Design, Analysis, and Optimization of Self-Resonant Wireless Power Transfer Systems

by

Neda ZAHEDI SAADABAD

MANUSCRIPT-BASED THESIS PRESENTED TO ÉCOLE DE TECHNOLOGIE SUPÉRIEURE IN PARTIAL FULFILLMENT FOR THE DEGREE OF DOCTOR OF PHILOSOPHY
Ph.D.

MONTREAL, APRIL 23RD, 2026

ÉCOLE DE TECHNOLOGIE SUPÉRIEURE
UNIVERSITÉ DU QUÉBEC

BOARD OF EXAMINERS

THIS THESIS HAS BEEN EVALUATED

BY THE FOLLOWING BOARD OF EXAMINERS

Dr. Qingsong Wang, Thesis Supervisor
Electrical Engineering Department, École de technologie supérieure

Dr. Ambrish Chandra, Thesis Co-supervisor
Electrical Engineering Department, École de technologie supérieure

Dr. Zhaoheng Liu, Chair, Board of Examiners
Department of Mechanical Engineering, École de technologie supérieure

Dr. Gaixia Zhang, Member of the jury
Department of Electrical Engineering, École de technologie supérieure

Dr. Alireza Bakhshai, External Evaluator
Department of Electrical and Computer Engineering, Queens University

THIS THESIS WAS PRENSENTED AND DEFENDED

IN THE PRESENCE OF A BOARD OF EXAMINERS AND PUBLIC

APRIL 23RD, 2026

AT ÉCOLE DE TECHNOLOGIE SUPÉRIEURE

ACKNOWLEDGEMENTS

I would like to say my gratitude and appreciation to all people who have accompanied me during my doctorate study and during the writing of my dissertation with their great deal of support and assistance.

First, I would like to thank my supervisor, Dr. Qingsong Wang**,** for his guidance and supervision during my Ph.D. studies. His direction and support have been valuable in shaping the progress of this research and in guiding me toward the completion of this work.

I would like to express my deepest appreciation to my co-supervisor**,** Dr. Ambrish Chandra**,** for his continuous encouragement, kindness, and positive energy throughout my doctoral studies. His supportive attitude, thoughtful advice, and motivating spirit have always given me confidence and inspiration. His constructive feedback and valuable insights significantly contributed to the development and improvement of this research.

My sincere gratitude also goes to my husband, Javad Nekoui**,** who has been not only my life partner but also my academic companion throughout this journey. As a researcher in the same field and a co-author of several of my research works, he has always been a source of intellectual support through technical discussions, idea exchange, and thoughtful feedback. His patience, understanding, and continuous encouragement helped me overcome many challenges and played an essential role in both my academic progress and personal growth during this Ph.D. journey.

Finally, I would like to express my deepest gratitude to my parents and my brother for their unconditional love, endless encouragement, and unwavering belief in me. Their support, sacrifices, and constant motivation have been the foundation of my achievements and the source of my strength throughout my life. Their presence, even from afar, has always inspired me to pursue my goals with determination and perseverance.

Conception, analyse et optimisation des systèmes de transfert d'énergie sans fil auto-résonants

Neda ZAHEDI SAADABAD

RÉSUMÉ

Cette thèse établit une méthodologie unifiée de conception électromagnétique pour les systèmes de transfert d'énergie sans fil auto-résonants (SRWPT), fonctionnant sans condensateurs de compensation externes. Contrairement aux architectures résonantes conventionnelles reposant sur des composants capacitifs discrets, générant amplification de tension, contraintes diélectriques, pertes parasites et limitations de fiabilité l'approche proposée intègre la résonance directement dans la structure des bobines par un contrôle maîtrisé de l'inductance et de la capacité distribuées. La limitation fondamentale des bobines planes auto-résonantes, soit une capacité intrinsèque insuffisante déplaçant la fréquence de résonance vers la gamme des mégahertz, est surmontée grâce à une architecture PCB multicouche empilée en parallèle, augmentant la capacité inter-couches effective tout en réduisant la résistance équivalente par partage de courant. Afin de maintenir un rendement élevé en régime de puissance moyenne à basse fréquence (inférieure à 150 kHz), une stratégie de réduction des pertes fondée sur le rapport largeur de piste (TWR) et le rapport d'espacement des pistes (TGR) est introduite pour atténuer la résistance AC liée aux effets de peau et de proximité, préservant ainsi un facteur de qualité élevé. Une analyse approfondie basée sur la géométrie démontre en outre que la forme des bobines influence intrinsèquement l'inductance, la capacité distribuée, le couplage magnétique, la répartition des pertes et la tolérance au désalignement, révélant l'interdépendance des paramètres électromagnétiques dans les systèmes auto-résonants.

Afin de limiter la dégradation du rendement sous faible couplage magnétique et en présence d'entrefer important, cette thèse développe des architectures auto-résonantes multi-bobines, notamment à trois bobines, permettant d'augmenter l'impédance réfléchie et de stabiliser le transfert de puissance sans recourir à des éléments réactifs discrets. Par la coordination des interactions inductance–capacité mutuelles et la mise en forme intrinsèque de l'impédance, les configurations proposées améliorent la robustesse face aux variations de distance et au désalignement. Une topologie série–série auto-résonante à trois bobines est élaborée pour étendre la portée de transfert au-delà des limites des systèmes à deux bobines. Pour les applications biomédicales à encombrement restreint, une architecture réceptrice compacte est introduite, exploitant des bobines PCB multicouches interconnectées afin d'augmenter l'inductance effective sans accroître les dimensions physiques. Les validations expérimentales réalisées en régimes de puissance moyenne et faible confirment que la structuration multicouche, la conception guidée par la géométrie et l'ingénierie du couplage intrinsèque multi-bobines constituent une base évolutive et intégrable pour des systèmes de transfert d'énergie sans fil à haut rendement et structurellement robustes, destinés aux plateformes industrielles, aux systèmes de recharge pour véhicules à guidage automatique (AGV) et aux dispositifs biomédicaux compacts.

Mots-clés : Transfert d’énergie sans fil (WPT), systèmes auto-résonants, bobines multicouches, architectures multi-bobines, capacité distribuée, facteur de qualité, rapport largeur de piste (TWR), rapport d’espacement des pistes (TGR), géométrie des bobines, applications biomédicales et industrielles.

Design, analysis, and optimization of self-resonant wireless power transfer systems

Neda ZAHEDI SAADABAD

ABSTRACT

This dissertation establishes a unified electromagnetic design methodology for low-frequency, capacitor-free Self-Resonant Wireless Power Transfer (SRWPT) systems. Unlike conventional resonant WPT architectures that rely on discrete compensation capacitors, thereby introducing voltage magnification, dielectric stress, parasitic losses, and long-term reliability constraints, the proposed approach embeds resonance directly within the coil structure through deliberate control of distributed inductance and capacitance. The primary limitation of planar self-resonant coils, namely insufficient intrinsic capacitance that shifts the natural resonant frequency toward the MHz range, is systematically resolved through a parallel-stacked multilayer PCB architecture that enhances effective interlayer capacitance while concurrently reducing equivalent resistance via current sharing. To sustain high efficiency under medium-power, under150 kHz operation, layout-level electromagnetic optimization using Track-Width Ratio (TWR) and Track-Gap Ratio (TGR) is introduced as a structured loss-reduction strategy that mitigates AC resistance arising from skin and proximity effects, thereby preserving a high-quality factor. In parallel, a comprehensive geometry-driven analysis reveals how coil shape intrinsically governs inductance, distributed capacitance, coupling behavior, loss distribution, and misalignment tolerance through strongly interdependent electromagnetic mechanisms. By transforming parasitic effects into controllable design parameters, this work demonstrates that low-frequency intrinsic resonance, high-Q performance, and compact PCB implementation can be achieved simultaneously within a rigorous structural framework.

To address efficiency degradation under weak magnetic coupling and extended air gaps, the dissertation further advances self-resonant three-coil architectures that enhance reflected impedance and stabilize power transfer without reintroducing discrete reactive components. Through coordinated mutual inductance–capacitance interaction and intrinsic impedance shaping, the proposed multi-coil configurations strengthen effective coupling and improve robustness against distance variation and misalignment. A series–series self-resonant three-coil topology is developed to extend transfer range beyond the practical limits of conventional two-coil systems, while maintaining structural simplicity and capacitor-free operation. For size-constrained biomedical platforms, a compact receiver architecture is introduced in which interconnected multilayer PCB coils increase effective inductance without enlarging physical dimensions, enabling improved voltage gain and transfer efficiency under strict geometric constraints. Experimental results obtained under both medium and low power operating conditions demonstrate that multilayer structuring, geometry driven design, and intrinsic multicoil coupling strategies collectively establish a scalable and integration ready foundation for high-efficiency, structurally robust wireless power transfer systems suitable for industrial platforms, automated guided vehicle (AGV) charging applications, and biomedical devices.

Keywords: Wireless Power Transfer (WPT), Self-Resonant Systems, Multilayer Coils, Multicoil Architectures, Distributed Capacitance, Quality Factor, Track Width Ratio (TWR), Track Gap Ratio (TGR), Coil Geometry, Biomedical and Industrial Applications.

TABLE OF CONTENTS

LIST OF TABLES

LIST OF FIGURES

Page

LIST OF ABBREVIATIONS AND ACRONYMS

WPT	Wireless Power Transfer
SR-WPT	Self-Resonant Wireless Power Transfer
SRF	Self-Resonant Frequency
IPT	Inductive Power Transfer
MRC-WPT	Magnetic Resonant Coupling Wireless Power Transfer
PTE	Power Transfer Efficiency
TX	Transmitter coil
RX	Receiver Coil
AGV	Automated Guided Vehicle
EV	Electric Vehicle
D-WPT	Dynamic- Wireless power Transfer
GaN	Gallium Nitride
HF	High Frequency
LF	Low Frequency
K	Coupling Coefficient
L	Inductance
C	Capacitance
R	Resistance
Q	Quality Factor
HB	Half-Bridge
FEM	Finite Element Method
VA	Volt-Ampere

SC	Self-Compensated
PCB	Printed Circuit Board
SS	Series-Series
SP	Series - Parallel
PS	Parallel - Series
PP	Parallel - Parallel
PSC	Printed Spiral Coils
TWR	Track Width Ratio
TGR	Track Gap Ratio
FR4	Flame Retardant 4 (PCB dielectric material)
RMS	Root Mean Square
DC	Direct Current
AC	Alternating Current
PWM	Pulse Width Modulation
PTE	Power Transfer Efficiency
PDL	Power Deliver to Load
EMI	Electromagnetic Interference
EMC	Electromagnetic Compatibility
SAR	Specific Absorption Rate
ICNIRP	International Commission on Non-Ionizing Radiation Protection
IEC	International Electrotechnical Commission
IEEE	Institute of Electrical and Electronics Engineers

LIST OF SYMBOLS AND UNITS OF MEASUREMEN

Symbol	Description	Unit
(V)	Voltage	V
(I)	Current	A
(P)	Power	W
(P_{in})	Input Power	W
(P_{out})	Output Power	W
(η)	Efficiency	%
(L)	Inductance	uH
(L_{TX})	Transmitter Inductance	uH
(L_{RX})	Receiver Inductance	uH
(M)	Mutual Inductance	uH
(k)	Coupling Coefficient	–
(C)	Capacitance	uF
(C_p)	Parasitic Capacitance	uF
(R)	Resistance	Ω
(R_L)	Load Resistance	Ω
(R_{ESR})	Equivalent Series Resistance	Ω

(Q)	Quality Factor	–
(f_r)	Resonant Frequency	Hz
(w)	Angular Frequency	rad/s
(μ_0)	Permeability of Free Space	H/m
(μ_r)	Relative Permeability	–
(ε_0)	Permittivity of Free Space	F/m
($\boldsymbol{\varepsilon}_r$)	Relative Permittivity	–
(d)	Axial Distance	m
(r)	Coil Radius	m
(N)	Number of Turns	–
(A)	Cross-Sectional Area	m^2
(I_{TX})	Transmitter Current	A
(I_{RX})	Receiver Current	A
(V_{TX})	Transmitter Voltage	V
(V_{RX})	Receiver Voltage	V
(Z)	Impedance	Ω
(J)	Current Density	A/m^2
(E)	Electric Field Intensity	V/m
(S_{21})	Forward Transmission Coefficient	dB
(S_{11})	Reflection Coefficient	dB

INTRODUCTION

Wireless Power Transfer (WPT) enables the transmission of electrical energy without galvanic contact by exploiting time-varying electromagnetic fields. A major modern milestone was reported in 2007 by researchers at Massachusetts Institute of Technology, who demonstrated resonant inductive coupling capable of transmitting approximately 60 W of power over a distance of about 2 meters with reasonable efficiency, experimentally validating mid-range WPT feasibility. In contemporary near-field implementations, power is transferred through magnetic coupling between spatially separated coils, providing electrical isolation, improved safety, reduced maintenance, and enhanced reliability. These advantages have enabled widespread applications in biomedical implants (Shah, Zada, Shah, Basir & Yoo, 2023) consumer electronics charging, automated guided vehicles (AGVs) (Li, Li, Gao, Mu & Han, 2025), industrial charging platforms, electric vehicles (Zhang, Gong & Chang, 2023), and integrated motor-drive systems. However, because the transmitter and receiver are separated by an air gap, magnetic coupling is inherently incomplete, and part of the generated magnetic flux appears as leakage inductance and reactive impedance, limiting effective real power transfer.

As transfer distance increases or misalignment occurs, the coupling coefficient decreases and reactive effects become dominant. Under loosely coupled conditions, a significant portion of the input energy circulates in the reactive field rather than being delivered to the load, reducing power factor and overall efficiency. Resonant operation is therefore essential in practical WPT systems: by compensating reactive components at the operating frequency, resonance minimizes net reactive impedance and enables efficient real power transfer while strengthening magnetic field interaction between the coils (Shevchenko et al., 2019). Various compensation topologies have been developed, including Series–Series (SS), Parallel–Parallel (PP), Series–Parallel (SP), and Parallel–Series (PS) configurations, as well as advanced hybrid structures such as LLC-based multi-resonant networks to improve voltage gain, load tolerance, and efficiency under varying coupling conditions (Wu et al., 2023) (Saket, Shafiei & Ordonez, 2016).

Limitations of Conventional Capacitor-Based Resonance

In conventional WPT systems, resonance is achieved using discrete compensation capacitors, which provide tuning flexibility but introduce important limitations in high-Q operation. At the resonant frequency, voltage magnification occurs across the compensation capacitor, and its voltage can become approximately Q times greater than the input voltage. In high-efficiency designs where Q is large, this results in significant dielectric stress and thermal loading. Consequently, bulky and expensive high-voltage capacitors are required, increasing system size and limiting integration. Moreover, discrete capacitors introduce parasitic losses and are sensitive to aging and temperature variations, leading to detuning and long-term reliability concerns, particularly in compact or embedded applications (Kim, Abu-Siada & Sutinjo, 2018). These constraints motivate the exploration of alternative approaches in which resonance is achieved intrinsically by electromagnetic structure rather than by external lumped components.

Self-Resonant Wireless Power Transfer system

Every practical coil inherently exhibits distributed parasitic capacitance between adjacent turns and layers, which, together with its inductance, forms a natural resonant structure. While this capacitance is traditionally regarded as an undesirable parasitic effect, it can be intentionally engineered through precise conductor spacing, layering, and geometric arrangement to establish resonance without the need for discrete compensation capacitors. This principle underlies Self-Resonant Wireless Power Transfer (SRWPT), in which the coil itself functions as the resonant element. By eliminating external capacitors, SRWPT architectures mitigate voltage stress on discrete components, enhance structural robustness, and enable more compact and integrated implementations (Zahedi, Wang & Chandra, .2025) (Sérgio et al., 2016). However, resonance in such systems becomes intrinsically embedded in the electromagnetic geometry of the coil, meaning that the operating frequency is no longer independently tunable but determined by the inductance–capacitance balance. Consequently, achieving a target frequency band requires deliberate and precise electromagnetic coil engineering.

Efficiency Enhancement Mechanisms in Resonant Wireless Power Transfer

In WPT systems, both efficiency and transferred power must be carefully evaluated, particularly under varying air gaps and misalignment conditions. These performance metrics are fundamentally governed by the interaction between the coupling coefficient (k) and the quality factors (Q_1, Q_2) of the coils (Qin & Costinett, 2025), as expressed by

$$\eta \approx (k^2.Q_1.Q_2)/(1 + k^2.Q_1.Q_2) \quad (0.1)$$

which indicates that high efficiency requires a sufficiently large $k^2Q_1Q_2$ product. Therefore, improving system performance ultimately depends on enhancing magnetic coupling and resonator quality. The coupling coefficient primarily depends on the geometric and spatial relationship between the coils. Coil dimensions, turn distribution, alignment accuracy, and especially the air-gap distance determine how effectively the transmitter-generated magnetic flux links the receiver. Increasing coil size can enhance mutual inductance and improve k, but at the expense of larger parasitic capacitance and increased footprint. Reducing coil separation strengthens coupling; however, many practical applications such as electric vehicle charging pads, rail-based WPT systems, and implanted medical devices impose physical constraints that limit proximity. Misalignment further degrades coupling, making coil geometry and compensation network design critical for stable operation. To address weak coupling, techniques such as ferrite materials (Zahedi, wang & Chandra, 2025), magnetic core shaping, resonant relay coils (Jang et al., 2017), superconducting windings (Wang et al., 2018), metamaterials (Lee & Yoon, 2020), and metasurfaces (Li Long et al., 2017) have been explored to enhance magnetic flux linkage and mutual inductance.

In parallel, the quality factor Q significantly influences both efficiency and power capability (Dautov et al., 2025). Q represents the ratio of stored to dissipated energy in the resonant structure and depends on inductance, operating frequency, and total system losses. These losses include copper resistance, skin and proximity effects at higher frequencies, eddy-current losses

in nearby conductive materials, and magnetic core losses when ferrites are used. Although increasing frequency can raise Q by increasing inductive reactance, excessive frequency intensifies high-frequency losses, parasitic capacitance effects, and electromagnetic compatibility (EMC) concerns. Consequently, practical WPT systems must operate within an optimized frequency range that balances coupling strength, loss mechanisms, and structural constraints to achieve high and stable efficiency.

Research Objectives

Self-resonant wireless power transfer (SRWPT) eliminates external compensation capacitors by embedding resonance within the intrinsic inductance–capacitance interaction of the coil. While this approach improves structural robustness and reduces component stress, it introduces new electromagnetic design challenges that must be addressed through structural optimization.

A primary limitation of self-resonant planar PCB coils is the inherently small distributed capacitance generated between adjacent turns, which naturally shifts the intrinsic self-resonant frequency toward the MHz range. Such high-frequency operation is not always desirable for medium-power platforms that favor operation below 150 kHz. Therefore, achieving low-frequency self-resonance without relying on external compensation capacitors becomes a fundamental research problem. At the same time, preserving a high-quality factor (more than 100) is critical, since it governs the balance between stored electromagnetic energy and total dissipative losses, directly affecting efficiency, power capability, and transfer stability. Consequently, an effective design strategy must simultaneously increase the effective capacitance, control loss mechanisms, and maintain structural compactness while sustaining high electromagnetic performance.

Beyond frequency placement and quality factor improvement, coil geometry plays a decisive role in SRWPT performance. In self-resonant systems, geometry simultaneously influences inductance, distributed capacitance, AC resistance distribution, resonant frequency, magnetic coupling, and overall efficiency. Because these parameters are strongly interdependent, a

systematic comparative investigation of planar geometries is required to quantify their combined impact on system-level performance.

While optimized two-coil SRWPT systems can achieve high efficiency at moderate distances, efficiency degradation becomes more pronounced as distance increases. To enhance effective coupling and reflected impedance in larger swithout reintroducing discrete compensation networks, self-resonant coils are integrated into three-coil architectures and validated in the low-frequency regime for medium-power applications. Furthermore, for compact biomedical platforms where receiver footprint is strictly constrained, a dedicated self-resonant three-coil configuration is developed to increase effective inductance and efficiency without enlarging the receiver area.

Accordingly, the research objectives of this thesis are defined as follows:

• Develop multilayer PCB self-resonant coils capable of operating at low frequency for medium-power wireless power transfer applications.

• Improve coil quality factor through layout-level electromagnetic optimization using track-width ratio (TWR) and track-gap ratio (TGR).

• Systematically quantify and compare the influence of planar coil geometries on SRWPT performance, including inductance, distributed capacitance, resonant frequency, AC resistance, quality factor, and overall efficiency.

• Integrate self-resonant coils into three-coil architectures to enhance effective coupling, reflected impedance, and transfer efficiency in longer distances.

• Design and experimentally validate a compact self-resonant three-coil receiver architecture for biomedical applications that increases effective inductance and improves efficiency without enlarging the receiver footprint.

Methodology

Step I: WPT system specifications were first defined, including target power level, transfer distance, operating frequency, efficiency requirements, and application constraints. These specifications established the design boundaries for coil structure, resonance frequency, and inverter operation.

Step II: Based on the defined specifications, multilayer, double-layer, and three-coil self-resonant WPT configurations were designed. Multilayer stacking was employed to increase distributed capacitance and enable low-frequency intrinsic resonance without external capacitors. For improved coupling and reflected impedance, three-coil architectures were implemented. Layout-level optimization parameters, including Track-Width Ratio (TWR) and Track-Gap Ratio (TGR), were incorporated to reduce AC resistance and enhance the quality factor. According to the targeted resonant frequency determined by coil geometry, a full-bridge inverter was designed to operate at the intrinsic resonance of the system.

Step III: Electromagnetic simulations were performed in ANSYS Maxwell to extract inductance, distributed capacitance, AC resistance, coupling coefficient, and resonant frequency. Parametric analyses were conducted to evaluate the influence of geometry, multilayer configuration, and layout optimization. System-level simulations were carried out in MATLAB/Simulink to analyze efficiency, output power, inverter performance, and system behavior under different air gaps and misalignment conditions.

Step IV: Optimized coils were fabricated using multilayer PCB technology. The transmitter and receiver circuits, including the full-bridge inverter, were assembled based on the designed schematics and layouts. The prototype WPT system was experimentally tested under varying

distances and alignment conditions. Measured efficiency, output power, and electrical stresses were compared with simulation results to validate the proposed self-resonant design approach.

Thesis Outline

This thesis consists of five chapters focusing on the design and optimization of self-resonant wireless power transfer (SRWPT) systems.

Chapter 1 presents a comprehensive review of self-resonant coil structures for WPT, including PCB and non-PCB implementations. Single-layer, double-layer, and multilayer configurations are analyzed in terms of distributed capacitance, resonance behavior, and design challenges. Chapter 2 proposes a multilayer PCB self-resonant coil for low-frequency. By parallel connection of double-layer coils and applying TWR and TGR optimization, AC losses are reduced and quality factor is improved, with validation through modeling, FEM simulation, and experiments. Chapter 3 investigates the influence of planar coil geometry on SRWPT performance. Circular, square, hexagonal, and octagonal coils are compared in terms of efficiency, power transfer capability, quality factor, and misalignment tolerance using theoretical, simulation, and experimental analysis. Chapter 4 introduces a compact self-resonant three-coil architecture for footprint-constrained receivers. Structural inductance enhancement and intrinsic impedance shaping improve efficiency without external capacitors, and the system is experimentally validated. Chapter 5 presents a series–series self-resonant three-coil WPT system designed to enhance efficiency in long-distance operation. The three-coil architecture is employed to improve magnetic coupling and transfer robustness, while TWR and TGR optimization reduce losses and enhance quality factor, demonstrating the effectiveness of multi-coil self-resonant structures for extended-range applications.

CHAPTER 1

A COMPREHENSIVE REVIEW OF SELF-RESONANT COIL STRUCTURES FOR WIRELESS POWER TRANSFER SYSTEM

1.1 Introduction

In recent years, research on wireless power transfer (WPT) system is actively carried on, for the sake of their convenience, safety, low maintenance, and high reliability. The WPT systems, by alternating electromagnetic fields, can transfer electric energy to electrical equipment without any physical contact (Rezazade, Shahirinia, Naghash, Rasekh, & Afjei, 2022). There exist different types of wireless energy transfer technologies such as photoelectric, laser, microwave, capacitive coupling, and inductive coupling. According to the transmission distance, these technologies can be broadly categorized as near and far field WPTs, as shown in Figure 1.1 (Huang, Fang, Lam, Mak, & Martins, 2019). Due to the benefits of cordless and electrical isolation, WPTs have been widely employed in various practical applications like biomedical implants (Meng & Kiani, 2016), electric vehicles (Zhang et al., 2022), lighting, heating (Nguyen et al., 2021), and charging (Farajizadeh et al., 2019).

Figure 1.2 shows the typical configuration of a WPT system, which is composed of four parts: an AC source, a transfer system including a transmitting coil and a compensation network (Tx), a receiver system including a receiving coil and a compensation network (Rx), and a load. When the AC voltage source creates an alternating electric field around the coil, voltage is induced on the Rx coil that converts it back to electrical power to power up the load. To transfer electric power with a high efficiency, the transmitter and receiver need to have a strong coupling. Since both coils generate leakage flux that significantly increases the impedance, a compensation circuit is required at both the transmitter side and receiver side to compensate the leakage inductance and realize electrical resonance. Therefore, the impedance of TX and Rx can be minimized and the current of Tx and Rx can be maximized, which will significantly increase the transmitting power, efficiency, and range (Sun, Zhang, Rong, Shu, & Wei, 2021; Makhetha, Markus, & Abu-Mahfouz, 2022)

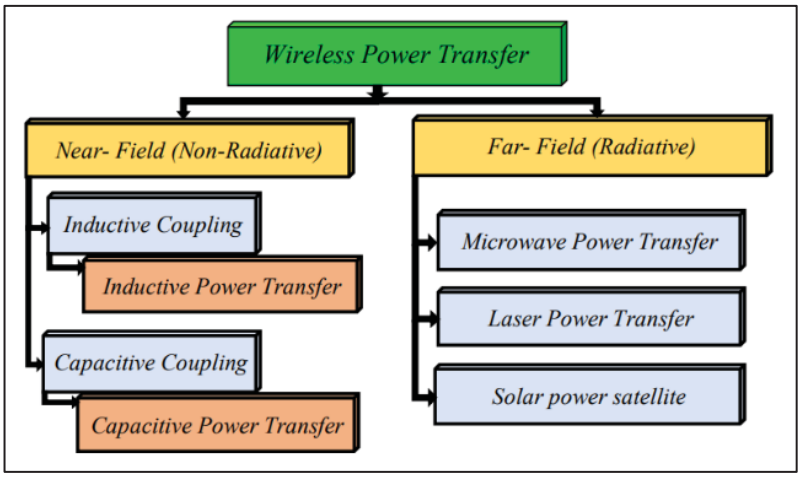

Figure 1.1 WPT classification and major research areas

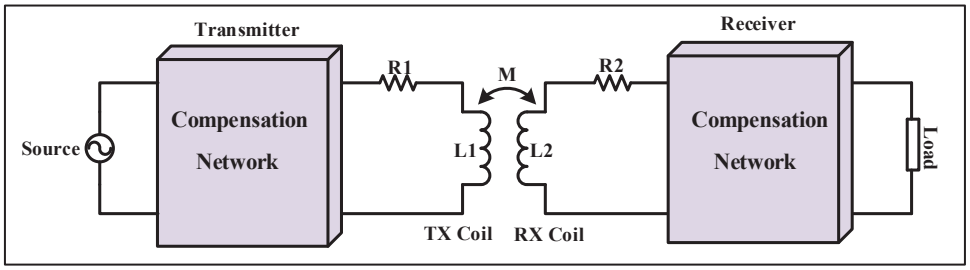

Figure 1.2 Equivalent circuit model of a compensated WPT system

A resonant coupler includes at least two magnetically coupled coils and capacitors, which can be applied discretely (Li, Zhang, Cui, & Wei, 2021; Zhang & Mi, 2015; Song, Li, Jiang, & Zhu, 2017) or distributed (Li & Costinett, 2018; Kim & Choi, 2022; Yi, Z., Li, M., Muneer, He, & Yang, 2020; Wang, Saket, Troy, & Ordonez, 2020; Lee, Kim & Moon, 2021; Jiang et al., 2020; Côte et al., 2022) in the circuit. Generally, a resonant coupler with external capacitors (in the form of externally lumped capacitors) is mostly used in WPT. Under resonance, the voltage or current of the capacitors gets Q times greater than the power source, where Q is the power factor of the system. Therefore, high voltage and current over the capacitors may cause the breakdown of the capacitors (de Miranda & Pichorim, 2019). Film capacitors are used to solve this problem, but these capacitors are bulky and too expensive (Bosshard, & Kolar, 2016). Consequently, despite the simple design, and easy manufacturing of the discrete capacitors, they suffer from limited quality factors in large power, low reliability, big size, and high cost. Self-compensated coils with high reliability and compact structure were proposed to

mitigate the aforementioned problems. Compared with discrete compensation method, self-compensated coils are more efficient but also face more challenges in designing the coils.

1.2 Compensation Network

1.2.1 Requirements of compensation network

WPT systems rely on the effective coupling between the transmitter and the receiver to transfer electric power. However, leakage inductance generated by the leakage flux of the coil significantly increases the impedance of the circuit. It is necessary to connect a compensation network to the transmitter and to the receiver, in which the former compensates the transmitter leakage inductance, increases the power factor near unity, and minimizes the VA rating of the power source, and the latter nullifies the receiver leakage inductance and maximizes the power transfer capability (Kunwar & Williamson, 2014). The performance of WPT system is influenced by many parameters such as transmission distance, number of loads, and misalignment, etc. External disturbance may also exist during the operation of WPT systems. Therefore, it is essential to have a suitable compensation network to cope with parameter variation to achieve constant current (CC) or constant voltage (CV) (Zhang et al., 2022). The efficiency of the WPT system depends on the quality factor and coupling coefficient of the coils. Furthermore, compensation topology and soft switching are the other factors that must be considered in designing the WPT system. Depending on the control strategy of the system, inverters may operate with variable or constant frequency. Inverters with variable frequency may cause bifurcation phenomenon, which means the occurrence of multiple zero phase angle (ZPA) resonant frequencies. This phenomenon is related to the value of input impedance (which varies from capacitance to inductance), compensation topologies, and load conditions, which may cause system instability. Therefore, an adequate compensation network has to be designed to have only one zero-phase angle under variable frequency control strategy and

different load conditions to guarantee system stability (Lu, Zhu, Lin, Zhang, Wang et Mi, 2020). Table 1.1 summarized the requirements of the compensation network.

Table 1.1 Requirements for compensation network

Requirement	Depend on
Minimized VA Rating and Maximized Power Transfer	Leakage Inductance, Compensation Topology
CV and CC out-put	Application, Compensation Topology
High Efficiency	Coupling Coefficient, Quality Factors of the Winding, Soft Switching
Bifurcation	Load Quality Factor, Compensation Topology and Capacitor
High Misalignment Tolerant	Compensation Topology

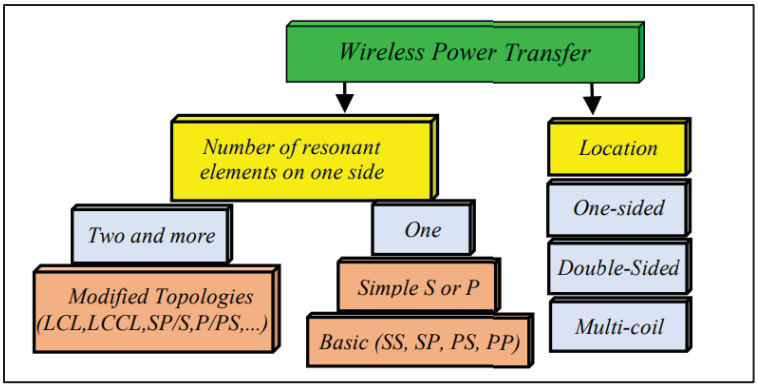

Figure 1.3. Classification of compensation network

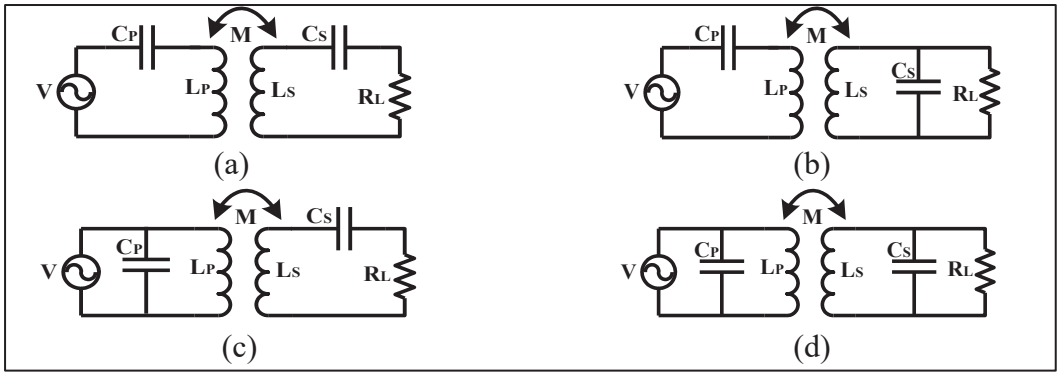

Figure 1.4. Classification of basic compensation topologies: (a) Series-Series (SS), (b) Series-Parallel (SP), (c) Parallel-Series (PS), (d) Parallel-Parallel (PP)

1.2.2 Classification of compensation network

Figure 1.3 shows the classification of the compensation have only one capacitor connected with the coil, namely, series-series (SS), series-parallel (SP), parallel-series (PS), and parallel-parallel (PP), in which the first letter shows the first coil's compensation, and the second letter shows the second coil's compensation, as shown in Figure 1.4 Other topologies with more resonant elements were also proposed, such as LCL, LCCL for the purpose of achieving high efficiency over a wide range of coupling and loading. The location of the compensation topology can be either on one side, or on both sides. In order to transmit power between multiple sources and multiple loads, multi-coil systems can be implemented and each coil will connect with a compensation circuit to achieve resonance.

1.3 Self-resonant Coils

Recent work on self-resonant coils has focused on structures in which the compensation capacitance is inherently integrated into the winding. Depending on the implementation, this capacitance may arise from the intrinsic electric-field coupling within the coil geometry or be intentionally enhanced through dielectric layering. In this study, such coils are broadly classified into intrinsically coupled self-resonant coils and dielectric-assisted self-resonant coils, and their characteristics for WPT applications are comparatively reviewed.

1.3.1 Self-resonant Coils Without PCB

This section reviews self-resonant coil structures implemented using wire-based or other non-PCB conductors.

1.3.1.1 Bifilar Coils

A bifilar coil consists of two conductors wound in parallel on the same form, bringing adjacent turns close together. This configuration generates distributed capacitance through the edge-

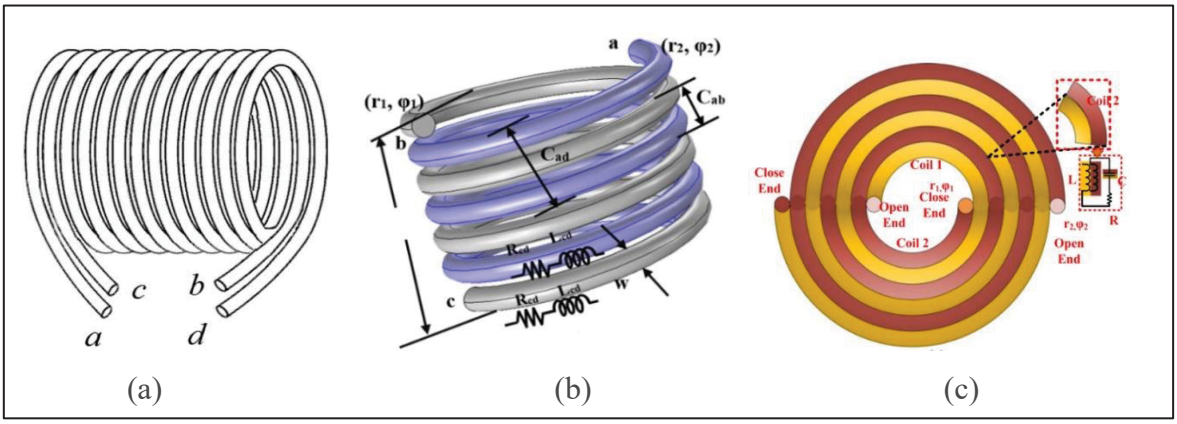

(a) (b) (c)

Figure 1.5 Self-resonant bifilar coils. (a) Taken from de Miranda & Pichorim (2016), (b) Taken from Vishnuram & Ramachandiran, (2020), and (c) Taken from Narayanamoorthi & Juliet (2018)

coupled method, in which the electric field between neighboring conductors forms a small parallel-plate–like capacitance along the coil. Combined with the coil's self-inductance, this edge-coupled capacitance enables the coil to achieve self-resonance without external capacitors. The total distributed capacitance C and the coil's inductance L determine the self-resonant frequency (SRF). Reference (de Miranda & Pichorim, 2019) compared closed- and open-ended bifilar coils: in a closed-bifilar coil, the conductors are connected at one end, forming a loop, which increases self-capacitance by $N^2/4$ relative to a conventional coil while maintaining similar inductance. Closed coils behave as parallel RLC circuits with maximum impedance at resonance. In open-bifilar coils, the conductors remain separate, producing roughly four times larger self-capacitance and four times lower inductance than the closed type. They behave as series RLC circuits with minimum impedance at resonance, while the first SRF remains nearly the same as that of the closed coil. As shown in Figure 1.5 (a), (de Miranda & Pichorim, 2016) proposes an open-ended solenoidal bifilar coil in which the required capacitance is formed naturally through the edge-coupled method, resulting in a self-resonant frequency of 802 kHz. While this design eliminates the need for external capacitors, it suffers from a relatively low Q-factor of 33. (de Miranda & Pichorim, 2019) employs the same bifilar geometry, but with a different terminal configuration. Although the intrinsic capacitance remains similar, the opposing currents in the interleaved windings significantly reduce the effective inductance, leading to a much higher self-resonant frequency of 5.87 MHz. The main limitation of this configuration is the low effective inductance seen by the source,

which restricts magnetic flux generation and limits achievable power transfer. In contrast, as illustrated in Figure 1.5 (b), (Vishnuram & Ramachandiran, 2020) utilizes a closed-ended bifilar coil for induction heating, where the load is directly heated by the magnetic field produced by the coil. This design operates at a self-resonant frequency of 29.5 kHz, achieving a maximum output power of around 500 W with an efficiency of 91.8%. The closed-ended configuration is preferred over the open-ended design because it enables series resonance above the self-resonant frequency, resulting in stronger magnetic coupling and more efficient power transfer. As it is shown in Figure 1.5(c), (Narayanamoorthi & Juliet, 2018) presents a planar version of the open bifilar coil, with the transmitter side implemented using HTS wire and the receiver side with copper. Although the design achieves self-resonance at 25 kHz, the power-transfer efficiency is limited to only 49.8% due to the low-quality-factor design and absence of structural optimization. To enhance efficiency over longer distances, a three-coil WPT system with open-bifilar coils is proposed (de Miranda & Pichorim, 2022). A relay coil is positioned between the transmitter and receiver, achieving a maximum power transfer efficiency of 47% at an 8 cm distance between the relay and load coils.

1.3.1.2 Helical Coils

In self-resonant helical coils, an edge-coupled capacitor is inherently formed between adjacent turns, which significantly affects the coil's resonant behavior. Various strategies have been explored to optimize these coils. As shown in Figure 1.6 (a), (Zhu et al., 2024) improves coil performance by intentionally varying the turn spacing instead of using a uniform pitch, enhancing design flexibility and achieving a 29% increase in quality factor and power transfer efficiency. (Zhu, 2024) investigates the same coil structure and demonstrates that precise modeling and reduction of ohmic resistance can further improve the quality factor and overall efficiency without altering the coil geometry. Additionally, (Zhu, Wang, Wu, Zhao, & Yu, 2023), as depicted in Fig. 1.6 (b), proposes a precise modeling approach and design

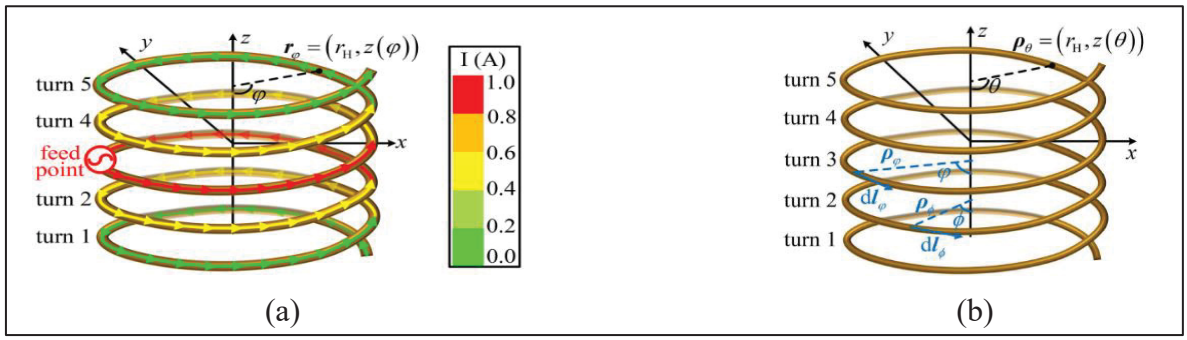

Figure 1.6 Schematic diagram of an open-ended helical coil. (a) Taken from Zhu (2024), (b) Taken from Zhu, Wang, Wu, Zhao, & Yu (2023)

guidelines for 6.78 MHz self-resonant helical coils, employing the PEEC method to calculate self-resonant frequencies and current distributions, rather than approximating the coil as a lumped inductance.

1.3.1.3 Coaxial Coils

Self-resonant coils based on coaxial structures have been widely studied for eliminating discrete compensation capacitors while maintaining high quality factor in wireless power transfer (WPT) systems. Early coaxial loop resonators achieved self-resonance through distributed capacitance between inner and outer conductors, with the loop current providing magnetic coupling for efficient power transfer (Dionigi & Mongiardo, 2012) as shown in Figure 1.7 (a). Later, as presented in Figure 1.7(b) substrate-mounted and welded coaxial resonators offered compact and mechanically robust designs, confining the electric field to reduce dielectric sensitivity and enable stable resonance without external capacitors (Zhang, Lin, Li, Cheng, & Fan, 2013). To enhance tuning flexibility, self-resonant coils with locally modified coaxial shields were introduced and is shown in Figure 1.7 (c), shaping parasitic capacitance to adjust resonance without discrete components (Son, Kim, Kim, Kim, & Park, 2011). More recently, compact planar multi-loop coils with coaxial cross sections allow precise control of distributed capacitance through geometry, achieving high-Q and stable resonance for practical wireless charging systems (Son, Kim, Kim, Kim, & Park, 2013) (Figure 1.7(d)).

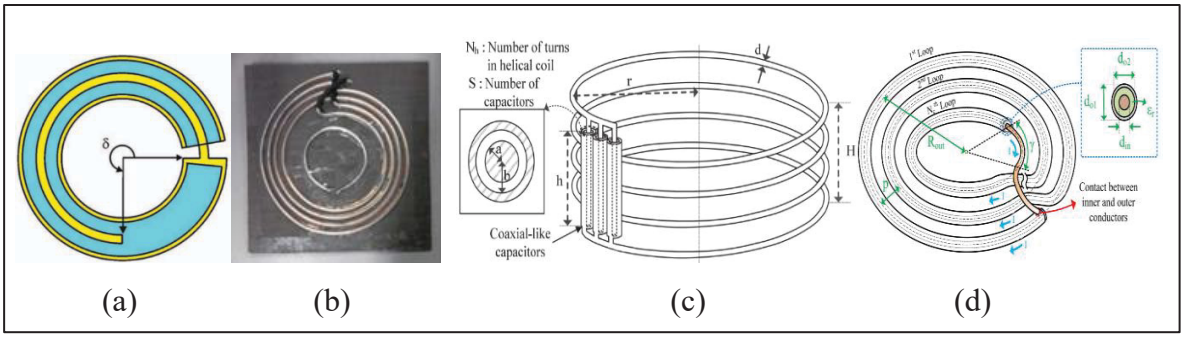

Figure 1.7. Coaxial self-resonant coils. (a) Taken from Dionigi & Mongiardo (2012), (b) Taken from Zhang, Lin, Li, Cheng, & Fan (2013), (c) Taken from Son, Kim, Kim, & Park, (2011), (d) Taken from Son, Kim, Kim, & Park (2013)

1.3.1.4 Face and edge coupled self-resonant wire-based multilayer coils

To eliminate discrete compensation capacitors, several studies have investigated wire-based self-resonant coils in which resonance is realized through parasitic capacitance formed between adjacent windings. Depending on the winding arrangement, this capacitance originates from face coupling between stacked layers, edge coupling between neighboring turns, or a combination of both. A basic implementation of this concept is the two-layer face-coupled structure. In (Yi, Li, Muneer, He, & Yang, 2020), an antisymmetric wire-wound coil is proposed, where two electrically isolated layers are wound in opposite directions and arranged face to face. As shown in Figure 1.8 (a), partial overlap between the layers forms an intrinsic series capacitance, enabling stable self-resonant operation without external components. To achieve self-resonance at low frequencies, particularly around the 85 kHz band, multilayer wire-wound self-resonant coils have been proposed and experimentally validated in (Nishihata et al., 2025; Hanawa & Imura, 2021; Kyaw, Stein, & Sullivan, 2017; and Hanawa, Imura, Hori, & Abe, 2022) which are illustrated in the Figure 1.8 (b), (c) and (d), respectively. In (Kyaw, Stein, & Sullivan, 2017), by stacking multiple open-ended winding layers increases both inductance and parasitic capacitance, enabling capacitor-less resonance with a reduced number of turns. In these designs, self-resonance is primarily governed by edge coupling between densely packed turns, with additional contribution from inter-layer face coupling. The effectiveness of this multilayer self- resonant approach under practical

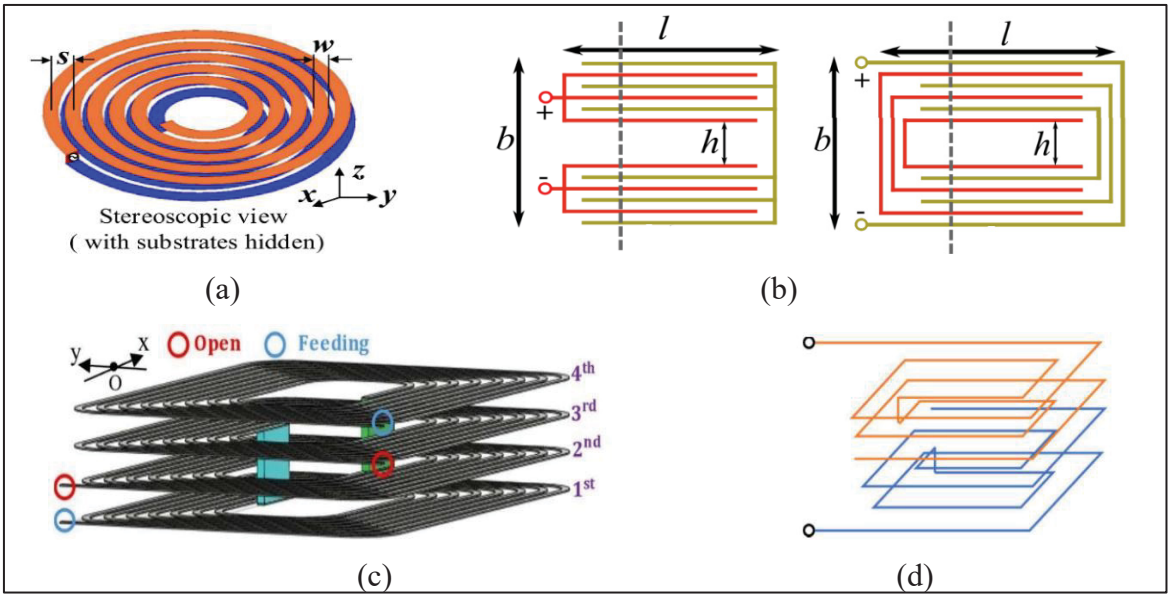

Figure 1.8 Face and edge coupled self-resonant wire-based multilayer coils. (a) Taken from Yi, Li, Muneer, He, & Yang (2020), (b) Taken from Kyaw, Stein, & Sullivan (2017), (c) Taken from Nishihata et al. (2025), (d) Taken from Hanawa, Imura, Hori, & Abe (2022)

conditions are further confirmed through comparative and application-level evaluations in (Hanawa, Imura, Hori, & Abe, 2022). Beyond low-frequency EV oriented applications, multilayer self-resonant wire-based coils have also been explored for mid-range WPT systems. In (Kim & Choi, 2022), spiral wire coils employ closely spaced turns and multilayer stacking to jointly control edge and face coupled capacitance, allowing resonance tuning through geometric parameters.

1.3.2 Self-Resonant Coils With PCB

To complement the wire-based self-resonant coils discussed in the previous section, PCB-based self-resonant planar coils have been extensively investigated as an alternative when compactness, mechanical robustness, and fabrication repeatability are required. Unlike wire-based implementations, where self-resonance mainly originates from inter-turn or bundle-level

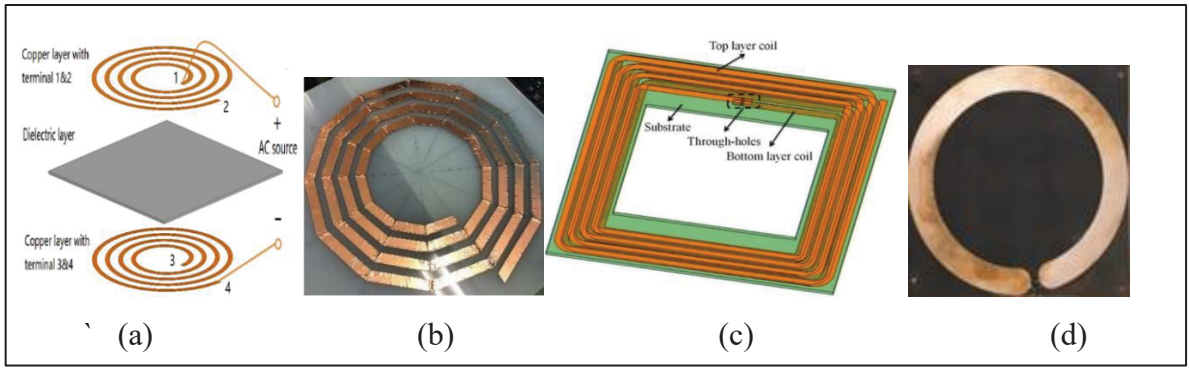

Figure 1.9. Double layer self-resonant PCB coils. (a) Taken from Li & Costinett (2018), (b) Taken from Sasahara & Akatsu (2022), (c) Taken from Chen, & Zhao (2013), (d) Taken from Cote, Garraud, Frassati, Sterna & Perichon (2022)

parasitic capacitance, PCB-based structures exploit face-coupled capacitance between well-defined overlapping copper conductors separated by a dielectric substrate. This mechanism enables accurate geometric control of the resonant frequency, improved prototype-to-prototype consistency, and inherently capacitor-less operation.

1.3.2.1 Double-Layer Self-Resonant Coils with Face Coupled Capacitance

The most fundamental PCB implementation is the double-layer self-resonant coil, where two spiral windings are printed on opposite sides of a dielectric substrate and connected in series. In (Li & Costinett, 2018), self-resonance is achieved through distributed face-coupled inter-layer capacitance between the opposing spirals, forming an intrinsic series LC resonator without discrete compensation components, as shown in Figure 1.9 (a). A related double-layer implementation is reported in (Sasahara & Akatsu, 2022), where an open-ended two-layer PCB spiral coil operates at 13.56 MHz and achieves self-resonance by exploiting parasitic capacitance generated both along the spiral pitch and between the facing layers, enabling capacitor-less operation under high-power conditions (see Figure 1.9 (b)). As it is illustrated in Figure 1.9 (c), a comprehensive analytical and experimental study is further reported in (Chen & Zhao, 2013), demonstrating that the resonant frequency and quality factor are primarily governed by the overlap area, substrate thickness, and dielectric properties.

Several works have focused on improving the modeling accuracy and loss characterization of double-layer PCB self-resonant coils. In (Yang et al., 2023), both lumped and distributed equivalent-circuit models are developed to accurately capture face-coupled capacitance and conduction loss, showing close agreement with measurements. The impact of dielectric loss on the equivalent series resistance and efficiency is explicitly investigated in (Takahashi, Hata, Imura, & Hori, 2018), confirming that substrate loss tangent plays a critical role even in double-layer configurations.

Beyond basic implementations, design-oriented and optimization-based approaches have been proposed to enhance performance predictability. In (Yang et al., 2023), a systematic optimization framework is introduced to jointly tune geometric parameters and resonance conditions, minimizing equivalent resistance while preserving self-resonant operation. Comparative assessment of different double-layer planar geometries is presented in (Zahedi, Wang, Chandra, 2025), where square, circular, and polygonal coils are benchmarked under identical conditions, revealing strong correlations between geometry, face-coupled capacitance, and efficiency. More advanced double-layer PCB self-resonant coils integrate impedance-matching functionality directly into the coil geometry. In (CÔTE Nathis et al., 2022), intrinsic impedance matching is achieved by combining face-coupled inter-layer capacitance with tailored spiral interconnections, enabling near-50-Ω input impedance at resonance without external matching networks. A related impedance-matched double-layer PCB self-resonant design is further reported in **(**Cote, Garraud, Frassati, Sterna & Perichon, 2022)**,** where experimental results confirm improved power transfer efficiency and robustness against load variation (see Fig 1.9 (c)).

Double-layer PCB self-resonant concepts have also been extended toward integrated resonator structures. In (Qu, Kiratipongvoot, Lee & Tang, 2018), an integrated PCB resonator design employs opposing conductive layers with open ends to realize strong face-coupled capacitance along the winding path, forming a compact self-resonant structure without discrete capacitors, as shown in Figure 1.9 (d). In addition, a fully compensated self-resonant configuration is reported in (Qin, Li, Sun & Costinett, 2023), where distributed inter-layer capacitive sections are introduced to suppress electric-field concentration while maintaining series self-resonant

operation. The influence of operating conditions and materials is further highlighted in (Takahashi, Hata, Imura, & Hori, 2018), where capacitor and ferrite-less double-layer self-resonant coils are compared under identical configurations. Experimental results demonstrate that dielectric loss in the inter-layer substrate becomes a dominant contributor to equivalent series resistance, particularly under low-frequency and high-current operation.

Double-layer PCB self-resonant coils have also been adapted to application-specific and shielded environments. In (Wu, Jiao, Cai, Yu & Ren, 2025), a sheet-metal-assisted planar self-resonant coil combines inter-turn capacitance with face-coupled capacitance to an underlying conductive layer, simultaneously achieving self-resonance and electromagnetic shielding for implantable WPT systems.

An extension of double-layer PCB self-resonant coils is the development of hybrid inductive–capacitive resonant couplers that integrate inductive and capacitive power transfer within a single PCB structure. In (Dai zhongyu et al., 2025) and (Wang, Sun, Zhang, Yang, & Hui, 2025), stacked PCB copper layers act simultaneously as spiral inductors and face-coupled capacitive plates, forming an intrinsic self-resonant tank without discrete components. As shown in Figure 1.10 (a) and (b), interlayer capacitance compensates the coil inductance while magnetic coupling enables inductive power transfer, with the asymmetrical design providing additional tuning of the inductive–capacitive coupling balance.

Finally, several studies demonstrate that double-layer PCB self-resonant coils can be scaled toward higher power levels and extended transfer distances through careful electric-field management and capacitive integration. In (Mohammad, Rallabandi, Onar, & Su, 2025) and (Xue lingxiao et al., 2023), high-voltage face-coupled capacitive sections are embedded within double-layer planar coils, enabling stable self-resonant operation under elevated voltage stress and meter-scale air gaps. High-frequency extensions of double-layer PCB self-resonant coils are further explored in (Mohammad et al., 2023), confirming the feasibility of MHz-range operation using embedded capacitive structures.

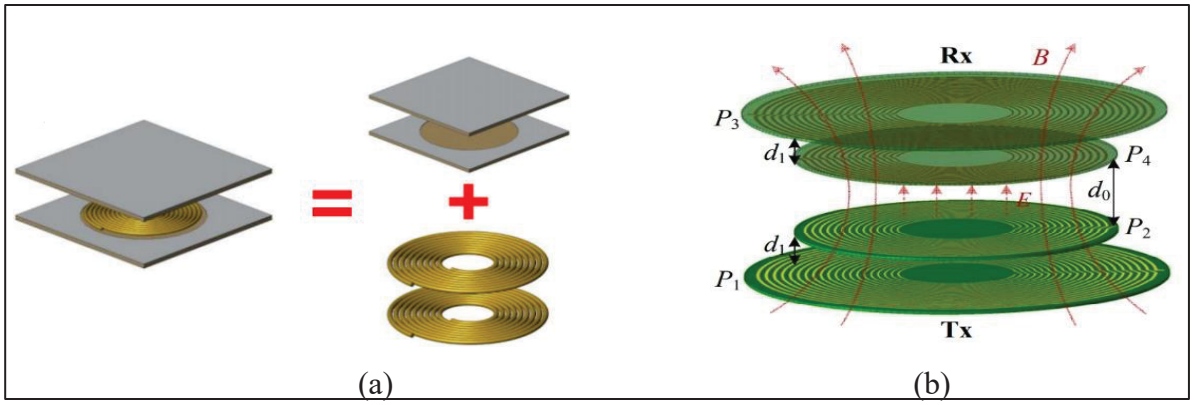

Figure 1.10. Hybrid inductive and capacitive coupler in self-resonant WPT coils. (a) Taken from Dai zhongyu et al. (2025), (b) Taken from Wang, Sun, Zhang, Yang, & Hui (2025)

1.3.2.2 Integrated and Hybrid PCB Self-Resonant Structures

While conventional double-layer PCB self-resonant coils rely on two opposing spiral windings to generate face-coupled capacitance, several studies realize self-resonance through integrated PCB structures with different physical mechanisms. In (Yin et al., 2023), the receiver is implemented as a multi-layer integrated PCB structure consisting of a spiral coil, a magnetic layer, and a conductive shielding layer. As shown in Figure 1.11 (a), self-resonance is achieved through the intrinsic capacitance formed between the coil and the adjacent conductive layer, rather than between two facing spiral windings. This integrated configuration simultaneously enables resonant operation and electric-field suppression, leading to reduced radiation without introducing discrete capacitors. A structurally distinct approach is reported in (Yi, Yang, Yang, X, Li, & Zeng, 2024), where self-resonance is realized using a coplanar waveguide (CPW)-based planar coil. In this design, as illustrated in Figure 1.11 (b), the distributed capacitance inherent to the CPW geometry enhanced through gradual variation of conductor width, forms the resonant network within a single PCB layer. The resonant frequency and quality factor are controlled by the CPW dimensions rather than interlayer coupling, demonstrating that PCB self-resonance can also be achieved through in-plane electric-field engineering instead of double-layer face coupling.

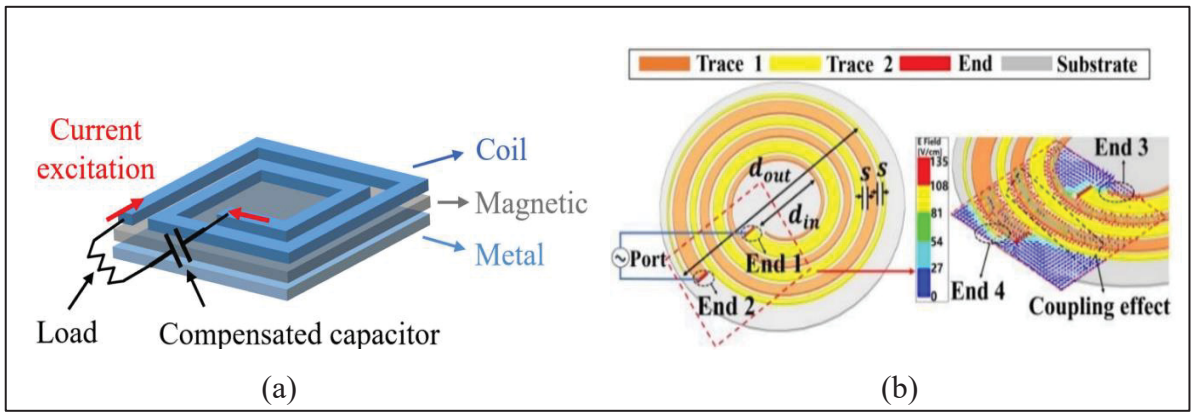

Figure 1.11 Integrated and hybrid PCB self-resonant. (a) Taken from Yin et al. (2023), (b) Taken from Yi, Yang, Yang, X, Li, & Zeng (2024)

1.3.2.3 Multi-Layers Self-Compensated Coils with PCB

Since the intra-winding capacitance is proportional to the area face between the adjacent coil layers, it is difficult to generate a large capacitance in a double layer coil, which results in a high resonant frequency that is normally several MHz as reported in the existing literatures. In order to reduce the resonant frequency, a multi-layer PCB coil was developed in (Wang, Saket, Troy, & Ordonez, 2020), whose configuration is shown in Figure 1.12 (a). This coil connected six 4-layer PCB coils in parallel to achieve a high value of the intra-winding capacitance and reduce the resonant frequency accordingly. Meanwhile, as a result of the parallel connection of the coils, the total resistance was reduced. Experimental results showed that this WPT system can achieve a maximum efficiency of 65% when operated at the resonant frequency of 120 kHz. Both the transmitter and the receiver are series connected with an additional inductor, to form a LCL compensation network so as to achieve impedance matching and a high-power factor. In contrast, a different multilayer PCB self-resonant structure is presented in (Zahedi; Wang & Ambrish, 2025), where a comparable coil footprint is maintained while employing fewer PCB layers, yet a larger effective intrinsic capacitance is achieved through deliberate geometric optimization. By adopting track-width-ratio (TWR) and track-gap-ratio (TGR) techniques, proximity and skin effects are effectively suppressed, leading to a significantly

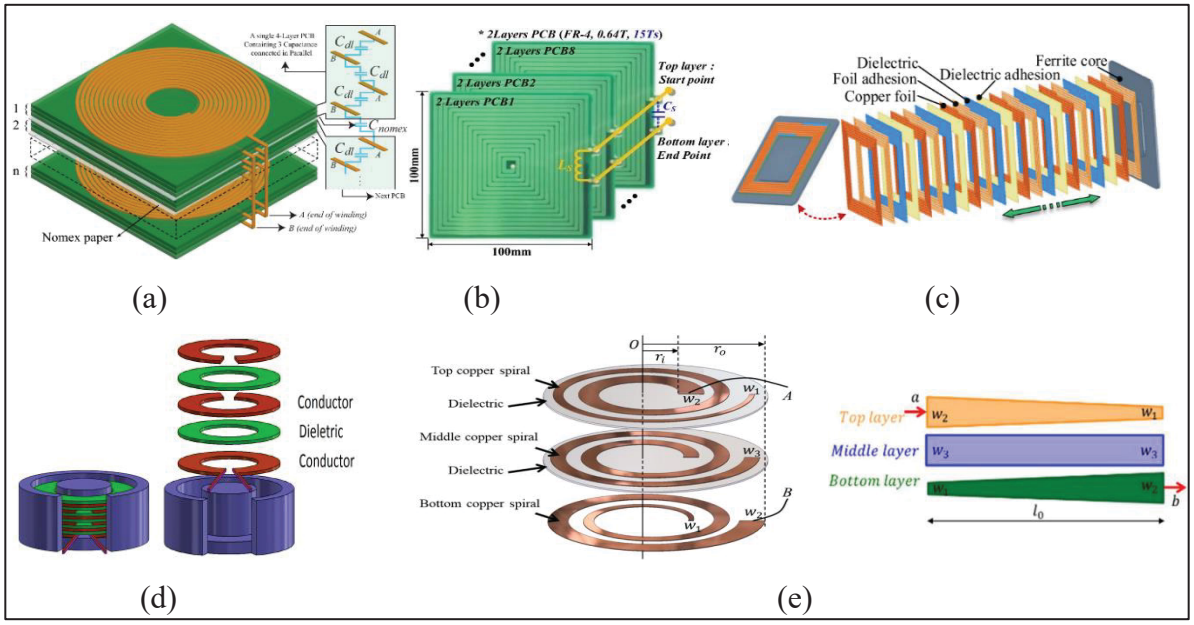

Figure 1.12 Multi-Layers self-compensated coils with PCB. (a) Taken from Wang, Saket, Troy, & Ordonez (2020), (b) Taken from Lee, Kim & Moon (2021), (c) Taken from Jiang et al (2020), (d) Taken from Stein, Kyaw & Sullivan (2018) (e) Taken from Qin, Li, Sun & Costinett (2023)

higher quality factor (Q = 123). As a result, the system achieves self-resonant operation at 147 kHz with a measured coil-to-coil efficiency of 94.7%. Another multi-layer PCB coils was designed in (Lee, Kim & Moon, 2021), in which 8 square-shaped coil layers were connected in parallel, as shown in Figure 1.12 (b). As a result, high intrinsic capacitance and low resonant frequency were achieved. By integrating a single switch to the rectifier, the system can supply a stable output power. Furthermore, soft switching can be achieved for both switches, which reduces the losses of the system. Compare to the WPT system investigated in (Wang, Saket, Troy, & Ordonez, 2020), this WPT system can achieve a higher efficiency of 75%. In (Jiang et al, 2020), a medium power low frequency WPT system based on self-resonance was proposed, which also used multi-layer coils, as shown in Figure 1.12 (c). The main privilege of this WPT system is achieving high value of capacitor and inductance which produces low resonance frequency (80-120Khz). This system consists of four multilayer capacitor-free with different dielectrics, and it was operated at an efficiency of 82% when transmitting 470W. Through analyzing the electric field distribution, insulation study of four dielectric layers was conducted to avoid the breakdown between two adjacent layers. In (Cote et al., 2022), the

influence of different dielectric materials on the power factor of self-compensated WPT system were investigated. The results showed that ROGERS 4003C achieve a power factor as large as 318, which is 7.6 times the power factor when FR4 was used. Figure 1.12 (d) shows another multilayer self-resonant coil studied in (Stein, Kyaw & Sullivan, 2018), which achieved a high-quality factor by using a thin foil layer. However, the fabrication of thin foil layer is a challenge. To overcome this concern, a modified self-resonant topology with PCB substrate was used. This configuration can effectively amplify the quality factor by 6.5 times at 7.09MHz. The same topology with a resonant amplifier was designed and implemented in (Gu et al, 2020), which is capable to transfer 300W power with a dc-dc efficiency of 95%. In (Stein, Kyaw, Feldman-Stein & Sullivan, 2018) and (Qin & Costinett, 2019), the current-sharing behavior in a three-layer PCB coil is systematically analyzed, providing insight into copper-loss reduction mechanisms in multilayer structures. Extending this concept to high-frequency operation, (Stein, Kyaw & Sullivan, 2017) experimentally demonstrates a high-Q multilayer PCB self-resonant structure ($Q \approx 1177$ at 7.08 MHz), where current distribution and loss mechanisms are characterized under MHz-range excitation. The same multilayer current-sharing structure in (Qin & Costinett, 2019), is further demonstrated in (Qin, Li & Costinett, 2020; Qin, Li, & Costinett, 2021) a nonuniform PCB self-resonant coil for electric vehicle charging, where stable MHz-range operation and 6.6 kW power transfer are experimentally validated, confirming the scalability of multilayer PCB self-resonant coils toward high-frequency and high-power WPT systems. Building on this architecture, a dedicated shielding design is introduced in (Qin, Li, Sun & Costinett, 2023), where magnetic and conductive shields are optimized to suppress leakage fields while preserving the multilayer current-sharing behavior for EV charging applications (see Figure 1.12 (e)).

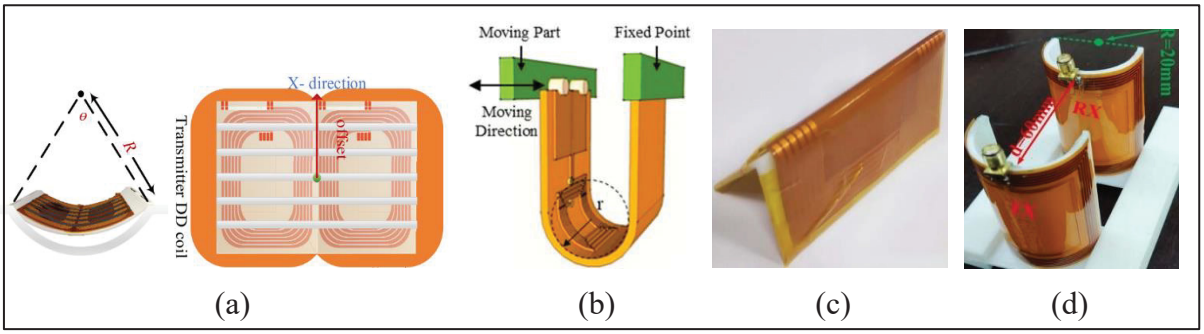

Figure 1.13. Flexible self-resonant coils. (a) Taken from Xiang, Jiang, Ma, Wang & Fan, (2024), (b) Taken from Xian et al. (2024), (c) Taken from Jeong et al. (2022), (d) Taken from Daura & Lawal (2019)

1.3.3 Flexible Self-Resonant Coils

Following rigid and multilayer PCB implementations, self-resonant coils with flexible and conformal structures have been investigated to support wireless power transfer on curved, wearable, and deformable platforms. Compared with rigid coils, flexible implementations introduce challenges such as deformation induced detuning, current redistribution, and loss variation, while enabling improved mechanical adaptability and form factor integration. One major research direction focuses on flexible self-resonant couplers assisted by nanocrystalline magnetic materials. As shown in Figure 1.13 (a) and (b), in (Xiang, Jiang, Ma, Wang & Fan, 2024) and (Xian et al., 2024), flexible planar coils are combined with nanocrystalline flake or ribbon cores to enhance magnetic confinement and power density while maintaining mechanical flexibility. These studies investigate self-resonant operation in the kHz frequency range, where the interaction between flexible geometry and magnetic material influences resonance stability, coupling behavior, and power capability in ultra-thin or surface conformal WPT interfaces. Another group of works addresses the interaction between mechanical deformation and resonant behavior in flexible coils. As it is illustrated in Figure 1.13 (c), in (Jeong et al., 2022), the electrical characteristics of single and double-layer flexible PCB coils are evaluated under repetitive bending, showing how resistance, inductance, and resonant frequency evolve with cyclic deformation. Complementary to this, (Cen, Wang, Yang, Zalhaf, & Han,2024) examines deformation induced detuning in flexible WPT systems and introduces

an automatic resonance tuning approach to maintain resonant operation across varying bending conditions.

Flexibility further enables conformal resonant WPT configurations on non-planar surfaces. In (Li, Yu, Kou, Ding & Zhang, 2022), flexible PCB coils mounted on cylindrical geometries are studied, establishing quantitative relationships between bending radius, inductance variation, and resonant frequency shift. Related concepts are explored in (Daura & Lawal, 2019), where printed flexible coil arrays support resonant electromagnetic excitation on curved surfaces, exploiting multiple resonant responses enabled by flexible geometries (see Figure 1.13 (d)). Furthermore, flexible resonant coils have been integrated into wearable platforms. In (Jeong et al., 2018), a double-layer flexible PCB coil embedded in a smartwatch strap is analyzed together with shielding materials, examining the effects of bending and proximity to the human body on resonant characteristics and coupling performance.

1.3.4 Resonant Network Types in Self-Resonant Coils

Self-resonant (SR) coils inherently support both series-type and parallel-type resonant behavior, depending on the terminal connection rather than the physical winding alone. As a result, an identical SR coil geometry can operate as either a series or parallel LC network under different excitation schemes, as conceptually compared in Figure 1.14 and discussed in (Odendaal & Li, 2005). In practical SR coil design, geometric features of the winding and substrate are deliberately tailored to emphasize specific parasitic capacitances. When the intrinsic capacitance is sufficiently large, resonance can be achieved without external matching components, although additional lumped elements may still be introduced to meet system level requirements. For series-resonant SR coils (Mohammad et al, 2023), resonance is typically embedded within the winding by introducing distributed capacitive coupling along the spiral path, for example through overlapping copper traces placed along the entire spiral or selected sections, as illustrated in Figure 1.15 (a). This fully integrated approach simplifies fabrication

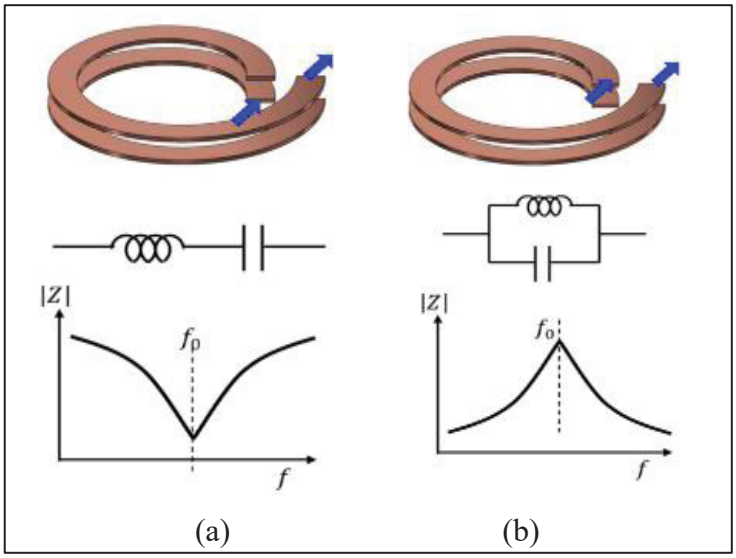

Figure 1.14 SR coil classification based on the resonant type (a) series resonant (b) parallel resonant

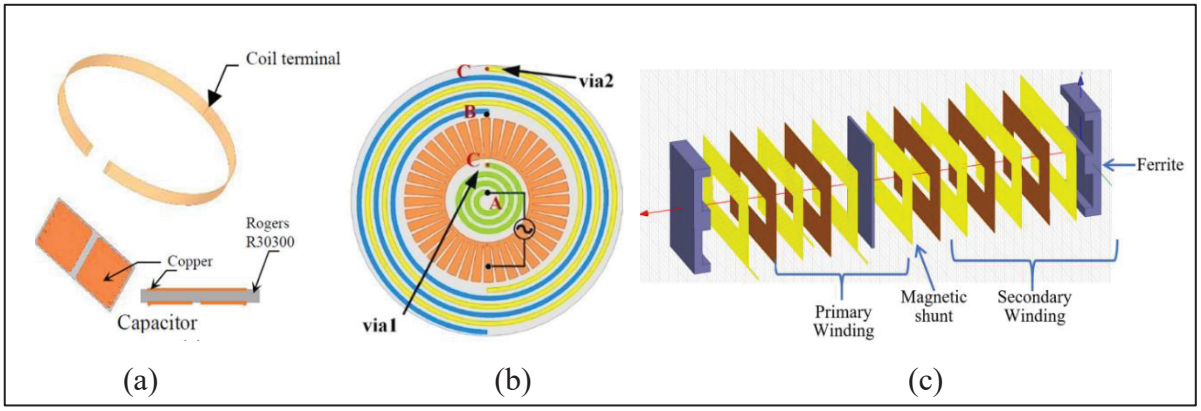

Figure 1.15 (a) Integrated series-resonance coil taken from (Mohammad et al, 2023) (b) LCC self-resonant coil structure taken from Yi Zixuan et al (2025) (c) LCC self-resonant coil structure taken from Ho & Pong (2019)

and packaging by eliminating discrete compensation capacitors. In contrast, parallel-resonant SR coils often require auxiliary circuitry to ensure stable excitation and avoid short-circuit conditions. As reported in (Gu et al., 2020), a series LC filter at the inverter side and a choke inductor at the rectifier side are employed to drive the parallel resonant tank. Because these components carry the same high-frequency circulating current as the resonant coil, their losses

directly affect efficiency, imposing stringent requirements on quality factor and current rating. Moreover, degraded power transfer performance has been reported for parallel–parallel resonant networks when directly driven by voltage source converters (Wang et al, 2019). Beyond basic series and parallel forms, higher order compensation networks have been explored for SR coils. In (Chen, Seyedi & Toliyat, 2024), an LCC compensation scheme is combined with a non-self-resonant transmitter coil by integrating a compensating inductor. Extending this concept, (Yi Zixuan et al, 2025) presents a self-resonant coil with high-order LCC characteristics, where a multi-segment winding passively realizes an LCC-type network. The detailed structure, illustrated in Figure 1.15 (b), incorporates magnetically coupled elements corresponding to the main coil, compensation coil, and parallel capacitive section. However, reported prototypes exhibit limited quality factor and power handling, highlighting challenges in scaling such integrated networks. An alternative integrated topology is the LCL-type self-resonant coil proposed in (Cote Nathis et al, 2022). A large outer loop forms a parallel LC resonance that is electrically combined with a smaller central spiral inductance. The demonstrated prototype operates at 12.7 MHz with a quality factor of 55, with analysis indicating that higher performance could be achieved using lower-loss dielectric substrates. In (Ho & Pong, 2019), a multilayer flexible printed-circuit planar transformer is presented, in which series capacitance is integrated within the winding structure to form an LLC-type resonant network, as shown in Figure 1.15 (c). The resonant behavior is realized through controlled interlayer capacitive coupling rather than discrete components, demonstrating an alternative implementation of integrated resonant networks using flexible printed circuitry. Overall, most mature SR coil implementations reported in the literature rely on series or parallel resonant networks, as increasing the compensation order substantially raises design complexity and may compromise efficiency. Nevertheless, higher-order networks such as LCL and LCC, widely adopted in non-self- resonant WPT systems for load tolerance and coupling robustness, suggest potential directions for future exploration of advanced SR coil architectures.

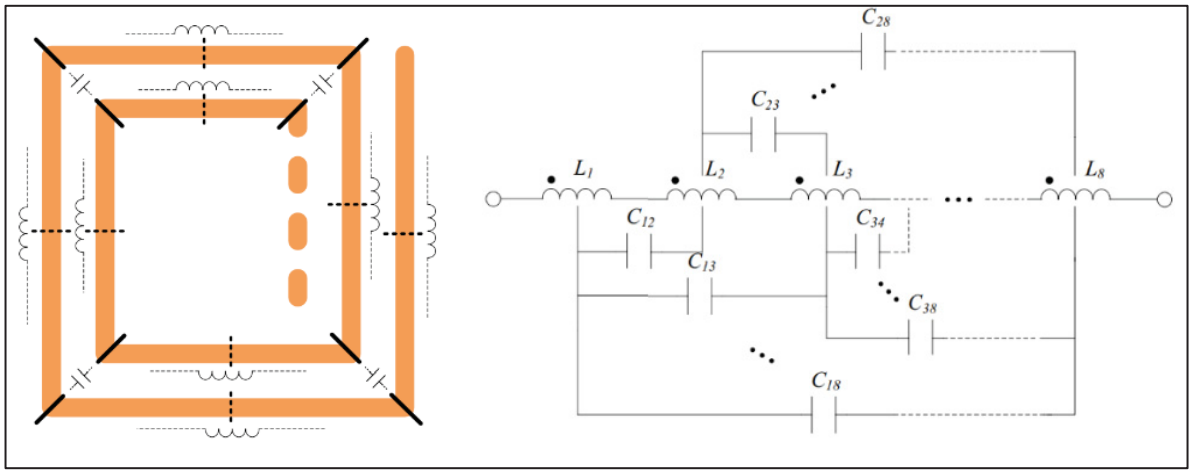

Figure 1.16 Schematic representation of the coil and the corresponding equivalent lumped-element circuit taken from Chen & Zhao (2013)

1.4 Inductance, Capacitance, Resistance, and Power Capability Modeling

Optimization of self-resonant coils requires accurate circuit models. This section briefly reviews the lumped-element L–C model and summarizes common approaches for estimating inductance, capacitance, and resistance across different coil geometries and operating conditions. Based on analytical, empirical, and numerical methods, these models provide practical insight into the relationship between coil layout, frequency, and loss mechanisms, and remain essential for SR coil design.

1.4.1 LC Lumped Model for Analysis

A widely adopted approach for analyzing self-resonant coil structures is the use of lumped-element LC circuit models, where the resonant behavior is represented using discrete inductive and capacitive elements derived from the coil geometry. In (Chen & Zhao, 2013), the modeling framework explicitly accounts for the self-inductance of individual turns in a single layer spiral, the mutual inductance between adjacent turns, and the inter-turn parasitic capacitance.

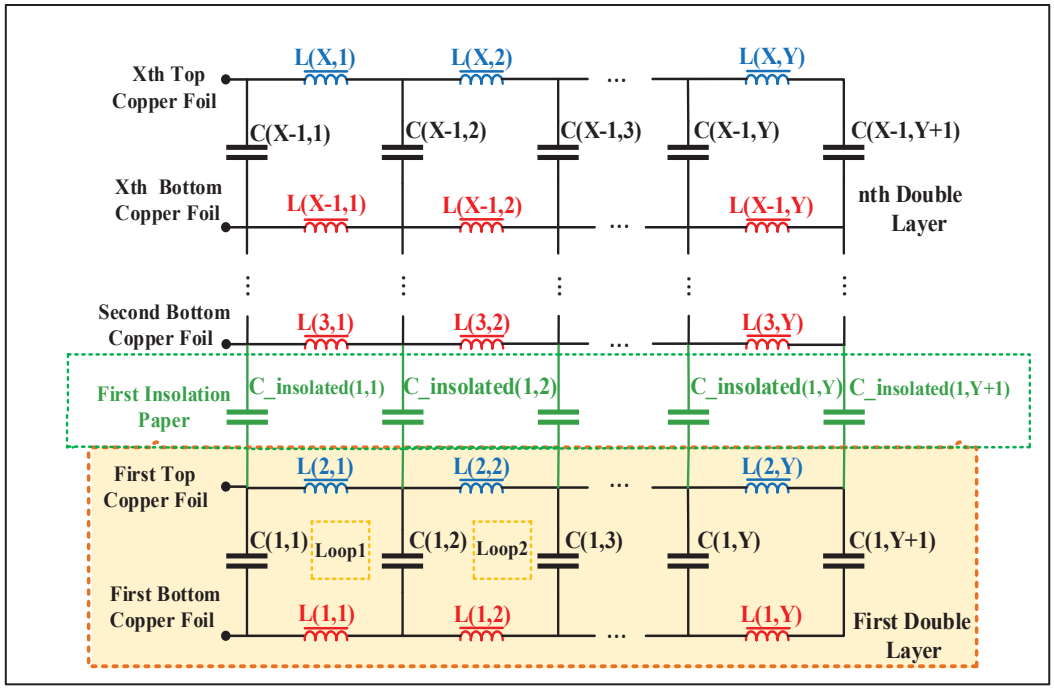

Figure 1.17 Equivalent circuit of a double-layer coil taken from Zahedi, Wang & Chandra (2025)

Resistive elements are incorporated to capture losses associated with copper conductors and dielectric materials, as illustrated in Figure 1.16. The values of the lumped parameters in this work are extracted from finite-element simulations rather than analytical expressions. This LC lumped modeling strategy has been extensively applied to the analysis of self-resonant structures, as it provides an intuitive representation of the underlying resonance mechanism while enabling circuit-level simplification. In many cases, the detailed lumped network can be further reduced to a more compact equivalent model, particularly for multi-layer self-resonant coils. For example, in the two-layer coil studied in (Zahedi, Wang & Chandra, 2025), each turn is initially represented by an inductive element, while distributed capacitors model the parasitic capacitance between overlapping turns across layers. Owing to the symmetry in geometry and material properties, the terminal loop can be equivalently reduced to a single inductance–capacitance pair. By extending this reduction iteratively, the complete two-layer coil is ultimately represented by a single equivalent inductor and capacitor, as depicted in Figure 1.17.

1.4.2 Inductance Modeling

Inductance modeling is a key step in the analysis and design of wireless power transfer coils, including both wound and planar spiral structures. For wound spiral inductors, empirical expressions are commonly used to estimate inductance based on basic geometric parameters. One widely used approximation expresses the inductance as (Wheeler, 1928):

$$L = \frac{4N^2R^2}{0.9r + H} \tag{1.1}$$

Where N is the number of turns, r is the winding radius, and H is the total axial length of the wound spiral. For planar spiral coils, several mature inductance models have been reported that provide sufficient accuracy for PCB-based implementations. In (Wheeler, 2006), two representative models are proposed. The first is a modified version of the classical Wheeler formula, expressed as

$$L_{MW} = K_1 \mu \frac{N^2 d_{avg}}{1 + K_2 \rho} \tag{1.2}$$

Where μ is the magnetic permeability, and the average diameter d_{avg} and fill ratio ρ are defined as:

$$d_{avg} = \frac{d_o + d_{in}}{2} \tag{1.3}$$

$$\rho = \frac{d_o - d_{in}}{d_o + d_{in}} \tag{1.4}$$

Where, d_o and d_{in} denote the outer and inner diameters of the spiral, respectively, while K_1 and K_2 are layout-dependent coefficients provided in Table 1.2. The second model in (Mohan, del Mar Hershenson, Boyd & Lee, 2002) is derived using a current-sheet approximation, where each side of the planar spiral is represented by an equivalent current sheet. The inductance is given by

Table 1.2 Coefficient for modified wheeler expression

Layout	K_1	K_2
Square	2,34	2,75
Hexagonal	2,33	3,82
Octagonal	2,25	3,55

Table 1.3 Coefficient for current sheet expression

Layout	C_1	C_2	C_3	C_4
Square	1,27	2,07	0,18	0,13
Hexagonal	1,09	2,23	0,00	0,19
Octagonal	1,07	2,29	0,00	3,55
Circle	1,00	2,46	0,00	0,20

$$L_{gmd} = \frac{\mu N^2 d_{avg} c_1}{2} \left(\ln \frac{c_2}{\rho} + c_3 \rho + c_4 \rho^2\right) \tag{1.5}$$

Where c_1, c_2, c_3 , and c_4 are empirical coefficients listed in Table 1.3. This model typically yields errors on the order of 1–2%, with most deviations below 3%. The error increases when the ratio of inter-turn spacing s to conductor width w becomes large, remaining below approximately 8% for $s \leq 3w$. More generally, the inductance of a multi-turn planar spiral coil for gradually varying geometries can be expressed as the sum of the self-inductance of individual turns and the mutual inductance between turns (Zahedi, Wang & Chandra, 2025):

$$L_S = \frac{\mu_o}{2Pi} + \sum_{\alpha=1}^{4n} l_n \left[\ln\left(\frac{2l_n}{w_n + t_n} \right) + 0.5 + \frac{(w_n + t_n)}{3l_n} \right] \tag{1.6}$$

Where, μ_o, t_n, w_n represent the permeability of free space, thickness and width of the nth coil

turn, respectively. l_n is the length of each turn. The calculation of positive and negative mutual inductance is given as follows:

$$\begin{cases} M_{Positive} = 4\sum_{i=1}^{N}\sum_{j=1}^{N-k} M(i,i+j) \\ M_{Negative} = 2\sum_{i=1}^{N}\sum_{j=1}^{N} M(i,j) \end{cases} \tag{1.7}$$

Where, positive mutual inductance signifies the presence of identical current directions in each coil section, whereas negative mutual inductance indicates opposing current directions in their respective coils. When these formulations are extended to multi-layer planar spiral coils, the equivalent inductance depends on both geometry and current distribution. For two-layer self-resonant coils, the total inductance can be well approximated using single-layer spiral models, provided that the overall coil height is much smaller than the conductor width (Li & Costinett, 2018). Although multi-layer structures introduce a vertical current component, this current is distributed over a large surface area, resulting in a relatively weak magnetic field compared with that generated by the circumferential current. As a result, the inductance is primarily governed by the circumferential current flow, and corrections to single-layer models are only required when the vertical magnetic field contribution becomes significant.

Beyond experimentally derived formulations, the inductive behavior of planar and self-resonant (SR) coils has been extensively investigated using analytical, field-based modeling techniques. These approaches describe electromagnetic coupling directly from fundamental principles and enable systematic evaluation of both self- and mutual inductance in multi-turn coil structures. While transmission-line representations have been employed to study resonance characteristics and current distribution in SR coils (Breitkreutz & Henke, 2013), such models do not yield explicit expressions for inductance. A rigorous analytical formulation is presented in (Zierhofer & Hochmair, 2002), where the mutual inductance between two parallel circular single-turn filamentary loops is expressed as:

$$M(a,b,\rho,d)=\pi\mu_o\sqrt{ab}\int_0^{\infty}J_1(x\sqrt{\frac{a}{b}})J_2(x\sqrt{\frac{b}{a}})J_0(x\frac{\rho}{\sqrt{ab}})\exp(-x\frac{d}{\sqrt{ab}})dx \tag{1.8}$$

Where $J_0(\cdot)$ and $J_1(\cdot)$ denote the zeroth- and first-order Bessel functions, respectively. This model assumes filamentary conductors and neglects the wire cross-sectional radius R, which is valid when $R/a \ll 1$. Under this assumption, the self-inductance of a single circular loop is approximated as (Greiner, 1991),

$$L(a,R)=\mu_o a(\ln(\frac{8a}{R})-2) \tag{1.9}$$

By superposition of all self- and mutual-inductance components, the equivalent self-inductance of a circular coil comprising N_a turns can be written as

$$L_a=\sum_{i=1}^{N_a}L(a_i,R)+\sum_{i=1}^{N_a}\sum_{j=1}^{N_a}M(a_i,a_j,\rho=0,d=0)(1-\delta_{i,j}) \tag{1.10}$$

Where $\delta_{i,j}$ is the Kronecker delta function. $\delta_{i,j}=1$ when i=j, $\delta_{i,j}=0$ when $i \neq j$. Similarly, the mutual inductance between two multi-turn coils with N_a and N_b turns, respectively, is obtained by summing the pairwise coupling between all constituent loops,

$$M_{ab}=\sum_{i=1}^{N_a}\sum_{j=1}^{N_b}M(a_i,a_j,\rho,d) \tag{1.11}$$

(Akyel, Babic & Kincic, 2002) investigates two analytical strategies for evaluating the mutual inductance between a circular coil and a thin conductive disk. In the first approach, shown in Figure 1.18, the disk is modeled as a continuous current distribution, leading to a double integral formulation for the mutual inductance,

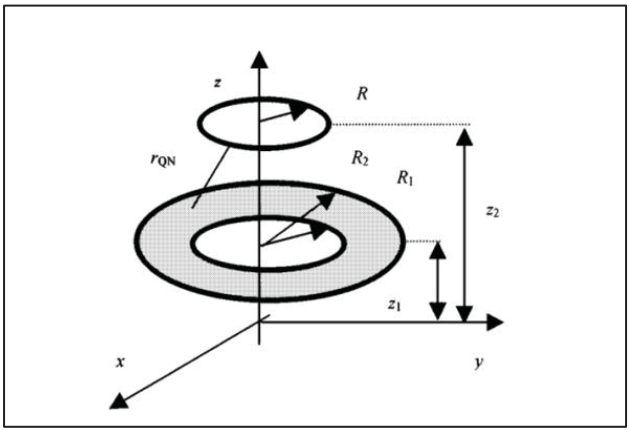

Figure 1.18 Mutual inductance modeling with circular filament coil-thin disk combination

$$M = \frac{\mu_o N_2 R}{(R_2 - R_1)} \int_0^{\pi} \int_{R_1}^{R_2} \frac{\cos\theta dr d\theta}{r_{QN}} \tag{1.12}$$

Where

$$r_{QN} = \sqrt{r^2 + R^2 - 2rR\cos\theta + (z_2 - z_1)^2} \tag{1.13}$$

And N_2 denotes the number of turns associated with the thin disk. An alternative formulation discretizes the disk into a set of filamentary loop meshes. By dividing the disk into 2N+1 concentric cells, the total mutual inductance is obtained through superposition (Kim, Levi, Zabar & Birenbaum, 1997),

$$M = \frac{N_2}{2N+1} \sum_{j=-N}^{j=N} M(j) \tag{1.14}$$

with the contribution of each filament loop given by

$$M(j) = \frac{2\mu_o \sqrt{RR(j)}}{k(j)} \left[(1 - \frac{k^2(j)}{2}) K(k(j)) - E(k(j)) \right] \quad \begin{cases} R_I = R, R_{II} = \dfrac{R_1 + R_2}{2} \\ R(j) = R_{II} + \dfrac{b}{2N+1} \\ k^2(j) = \dfrac{4RR(j)}{(R + R(j))^2 + z^2} \end{cases} \tag{1.15}$$

In this formulation, K(·) and E(·) denote the complete elliptic integrals of the first and second kind, respectively. Frequency-dependent impedance models in (Su, Liu, X & Hui, 2009; Hurley & Duffy, 1997) extend mutual inductance analysis to practical wireless charging systems incorporating ferrite shielding and metal plates, while accounting for both aligned and misaligned coil configurations. For non-circular coils, a geometric correction factor is commonly applied. As reported in (Jow & Ghovanloo, 2008), the mutual inductance is adjusted using

$$M = g\sum_{i=1}^{N_a}\sum_{j=1}^{N_b} M(a_i, a_j, \rho, d) \tag{1.16}$$

Where g compensates for shape-dependent effects and is typically 0.95, 1.0, and 1.1 for hexagonal, circular, and square coil pairs of equal size, respectively. Circular coils offer modeling simplicity, square coils maximize area utilization for compact PCB implementations, and hexagonal coils provide a balanced trade-off, making geometry selection primarily dependent on layout and fabrication constraints.

1.4.3 Capacitance Modeling

Accurate capacitance modeling is essential for optimizing self-resonant (SR) coil designs, as it directly determines the resonance frequency and electromagnetic performance. In SR coils employing coaxial-like structures (Son, Kim, Kim, Kim & Park, 2011), the capacitance formed between the inner and outer conducting rings can be approximated as (Pozar, 2005)

$$C_o = \varepsilon_o \varepsilon_r \frac{2\pi}{\ln(\frac{b}{a})} \tag{1.17}$$

Where a and b are defined in Figure 1.19. For most planar SR coils, the dominant capacitive

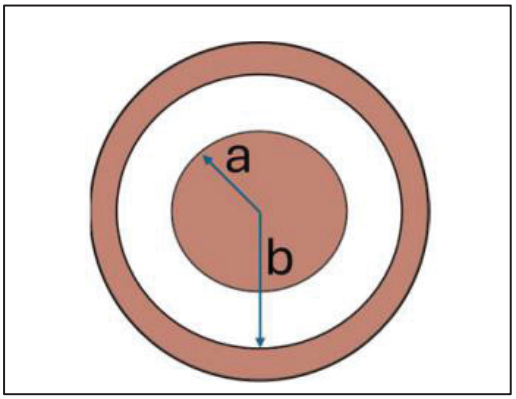

Figure 1.19 Coaxial-like capacitance generation between two circular layers

behavior can be represented using a parallel-plate capacitor model. The capacitance per unit length contributed by the overlapping copper area is given by

$$C_{Layer-Layer} = \frac{1}{(d/k_1\varepsilon_o A_{Total})} \tag{1.18}$$

Where, d, k_1, and ε_o represent the dielectric thickness, relative permittivity of the dielectric, and permittivity of free space, respectively. In addition to the capacitance generated in (1.18), the fringing electric field between turns, also contributes to the creation of parasitic capacitance, particularly when the distance between two turns is minimal. Several methods have been proposed to evaluate the fringing capacitance. Conformal-mapping-based approaches transform the capacitor geometry into an equivalent plane to derive analytical solutions, with progressively improved accuracy reported in (Langton, 1981). To better match specific coil geometries, (Li & Costinett, 2018) introduces an empirical scaling factor into these formulations. An alternative and more rigorous approach is the potential-theoretic method proposed by García (García-Moreno & Bandala-Sánchez, 2013), where the electric potential is expanded using a Fourier series,

$$\phi(x,y) = \sum_{n=1}^{\infty} A_n \sin(k_n y) e^{-k_n x} \tag{1.19}$$

with boundary conditions defined by

$$f(\xi)=\begin{cases} F_1(\xi): -T \le \xi \le -d-t \\ -v_o: -d-t \le \xi \le -d \\ \dfrac{v_o}{d}: -d \le \xi \le d \\ v_o: d \le \xi \le d+t \\ F_2(\xi): d+t \le \xi \le T \end{cases} \tag{1.20}$$

Where linear forms of $F_1(\xi)$ and $F_2(\xi)$ are adopted,

$$\begin{cases} F_1(\xi) = -v_o \dfrac{(T+x)}{(T-d-t)} \\ F_2(\xi) = v_o \dfrac{(T-x)}{(T-d-t)} \end{cases} \tag{1.21}$$

The Fourier coefficients and wavenumbers are

$$A_n = \frac{1}{T}\sum_{-T}^{T} f(\xi)\sin(k_n\xi)d\xi, \qquad k_n = \frac{n\pi}{T} \tag{1.22}$$

leading to the fringing capacitance expression

$$C_f = 2\sum_{n=1}^{\infty} \varepsilon_o \varepsilon_r \frac{A_n}{v_o}(1-e^{-k_n(w_f+d)}) \tag{1.23}$$

Where w_f denotes half the width difference between the plates and t is the copper thickness. The accuracy of the reviewed capacitance models is validated against 2-D electric-field simulations using FEMM. A similar capacitance modeling framework has been presented in (Zahedi, Wang & Chandra, 2025) for multilayer self-resonant PCB coils, where the total

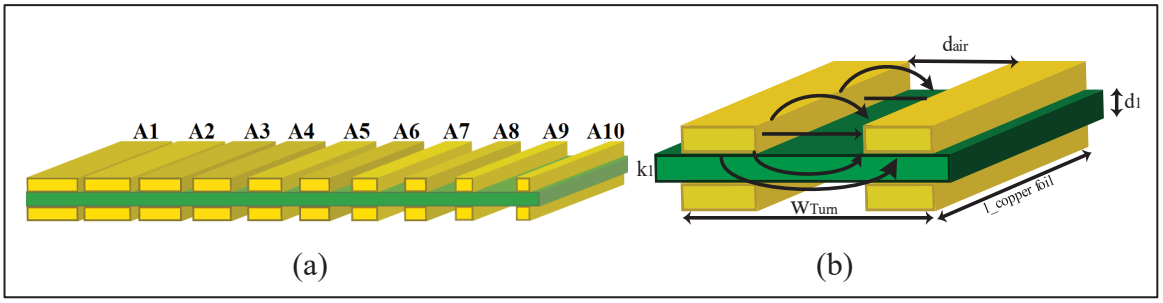

Figure 1.20 Capacitance calculation of proposed coil structure. (a) Layer to layer, (b) Parasitic capacitance

effective capacitance was obtained by combining the layer-to-layer coupling between adjacent conductive layers with the parasitic turn-to-turn fringing capacitance. Following this approach, the present work formulates the capacitance model by explicitly accounting for both contributions and extending the analysis to the proposed multilayer geometry. As shown in Figure 1.20 (b), the fringing electric field implies to two adjacent turns with the air and dielectric. C_{air} and $C_{\text{dielectric}}$ correspond to the capacitance involving air and dielectric, respectively, which can be calculated based on conformal mapping and the assumption of the magnetic wall (Vendik, Zubko & Nikol'Skii, 1999) as follows:

$$\begin{cases} C_{air} = \varepsilon_o l_{copper-foil} F(k_o) \\ k_o = d_{air} / w_{Turn} \end{cases} \tag{1.24}$$

$$\begin{cases} C_{Dielectric} = 0.5\varepsilon_o l_{copper-foil} (k_1 - k_o) F(k_1) \\ k_1 = \tanh\left(\frac{\pi d_{air}}{4d_1}\right) / \tanh\left(\frac{\pi w_{Turn}}{4d_1}\right) \end{cases} \tag{1.25}$$

Where,

$$F(k_i) = \begin{cases} \pi^{-1} \ln\left[2\frac{1+(1-k_i^2)^{0.25}}{1-(1-k_i^2)^{0.25}}\right] & \text{for } k_i \le 0.5 \\ \pi\left[\ln\left(2\frac{1+\sqrt{k_i}}{1-\sqrt{k_i}}\right)\right]^{-1} & \text{for } k_i \ge 0.5 \end{cases} \tag{1.26}$$

Consequently, the parasitic capacitance between two turns is calculated as given:

$$C_{Parasitic-T-T} = C_{air} + C_{Dielectric} \tag{1.27}$$

The overall capacitance of a multi-layer PCB coil, with insolated paper between each two-layer, can be described as:

$$C_{Total} = nC_{Layer-layer} + (n-1)C_{Insolated} + C_{air} + C_{Dielectric} \tag{1.28}$$

Where, n is the number of layers. Therefore, based on the above equation, increasing the number of layers allows for the production of a larger capacitance, consequently resulting in lower resistance and a resonant frequency. The self-resonant frequency is determined by the desirable compensation capacitance between coil layers while the undesirable parasitic capacitance will slightly decrease the self-resonant frequency.

1.4.4 Copper Loss Modeling

1.4.4.1 Low-Frequency Conduction Loss

At low frequencies, copper loss is dominated by the DC resistance, which depends on conductor length, cross-sectional area, and material resistivity. For a single-layer planar coil, the DC resistance is given by (Sullivan & Beghou, 2013)

$$R_{lf} = \frac{2\pi\rho}{\ln(\frac{r_2}{r_1}).t} \tag{1.29}$$

where t, r_1, r_2, and ρ denote the copper thickness, inner radius, outer radius, and resistivity, respectively. In multilayer self-resonant (SR) coils, the equivalent DC resistance depends on

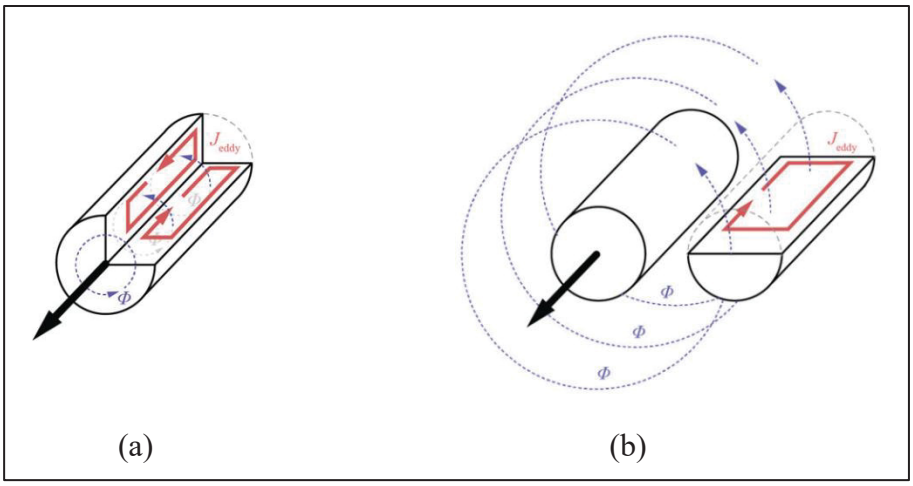

Figure 1.21 Eddy currents from (a) skin effect (b) proximity effect

current sharing among layers. For example, the two-layer SR coil in (Li & Costinett, 2018) distributes current evenly, resulting in an equivalent DC resistance equal to two-thirds of that of an equivalent single-layer coil. Increasing the number of layers further reduces the DC resistance, which is a key contributor to the high-quality factor of SR coils.

1.4.4.2 High-Frequency Conduction Loss

At high frequencies, copper loss is dominated by eddy-current effects, namely skin and proximity effects. The skin effect arises from the self-induced magnetic field within the conductor, forcing the current to concentrate near the surface. The proximity effect is caused by external magnetic fields from neighboring conductors, which redistribute the current toward regions where the normal magnetic field component is strongest, as illustrated in Figure 1.21. A key parameter governing these effects is the skin depth,

$$\delta = \sqrt{\frac{\rho}{\pi \mu_o f}} \tag{1.30}$$

Where ρ, μ_o, and f denote the conductor resistivity, permeability, and operating frequency, respectively.

1.4.4.2.1 Skin Effect Losses

In self-resonant and meta surface-assisted wireless power-transfer systems, flat rectangular copper traces are commonly employed instead of round conductors. Such planar structures enable higher copper fill-factor and efficient multilayer integration while also facilitating the formation of inter-layer parasitic capacitance. However, under high-frequency excitation, the current density within these rectangular foil conductors becomes non-uniform due to electromagnetic diffusion. This phenomenon, known as the skin effect, forces the current to concentrate near the conductor surface, thereby reducing the effective conduction area and increasing the AC resistance. For planar foil conductors, a widely accepted analytical description in (Y. Eo & Eisenstadt, 1993) and (Yue & Wong, 2000), assumes that the current density decays exponentially with depth into the conductor. Under sinusoidal steady-state excitation, the total current flowing through a conductor of thickness t can be written as

$$I_{total} = \int_0^t j(0)\exp\left(-\frac{x}{\delta}\right)dxj(0)\delta_x \tag{1.31}$$

where δ is the classical electromagnetic skin depth. The corresponding effective penetration depth can be calculated as follows

$$\delta_x = t_{eff} = \delta(1-\exp\left(-\frac{x}{\delta}\right)) \tag{1.32}$$

and the AC resistance associated with the skin effect may be expressed as

$$R_{skin} = F(f)R_{DC}I^2 \tag{1.33}$$

where ρ, l, and w denote the resistivity, conductor length, and width, respectively. This classical formulation, which has been extensively employed in the modeling of planar spiral coils, captures the exponential current-crowding inside the conductor while neglecting

magnetic interaction between adjacent turns. More advanced analytical formulations in (Zahedi, Wang & Chandra, 2025) extend the above skin-depth model by explicitly incorporating the influence of coil geometry, particularly the turn pitch and spacing, which modify the local magnetic-field distribution. In these models, the AC resistance attributed to the skin effect can be written as

$$R_{Skin} = \sum_{n=1}^{N} \frac{l_n}{\tau \sigma w_n \alpha^{0.5} \beta} \tag{1.34}$$

Where, σ and p_n stand for the coil's conductivity and pitch of coil, respectively. In (1.35), the parameters α, β, and τ are expressed as:

$$\alpha = 1 / \pi \sigma \mu_o f \quad , \quad \beta = (1 - e^{-\frac{t_n}{p_n}}) \quad , \quad \tau = (1 + \frac{t_n}{w_n}) \tag{1.35}$$

where t_n and p_n represent the thickness and pitch of the n-th turn, and μ is the magnetic permeability. In this formulation, β_n acts as the current-penetration correction term associated with the skin effect, whereas τ_n introduces the influence of conductor pitch and spacing, implicitly capturing part of the proximity-induced current redistribution.

1.4.4.2.2 Proximity Effect Losses

The proximity effect arises from the magnetic fields produced by neighboring turns, which distort the current distribution inside the conductor and increase the AC resistance. Early analytical treatments estimated these fields using filamentary winding assumptions and the Biot–Savart law (Lu & Ngo, 2019); however, this approach becomes inaccurate for wide planar traces or tightly spaced windings, where the field strongly depends on the internal current distribution (Du, Li & Dujić, 2021). A more rigorous analysis of current crowding was proposed in (Smith, 1972), where integral equations were solved for the transverse current distribution, although the study was limited to two parallel round conductors. Another modeling strategy applies AC resistance factors to represent eddy-current effects in laminated

conductors placed next to high-permeability cores, later refined using field-weakening and current-crowding coefficients (Stein, Kyaw & Sullivan, 2018). This approach still relies on finite-element calibration. A classical proximity-loss expression for laminated conductors is given in (Sullivan & Beghou, 2013):

$$P_{prox} = \frac{B_{pk}^2 w^2 t^2}{24\rho} V \tag{1.36}$$

Where B_{pk} , w, t, and V denote the peak flux density, width, thickness, and copper volume. The key difficulty is determining the local magnetic-flux distribution. For multilayer windings, (Sullivan & Beghou, 2013) expresses the flux as a function of radial and vertical position, while (J. Li, 2018) employs a 2-D analytical solution based on Maxwell's equations (Fang, Wu & Sin, 2015). These models are most accurate for thick-foil windings and lose precision when the width-to-thickness ratio increases. To better represent PCB geometries, (Lope, Carretero, Acero, Alonso & Burdio, 2013) decomposes the surrounding magnetic field into orthogonal components. The resulting per-unit-length proximity resistance in the x- and y-directions is

$$\begin{cases} R_{proxu,l,x} = \dfrac{2\pi}{\sigma} \varphi_{prox}\left(\dfrac{w}{\delta}, \dfrac{h}{\delta}\right) H_{o,x}^2 \\ R_{proxu,l,y} = \dfrac{2\pi}{\sigma} \varphi_{prox}\left(\dfrac{w}{\delta}, \dfrac{h}{\delta}\right) H_{o,y}^2 \end{cases} \tag{1.37}$$

Where σ is conductivity, δ is skin depth, and w, h are conductor dimensions. The geometry-dependent factor ϕ_{prox} is extracted using 2-D FEM simulations in uniform fields (Du, Li & Dujić, 2021). Results show that square cross-sections mitigate proximity loss at high frequency, while wide flat conductors experience the highest losses when their long side faces the magnetic field. Since a uniform field is assumed, accuracy may degrade in dense windings with strong spatial field gradients. A unified proximity-loss representation is reported in (Mühlethaler, 2012):

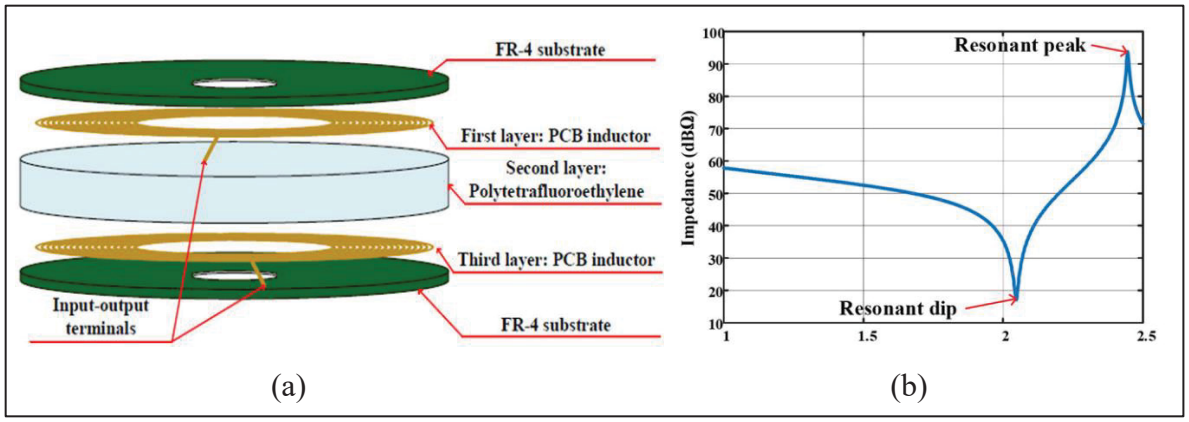

Figure 1.22 (a) sandwich structure utilizing low-cost PCB substrate (b) fabricated sample impedance plot taken from Li, Wu, Yucel & Hui (2023)

$$P_{proximity} = G(f) R_{dc} H_e^2 \tag{1.38}$$

Where G(f) is obtained using Bessel-function solutions. Similar frequency-dependent correction-factor approaches are also adopted in (Zahedi, Wang & Chandra, 2025), where inter-turn field interaction is embedded into the model. These works consistently show that strong orthogonal flux components near conductor edges significantly amplify proximity losses; therefore, minimizing conductor thickness and carefully selecting winding geometry are essential for reducing current crowding. As in previous empirical formulations, the analysis assumes a locally uniform external magnetic field.

1.4.4.3 Dielectric Losses

The capacitive loss in self-resonant coils is typically modeled using the dielectric loss tangent at the operating frequency, where the equivalent resistance is expressed as

$$R_C = \frac{D_g}{2\pi f_o C} \tag{1.39}$$

Several dielectric materials have been reported for SR-coil fabrication in literature reviews. PCB laminates such as PTFE (Teflon) and Rogers ceramic substrates exhibit significantly lower loss tangent than FR-4, although their higher cost is a major drawback. Low-loss

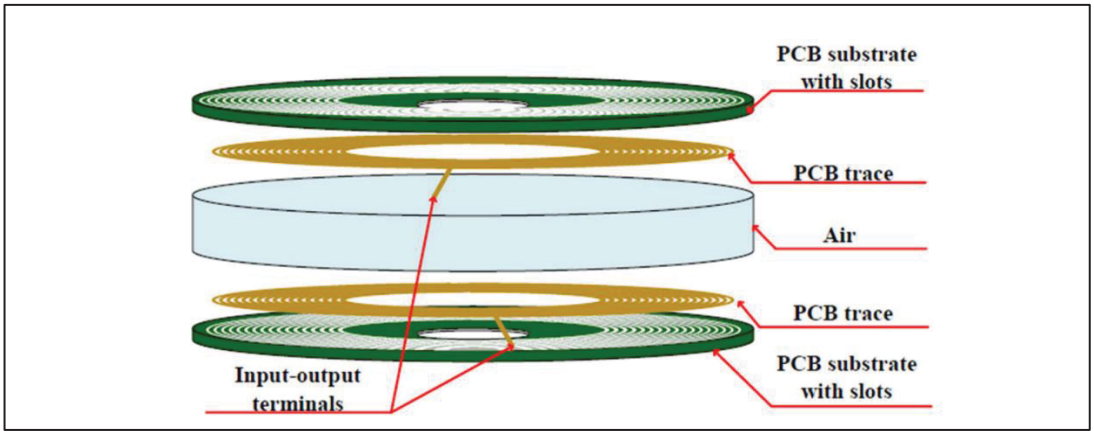

Figure 1.23 Structure of a new design of PCB resonator based on two PCBs separated with an air gap, and with air trenches between adjacent turns taken from Kerui, Wu, Yucel, & Hui, (2023), and Li, Wu, Yucel & Hui (2023)

dielectrics are generally preferred, but FR-4 may still be used as a structural support layer provided that regions of high electric-field intensity are confined to the low-loss dielectric. For example, in (Stein, Kyaw & Sullivan, 2017), PTFE is employed as the resonant dielectric while FR-4 serves mainly as a mechanical substrate. A similar concept is implemented in (Li, Kerui, et al., 2023), using a multi-turn structure in which the displacement current is intentionally directed through the low-loss dielectric (illustrated in Figure 1.22). The resulting 210 mm coil exhibits both series and parallel resonances, achieving quality factors of 195 at 2.0 MHz and 314 at 2.4 MHz. However, even when PTFE forms the dominant capacitive path, the longitudinal voltage drop along each winding still produces turn-to-turn electric fields within the FR-4 substrate. To further reduce dielectric loss, (Kerui, Wu, Yucel, & Hui, 2023) introduces air trenches between adjacent turns, as shown in Figure 1.23. Finite-element analysis indicates that dielectric loss accounts for approximately 57 % of total loss when FR-4 alone is used. This ratio decreases to 18 % when air is used as the dielectric medium and to 8 % when air trenches are added.

A comparative study of dielectric films including mica, polypropylene, polyimide, and fiberglass was reported in (Jiang et al., 2021). At ≈300 W output power, polypropylene achieved the highest efficiency (82 %), compared with 79 % for polyimide and 78 % for

fiberglass. A cost comparison in (Kerui, Wu, Yucel, & Hui, 2023) shows that a 210-mm FR-4 board costs $4.79, whereas an equivalent Rogers RO4350B laminate costs $72.22. Dielectric strength is also a key design consideration. In (R. Qin, 2022), RO3003 laminates were patterned via chemical etching for SR-coil fabrication. Partial-discharge testing demonstrated that a 1.5mm thick laminate could withstand up to 4.4 kV RMS before reaching the 30pC threshold, more than twice the 1.9 kV RMS operating voltage at 6.6 kW. To satisfy UL60950 insulation clearance requirements for 2 kV RMS ratings, a minimum creepage spacing of 20 mm between copper traces and nearby holes was maintained. An alternative configuration eliminates separate dielectric films by allowing the magnetic material itself to serve as the dielectric, with capacitance formed between the copper winding and a metal plate (Yin et al., 2023). This structure significantly suppresses stray electric-field radiation, but requires the ferrite to exhibit high resistivity and low dielectric loss.

1.4.5 Power Capability Modeling

The power capability of a self-resonant inductive link is determined by the mutual coupling, self-inductances, and excitation current in the primary and secondary coils. In general, the transferable power can be expressed as:

$$P = wMI_{primary}I_{secondary} = 2\pi fk\sqrt{L_{Primary}L_{secondary}}.I_{primary}I_{secondary} \tag{1.40}$$

where f is the operating frequency, M is the mutual inductance, k is the coupling coefficient, and $I_{primary}$, $I_{secondary}$, $L_{primary}$, and $L_{secondary}$ denote the primary and secondary currents and inductances, respectively. From (1.40), it is evident that increasing the operating frequency enhances the reactive power exchange and therefore improves the power-density potential of SR-coil systems. This trend is reflected in several implementations: the SR structure reported in (Mohammad et al, 2023) was later demonstrated to deliver 1 kW at 6.78 MHz (Gu Lei et al., 2020), although the attainable power is ultimately restricted by the relatively small single-turn inductance (typically < 1 μH). A more balanced design operating at 3 MHz is presented in (Qin, Li & Costinett, 2021), achieving 6.6 kW. Such multi-MHz operation has been

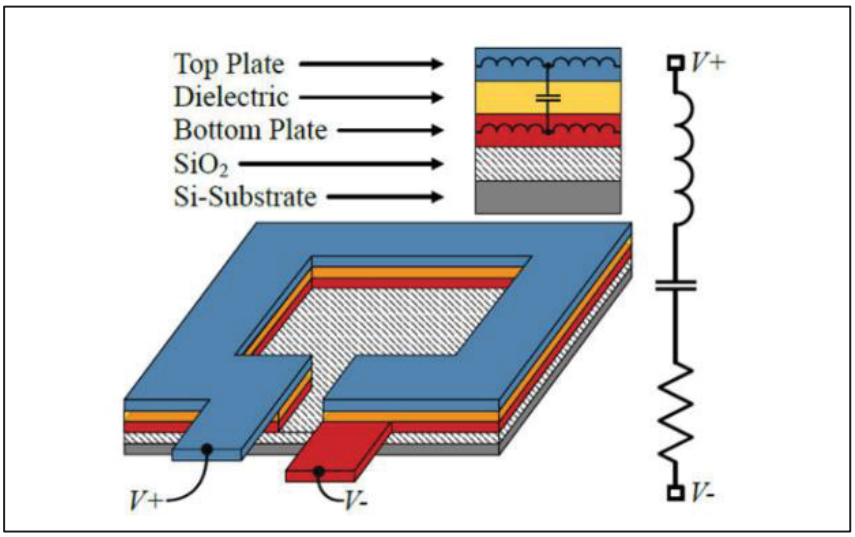

Figure 1.24 2-layer single turn SR coil in typical CMOS process

facilitated by the availability of wide-bandgap switching devices such as GaN FETs, which allow efficient high-frequency conversion.

Besides increasing frequency, the achievable power can also be improved by enlarging the coil size, which strengthens magnetic coupling over a given air gap. A notable demonstration of this principle is the 2-m-diameter SR coil developed at Oak Ridge National Laboratory (Mohammad et al., 2023). The structure employs a 6-inch-wide copper-foil winding resonant at 6.78 MHz and is capable of transferring 300 W across a 2-m separation with 62 % efficiency. Although SR coils have been explored for high-power transfer, the same physical principle is also applicable to ultra-low-power systems. An example is the two-layer single-turn SR coil implemented in a 0.18μm CMOS process in 85, which delivers less than 1 W with a peak efficiency of 85.5 %. In this design, the parasitic capacitance between metal layers forms the resonant network (Figure 1.24). One of the practical benefits of self-resonance in this integrated geometry is that it promotes a more uniform current distribution among multiple parallel traces. As illustrated in Figure 1.25 (a), a non-resonant multi-trace inductor suffers from current crowding toward the lowest-impedance inner turns, whereas the SR configuration of Figure 1.25(b) introduces capacitive reactance that equalizes the current density.

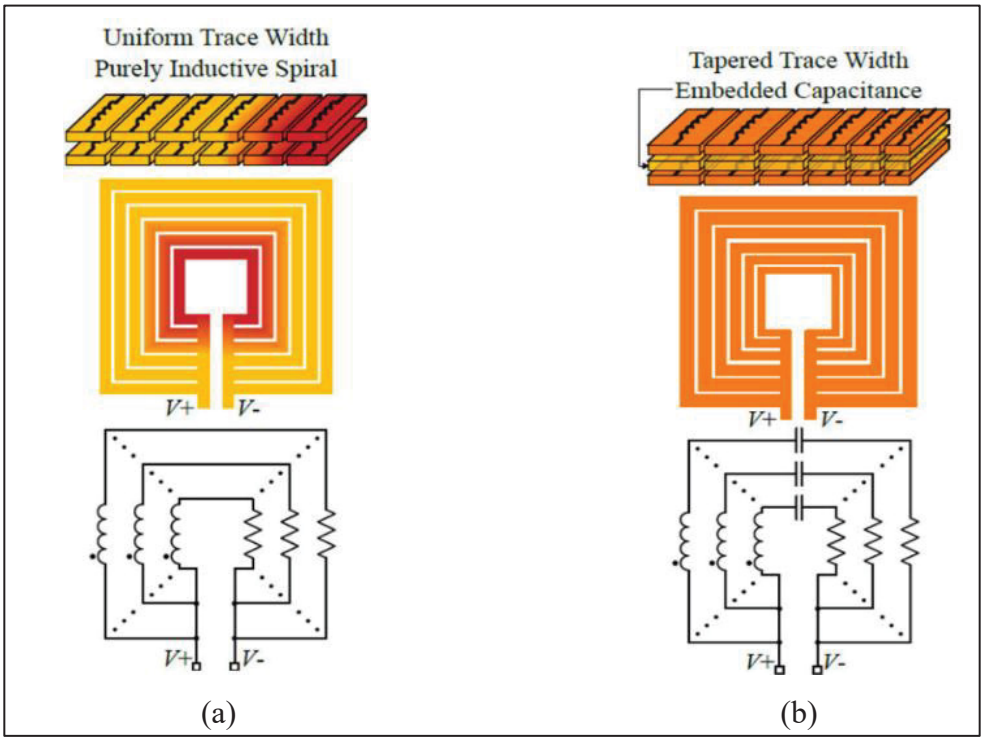

Figure 1.25 2-layer single turn SR coil current distribution comparison (a) 2-layer inductor (b) 2-layer SR coil

Self-resonant inductive structures have also been adapted for very high-frequency, low-power applications such as UHF-RFID. In (Pei et al., 2020), the resonant frequency is tuned to 433 MHz within the ISM band by adjusting the spacing between winding segments. Since the resonance in this case relies on extremely small parasitic capacitances, care must be taken to avoid additional stray capacitances from nearby dielectrics or packaging materials.

1.4.6 EMI Consideration

Electromagnetic interference performance of self-resonant coils has been experimentally compared with conventional wireless-charging coils. Measurements in (Jiang et al., 2020) show that, at comparable operating conditions, the radiated magnetic field is essentially unchanged, while the electric-field level is reduced in multi-layer SR coils due to shielding produced by stacked copper foils. Additional analysis of square SR-coil structures in (Xiang et al, 2024) confirms that the magnetic flux remains well confined by nanocrystalline shielding layers, with the maximum electric-field strength remaining below regulatory limits. Despite

this, leakage electric fields may still interact with nearby sensitive electronics such as capacitive touch systems (Yang, Cooper, Elkhouly, Narayan & Ren, 2015) or introduce extra dielectric losses in surrounding materials. To mitigate such effects, distributed capacitance SR-coil structures have been proposed (Qin, Li, Sun & Costinett, 2023), where the current periodically crosses the dielectric layer, reshaping the current path and suppressing fringing electric fields. Existing studies mainly address near-field behavior; comprehensive far-field EMI assessment and regulatory validation are still limited. Therefore, continued investigation will be necessary to fully establish EMI compliance of SR-coil structures.

1.5 State of the Art and Research Gap

Self-resonant wireless power transfer (SRWPT) has recently attracted increasing attention as an alternative to conventional capacitor-compensated wireless power transfer systems. By embedding the resonant mechanism directly within the electromagnetic structure of the coil, SRWPT eliminates discrete compensation capacitors, thereby improving structural robustness, reducing voltage stress on passive components, and simplifying system integration. As a result, a wide range of self-resonant coil structures has been proposed, including bifilar coils, helical resonators, coaxial resonators, multilayer wound coils, and planar PCB-based resonators. Despite these advances, the current state of the art still exhibits several fundamental limitations that restrict the practical deployment of self-resonant WPT systems.

A primary challenge arises from the intrinsically high self-resonant frequency of planar coils. In most PCB-based self-resonant structures reported in the literature, the distributed capacitance generated between adjacent turns is relatively small. Consequently, the resulting self-resonant frequency typically lies in the MHz range, which is significantly higher than the operating frequency commonly preferred for medium-power WPT platforms such as electric vehicle chargers, industrial wireless charging systems, and motor-drive applications, where frequencies below approximately 150 kHz are generally adopted to limit switching losses and

electromagnetic interference. Therefore, achieving low-frequency self-resonance without relying on external capacitors remains a critical design challenge.

In addition, although multilayer coil configurations have been explored to increase intrinsic capacitance, a systematic electromagnetic design methodology capable of simultaneously achieving low resonant frequency, high quality factor, and compact coil structure is still lacking. Increasing capacitance often leads to increased copper losses, stronger parasitic coupling, and larger physical dimensions, creating a complex multi-objective design trade-off that has not yet been comprehensively addressed.

Another limitation concerns the insufficient understanding of the role of coil geometry in self-resonant systems. While different planar geometries have been individually investigated in previous studies, a rigorous and systematic comparison of commonly used geometries such as circular, square, hexagonal, and octagonal coils under identical operating conditions remains largely absent. Since coil geometry simultaneously influences inductance distribution, distributed capacitance, AC resistance, resonant frequency, and magnetic coupling, a comprehensive investigation is essential to establish clear electromagnetic design guidelines for SRWPT systems.

Furthermore, efficiency degradation under weak magnetic coupling remains a critical issue in conventional two-coil SRWPT configurations. As the air gap increases or misalignment occurs, the coupling coefficient decreases significantly, leading to rapid efficiency degradation and reduced power transfer capability. Although relay coils and multi-coil architectures have been explored in capacitor-compensated WPT systems, their integration into self-resonant architectures has not yet been systematically investigated.

Finally, SRWPT solutions for footprint-constrained receivers remain extremely limited, particularly in biomedical wireless power transfer applications. Implantable medical devices require highly compact receiver coils, which inherently restrict achievable inductance and reduce coupling capability. Consequently, maintaining efficient wireless power transfer in such size-constrained environments remains an open research problem.

These limitations highlight the need for new electromagnetic design strategies capable of enabling low-frequency, high-efficiency, and structurally compact self-resonant WPT systems suitable for practical applications.

1.6 Originality of the Research

To address the aforementioned challenges, this thesis introduces several original contributions that advance the design and performance of self-resonant wireless power transfer systems.

First, a multilayer PCB self-resonant coil architecture is proposed to enable intrinsic resonance at low frequencies without the use of external compensation capacitors. By strategically enhancing inter-layer capacitive coupling while preserving strong inductive behavior, the proposed structure significantly increases the effective distributed capacitance of the coil. As a result, the intrinsic resonant frequency can be shifted toward the sub-150 kHz region, which is suitable for medium-power WPT systems.

Second, this research introduces an electromagnetic layout optimization methodology based on Track-Width Ratio (TWR) and Track-Gap Ratio (TGR). These layout parameters are systematically optimized to mitigate AC resistance caused by skin and proximity effects in multilayer PCB coils. The proposed optimization framework significantly improves the coil quality factor while maintaining compact geometry and manufacturability.

Third, this work presents a comprehensive comparative investigation of planar coil geometries in self-resonant wireless power transfer systems. Circular, square, hexagonal, and octagonal coils are analyzed under identical operating conditions. Their impact on inductance, distributed capacitance, AC resistance, resonant frequency, quality factor, magnetic coupling, and overall power transfer efficiency is evaluated using analytical modeling, finite-element electromagnetic simulations, and experimental validation. The results establish practical design guidelines for geometry selection in SRWPT systems.

Fourth, a self-resonant three-coil wireless power transfer architecture is developed to overcome efficiency degradation under weak coupling conditions. By introducing an intermediate resonant coil, the proposed architecture increases the effective coupling coefficient and

enhances the reflected impedance seen by the transmitter. This approach improves power transfer efficiency at extended distances while preserving the capacitor-less nature of the self-resonant system.

Finally, a compact self-resonant three-coil receiver architecture for biomedical applications is proposed. By structurally integrating auxiliary coils within the receiver design, the effective inductance is significantly increased without enlarging the receiver footprint. This enables improved wireless power transfer efficiency in size-constrained biomedical platforms.

Through these contributions, the research advances the electromagnetic design methodology of self-resonant wireless power transfer systems and demonstrates the feasibility of high-efficiency, capacitor-less WPT architectures operating at low frequency for both medium-power and compact biomedical applications.

CHAPTER 2

A MUILTILAYER PCB COIL FOR SELF-RESONANT WIRELESS POWER TRANSFER SYSTEMS

Neda Zahedi Saadabad [a], Qingsong Wang [a], Ambrish Chandra [a]

[a] Department of Electrical Engineering, École de technologie supérieure,
1100 Notre-Dame Ouest, Montréal, Québec, Canada H3C1K3

Article published in *Journal of IEEE Transaction on Industrial Electronics, September 2025* vol. 73 (2025), available at https://ieeexplore.ieee.org/abstract/document/11178063

Abstract

This paper presents an innovative PCB coil for self-resonant wireless power transfer (SRWPT) systems. Parasitic capacitance between adjacent coil layers is used for compensation, allowing the elimination of physical capacitors normally used in the traditional RWPT systems. Multilayer design that connects multiple PCB coils in parallel is implemented to reduce the resonant frequency. Through applying track-width-ratio and track-gap-ratio, the AC resistance of the proposed PCB coil is significantly reduced and the proposed SRWPT system achieves a high efficiency accordingly. The equivalent circuit and theoretical models of inductance and capacitance of the proposed PCB coil have been established. Finite element method is employed to optimize the coil and simulate its performance. A SRWPT system based on the proposed coil is established, and experimental tests have been conducted to study its performance. The results show that the proposed system achieves a resonant frequency below 150 kHz, a coil-to-coil efficiency of 94.7%, and a high-quality factor of 123.

2.1 Introduction

Wireless power transfer (WPT) systems are attracting increasing attention due to their convenient and reliable energy transfer without direct connections. These systems rely on magnetic coupling between the transmitter and receiver coil pads and are widely applied in various applications like medical devices (Shah, Zada, Shah, Basir & Yoo, 2023), home appliances (Sezer, Odabas, Sinirlioglu, Kaya & Altintas, 2021) and electric vehicles (Zhang et al., 2023). One of the most promising applications of WPT is in Automated Guided Vehicles (AGVs). These autonomous transport units, widely used in industrial settings like warehouses and manufacturing plants, are typically powered by batteries (Li Xiaofei et al, 2023; Mao, Lin, Su & Zhang, 2023; Matsumoto, Shibako & Neba, 2017; Zhang Yiming et al., 2024). WPT offers a solution by allowing AGVs to charge without physical connectors, enabling continuous operation while moving or stationary. Additionally, the absence of exposed electrical contacts makes WPT an ideal choice for harsh environments like factories, where moisture, dust, and oils are prevalent.

Extensive research has been conducted on wireless power transfer (WPT) for AGVs, with various approaches addressing key challenges such as misalignment compensation, power optimization, and mutual inductance stabilization. For instance, (Li Xiaofei et al, 2023) develops a WPT system with self-alignment and output current control, achieving 89.1% efficiency. In (Mao, Lin, Su & Zhang, 2023), a dual-receiver coil mechanism mitigates misalignment, enhancing power transfer. Reference (Matsumoto, Shibako & Neba, 2017) introduces a contactless power transfer system that replaces conventional AGV batteries, employing advanced control strategies to deliver over 100 W at more than 80% efficiency. Additionally, (Zhang Yiming et al., 2024) presents a dynamic WPT system utilizing a dual-receiver magnetic coupler and an I-type solenoid coil, stabilizing mutual inductance fluctuations within 3.6%, confirming its practicality.

Despite extensive research in this field, many existing solutions rely on conventional coil designs that require external compensation circuits to maintain resonance, as leakage flux increases with transmission distance (Shevchenko et al., 2019). While simple compensation networks use single capacitors (Yue et al., 2023; Saket, Shafiei & Ordonez, 2016), more

advanced configurations like LCC (Hou et al., 2022), LCL (Gao, Dong, Yin, Zhang & Cui, 2022), and P-CLC (Wang, Wang, Lu, Guo & Wang, 2022) circuits are often necessary, adding complexity, cost, and size to the system. Moreover, the magnification of voltage and current across compensation capacitors at resonance heightens the risk of breakdown, compromising system reliability. In contrast, PCB-based self-compensated coils address these challenges by generating compensation capacitance from neighboring turns or parallel plate-shaped structures, eliminating the need for bulky external compensation, thus offering a more compact, efficient, and reliable alternative (Zahedi, Wang & Chandra, 2023; Zahedi, Wang & Chandra, 2023; Zahedi, Wang & Chandra, 2025). Various coil structures have been explored, including bifilar coils (de Miranda & Pichorim, 2016) spaced spiral coils (Kim & Choi, 2022), and two-layer spiral configurations with a dielectric layer (Li & Costinett, 2018; Cote Nathis et al., 2022), all operating at MHz frequencies to enable efficient power transfer. To optimize static AGV charging, switching to low-frequency operation is essential for better power transfer efficiency. Due to the proportionality between intra-winding capacitance and the facing area of adjacent conductors, constrained by the coil size, it is difficult to obtain a large intra-winding capacitance. This leads to SRWPT systems having a high resonant frequency, typically in the megahertz range (de Miranda & Pichorim, 2016; Kim & Choi, 2022; Li & Costinett, 2018; Cote Nathis et al., 2022). To reduce resonant frequency, multilayer coils that connect multiple coil layers in parallel have been proposed (Wang, Saket, Troy & Ordonez, 2020; Lee, Kim & Moon, 2021). These coils have achieved a resonant frequency lower than 150kHz, but the reported transfer power and efficiency were only 67W with 65%, and 60W with 75%, respectively. In (Jiang et al., 2020), multi-layer coil configurations with distinct dielectrics were experimented and compared, demonstrating the system's capability to transfer 360W with an efficiency of 82%. However, this coil has a low-quality factor of 23, and only the receiver is self-resonant while the transmitter has a traditional compensation circuit.

This paper proposes a new multilayer PCB coil that connects six double-layer PCBs in parallel for SRWPT systems. The multilayer configuration significantly increases the intra-winding

capacitance and leads to a resonant frequency of 147kHz. In order to increase quality factor and efficiency, a novel coil layout with both track-width-ratio (TWR) and track-gap-ratio (TGR) is implemented, which reduces the AC resistance of the coil by suppressing the proximity effect. The following sections of this paper are organized as follows: Section II introduces the proposed coil topology and theoretical models. Section III provides details on the design and optimization. Experimental validation is presented in Section IV, and Section V concludes the paper.

2.2 Coil Topology and Theoretical Models

2.2.1 Coil Topology

Fig. 1(a) depicts the double-layer PCB with a square spiral coil layout. A dielectric layer is inserted between the upper and lower coils to generate intra-winding capacitance. Both the upper coil and lower coil have two terminals, among which terminals 2 and 3 are left open and terminals 1 and 4 are connected to the AC source for the transmitter and to the load for the receiver. The AC current flows distributedly from one terminal to the other and crosses the dielectric layer, thus creating a series LC resonant tank. To increase capacitance and lower the resonant frequency, six double-layer PCB coils separated by insulation papers are connected in parallel, as illustrated in Fig. 1(b). All terminals 1 are connected, as are the terminals 4, while terminals 2 and 3 on all layers are left open. Terminals 1 and 4 on the transmitter are connected to the AC power source, and terminals 1 and 4 on the receiver are connected to the load, as shown in Fig.2. Since the center area of the coil has the largest magnetic intensity, which significantly increases the AC resistance, a hollow spiral winding pattern is adapted. Moreover, TWR and TGR are applied to the proposed coil, which means that from the inside to the outside, the coil width gradually increases, and the gap between adjacent turns gradually

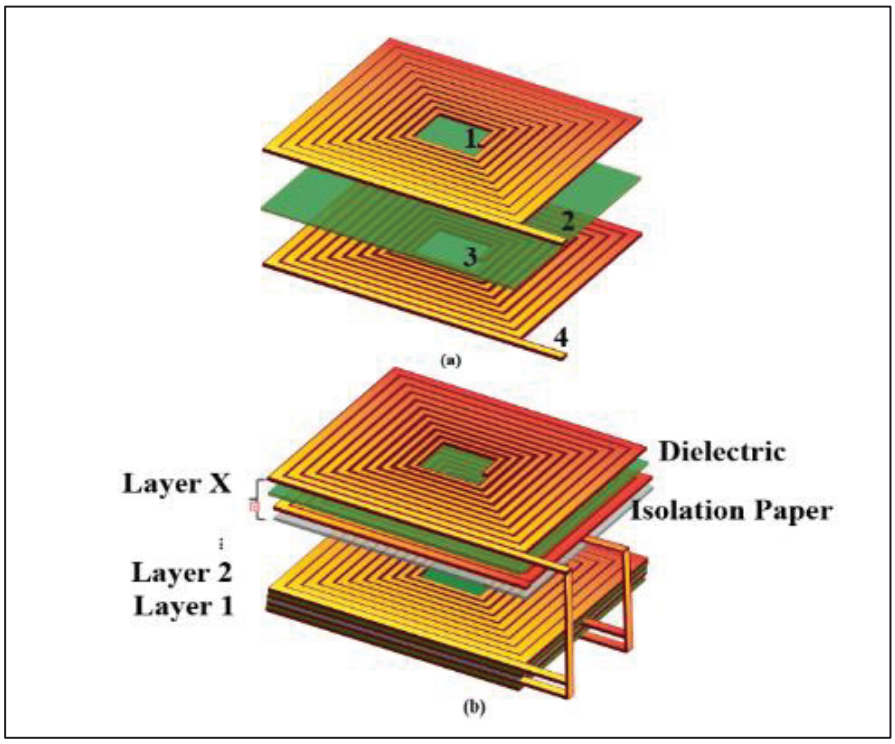

Figure 2.1 Structure of the proposed self-compensated PCB coils.
(a) Double-layer PCB coil, (b) Multilayer PCB coil

decreases. This novel configuration reduces AC resistance by limiting wire exposure to the high magnetic field region close to the coil center.

2.2.2 Equivalent Circuit

The proposed coil connects six double-layer coils in parallel, and each layer is identical with Y turns. Each turn can be considered as a one-turn inductor, indicated as L(X,Y), in which X and Y are the serial number of the layer and conductor, respectively. The capacitance generated between top and bottom conductors is represented by C(X,Y), and the capacitance produced by the adjacent double-layer coils is indicated as C_insolated (X,Y). These two capacitances are determined by the conductor subtending area, thickness and conductivity of the dielectric layer. The vertical cross section and equivalent circuit of the proposed multilayer PCB coil,

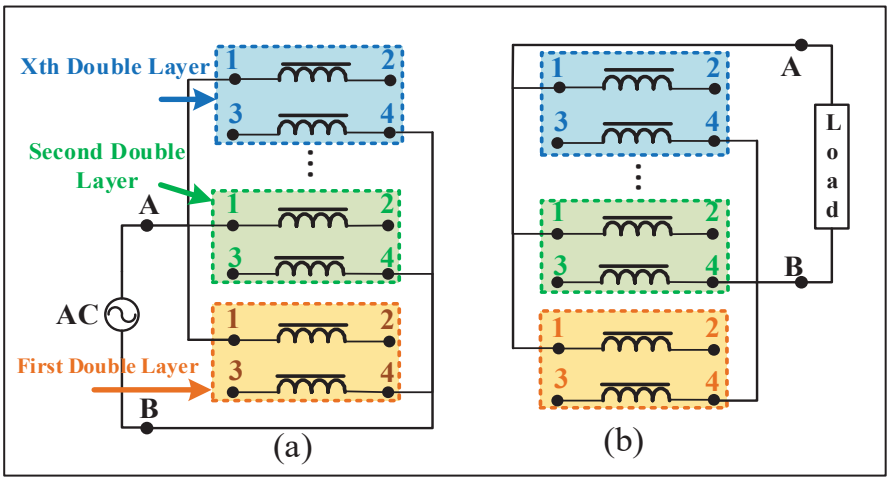

Figure 2.2 Connections of the transmitter and receiver coils. (a) Transmitter coils, (b) Receiver coils

where each layer is subdivided into X segments and each segment is denoted by an inductor L are illustrated in Figure 2.3 (a) and (b), respectively. Due to the equal length of L(1,n) and L(2,n), these conductors have equal inductance, but those between segment pairs differ, which means:

$$L(1,n)=L(2,n)=\ldots=L(X,n)\ ,\ \ n=1,2,\ \ldots\ ,\ Y \tag{2.1}$$

The symmetrical coil layout and the same board material used make capacitance identical as follows:

$$C(1,n)=\ C(2,n)=\ \ldots\ =C(X-1,n)\ ,\ \ n=1,2,\ \ldots\ ,\ Y+1 \tag{2.2}$$

From Figure 2.3 (b), one can see that the equivalent circuit of a double-layer coil consists of Y loops, and each loop has two inductances and two capacitances. The voltage of L(1,Y) and L(2,Y) can be expressed as:

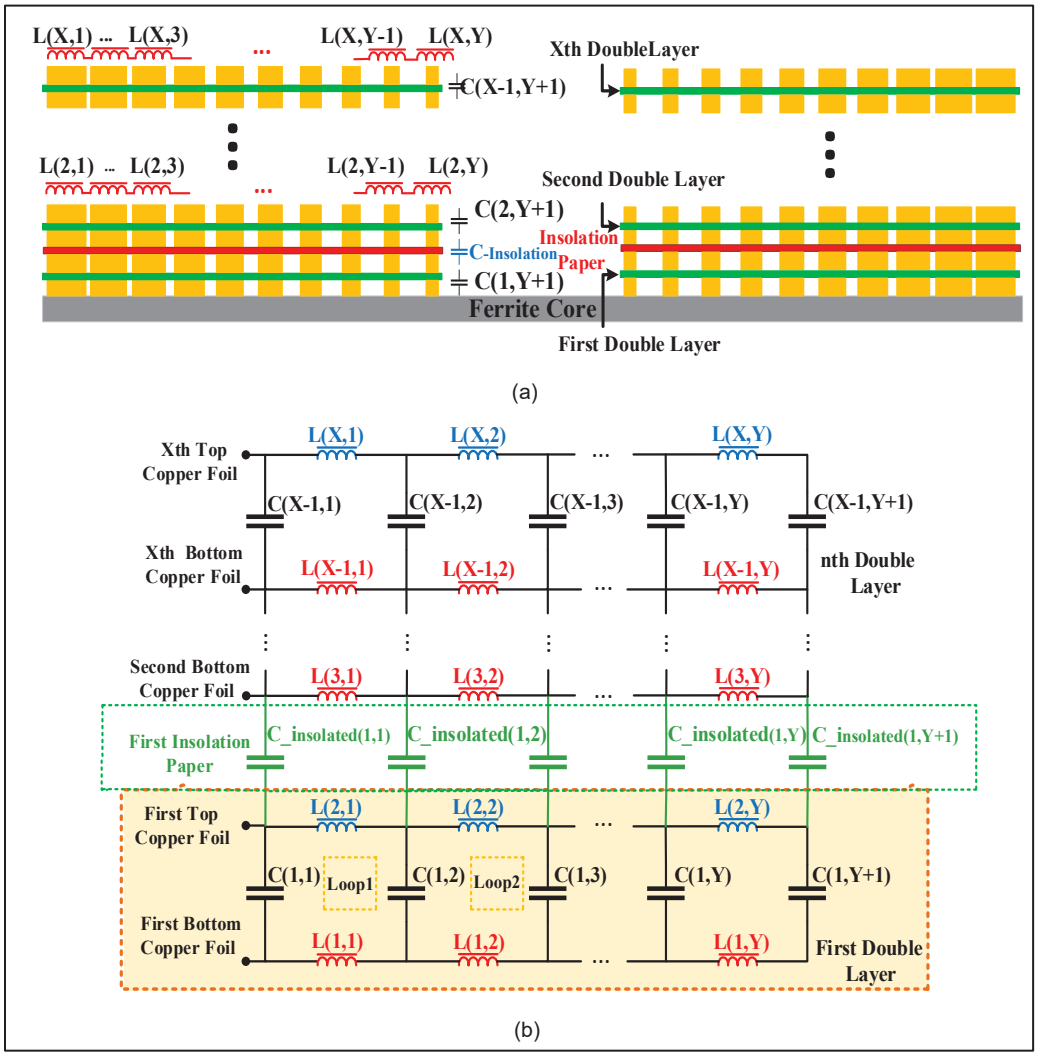

Figure 2.3. (a) Vertical cross section of PCB coils with track-width-ratio and track-gap-ratio. (b) Equivalent circuit of multilayer PCB coils

$$V_{L(1,Y)} = L_{(1,Y)} \frac{di}{dt}, \qquad V_{L(2,Y)} = L_{(2,Y)} \frac{di}{dt} \tag{2.3}$$

The identical feature and consistent coil materials ensure unique inductance across each nth turn at different layers. Consequently, the voltages $V_{L(1,Y)}$ and $V_{L(2,Y)}$ across the inductors remain identical (Ho & Pong, 2019), which can be written as:

$$V_{L(1,Y)} = L_{(1,Y)} \frac{di}{dt} = L_{(2,Y)} \frac{di}{dt} = V_{L(2,Y)} \tag{2.4}$$

In the loop of a double-layer coil, the voltage equation is given by:

$$V_{C(1,1)} + \sum_{a=1}^{Y} V_{L(2,a)} = V_{C(1,Y+1)} + \sum_{a=1}^{Y} V_{L(1,a)} \tag{2.5}$$

Where, $V_{C(1,Y)}$ is the voltage of the capacitance between upper and lower conductors. Thus, considering the equality of the voltages across the two inductors, the voltages across the capacitors become equal as well. However, it is important to note that the actual sizes of the capacitors vary. Therefore:

$$V_{C(1,1)} = V_{C(1,Y+1)} \tag{2.6}$$

For other layers we have:

$$V_{C(X-1,1)} + \sum_{a=1}^{Y} V_{L(X,a)} = V_{C(X-1,Y+1)} + \sum_{a=1}^{Y} V_{L(X-1,a)} \tag{2.7}$$

$$V_{C(X-1,1)} = V_{C(X-1,Y+1)} \tag{2.8}$$

Equation (2.8) proves that all the capacitors between the top and bottom layers have the same voltage. As illustrated in Figure 2.4 (a) to calculate the equivalent capacitance in a two-layer coil, note the Kirchhoff's Current Law (KCL). With I_{in1} and I_{in2} as the input currents and I_{out} as the output current, the relationship is given by:

$$I_{in1} = C_{(1,Y)} \frac{dv_{C(1,Y)}}{dt} + C_{(1,Y+1)} \frac{dv_{C(1,Y+1)}}{dt} \tag{2.9}$$

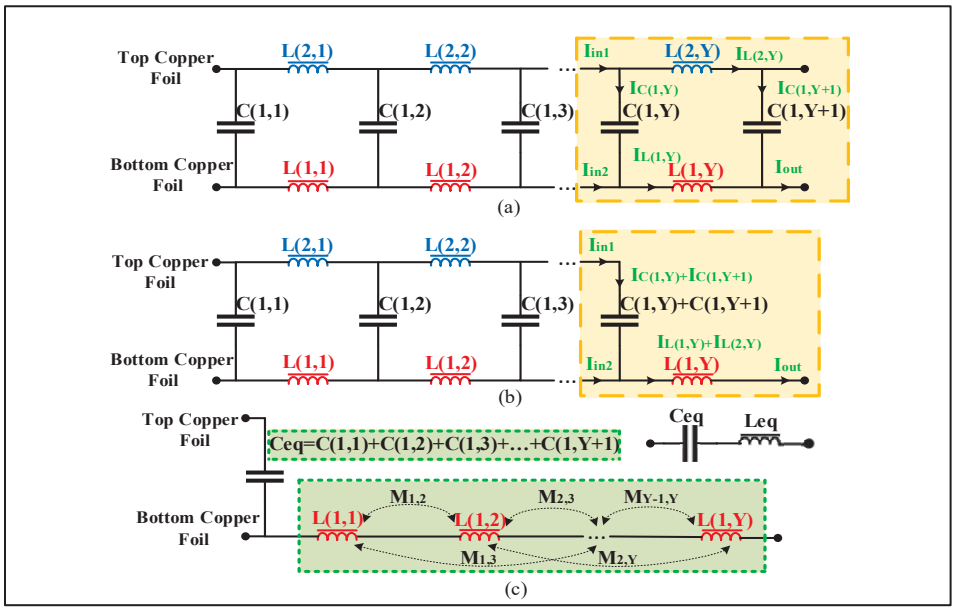

Figure 2.4. Equivalent circuit of a double-layer coil. (a) Circuit with distributed inductance and capacitance. (b) Circuit shows equivalent capacitance and inductance of the end loop. (c) Final equivalent circuit

Bases on (2.8), the equation in (2.9) can be rewritten as follows:

$$I_{in1} = (C_{(1,Y)} + C_{(1,Y+1)}) \frac{dv_{C(1,Y)}}{dt} = (C_{(1,Y)} + C_{(1,Y+1)}) \frac{dv_{C(1,Y+1)}}{dt} \tag{2.10}$$

Therefore, the equivalent capacitance equals the sum of the capacitors of each section. The equivalent inductance for each layer could be determined using the voltage across L(1,Y), which includes a self-induced voltage and an induced voltage from L(2,Y), as expressed below:

$$V_{L(1,Y)} = L_{(1,Y)} \frac{dI_{L(1,Y)}}{dt} + M_{(1,Y)(2,Y)} \frac{dI_{L(2,Y)}}{dt} \tag{2.11}$$

Where, M is the mutual inductance between L(1,Y) and L(2,Y) that is given by:

$$M_{(1,Y)(2,Y)} = K_{(1,Y)(2,Y)} \sqrt{L_{(1,Y)} L_{(2,Y)}} \tag{2.12}$$

Given the thin insulating layer and consistent coil geometry, a unique magnetic field permeates both copper foils on top and bottom of the dielectric layer. Consequently, the coupling coefficient K is treated as 1, therefore

$$M_{(1,Y)(2,Y)} = L_{(1,Y)} = L_{(2,Y)} \tag{2.13}$$

Equation (2.11) can be rewritten as follows:

$$V_{L(1,Y)} = L_{(1,Y)} \frac{d(I_{L(1,Y)} + I_{L(2,Y)})}{dt} = L_{(1,Y)} \frac{dI_{out}}{dt} \tag{2.14}$$

Based on the aforementioned analysis, the equivalent circuit in the nth loop is comprised of an inductance and a capacitor, as illustrated in Figure 2.4 (b). The equivalent circuit could be simplified with a concentred capacitance and a concentrated inductance that are connected in series, as shown in Figure 2.4 (c).

2.2.3 Inductance Modeling

The inductance of the multi-turn planar spiral coil is determined by the sum of self-inductance for each turn and both positive and negative mutual inductances between turns, as indicated by:

$$L_{Layer} = L_S + M_{Positive} + M_{Nehative} \tag{2.15}$$

Self-inductance could be calculated using the following equation:

$$L_S = \frac{\mu_o}{2Pi} + \sum_{\alpha=1}^{4n} l_n \left[\ln\left(\frac{2l_n}{w_n + t_n} \right) + 0.5 + \frac{(w_n + t_n)}{3l_n} \right] \tag{2.16}$$

Where, μ_o, t_n, w_n represent the permeability of free space, thickness and width of the nth coil turn, respectively. l_n is the length of each turn. The calculation of positive and negative mutual inductance is given as follows:

$$M_{Positive} = 4 \sum_{i=1}^{N} \sum_{j=1}^{N-k} M(i, i+j) \tag{2.17}$$

$$M_{Negative} = 2 \sum_{i=1}^{N} \sum_{j=1}^{N} M(i, j) \tag{2.18}$$

Where, positive mutual inductance signifies the presence of identical current directions in each coil section, whereas negative mutual inductance indicates opposing current directions in their respective coils.

2.2.4 Capacitance Modeling

In the proposed structure, the electric field is composed of two types: electric field oriented vertically between two layers within the dielectric, and undesirable fringing electric fields between adjacent traces. As illustrated in Figure 2.5(a) there is a very thin dielectric layer between two copper foils. The capacitance between these layers is computed similarly to that of a planar capacitor. Thus, each layer's total area equals the sum of the individual areas of every turn. Consequently, the layer-to-layer capacitance is calculated as follows:

$$A_{Total} = A_1 + A_2 + \ldots + A_N' \tag{2.19}$$

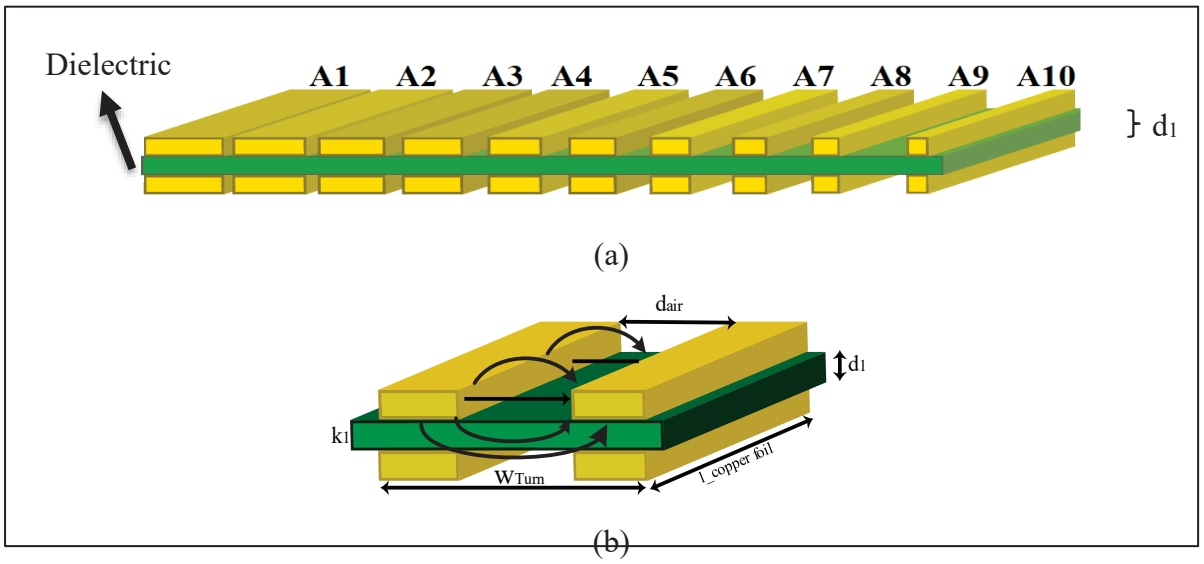

Figure 2.5 Capacitance calculation of proposed coil structure. (a) Layer to layer, (b) Parasitic capacitance

$$C_{Layer-Layer} = \frac{1}{(d/k_1 \varepsilon_o A_{Total})} \tag{2.20}$$

Where, d, k_1, and ε_o represent the dielectric thickness, relative permittivity of the dielectric, and permittivity of free space, respectively. In addition to the capacitance generated in (2.20), the fringing electric field between turns, also contributes to the creation of parasitic capacitance, particularly when the distance between two turns is minimal. As shown in Figure 2.5 (b), the fringing electric field implies to two adjacent turns with the air and dielectric. C_{air} and $C_{dielectric}$ correspond to the capacitance involving air and dielectric, respectively, which can be calculated based on conformal mapping and the assumption of the magnetic wall (Vendik, Zubko & Nikol'Skii, 1999) as follows:

$$\begin{cases} C_{air} = \varepsilon_o l_{copper-foil} F(k_o) \\ k_o = d_{air} / w_{Turn} \end{cases} \tag{2.21}$$

$$\begin{cases} C_{Dielectric} = 0.5\varepsilon_o l_{copper-foil} (k_1 - k_o) F(k_1) \\ k_1 = \tanh(\frac{\pi d_{air}}{4d_1}) / \tanh(\frac{\pi w_{Turn}}{4d_1}) \end{cases} \tag{2.22}$$

Where,

$$F(k_i) = \begin{cases} \pi^{-1} \ln\left[2\frac{1+(1-k_i^2)^{0.25}}{1-(1-k_i^2)^{0.25}} \right] & \text{for } k_i \le 0.5 \\ \pi\left[\ln(2\frac{1+\sqrt{k_i}}{1-\sqrt{k_i}}) \right]^{-1} & \text{for } k_i \ge 0.5 \end{cases} \tag{2.23}$$

Consequently, the parasitic capacitance between two turns is calculated as given:

$$C_{Parasitic-T-T} = C_{air} + C_{Dielectric} \tag{2.24}$$

The overall capacitance of a multi-layer PCB coil, with insolated paper between each two-layer, can be described as:

$$C_{Total} = nC_{Layer-layer} + (n-1)C_{Insolated} + C_{air} + C_{Dielectric} \tag{2.25}$$

Where, n is the number of layers. Therefore, based on the above equation, increasing the number of layers allows for the production of a larger capacitance, consequently resulting in lower resistance and a resonant frequency. The self-resonant frequency is determined by the

desirable compensation capacitance between coil layers while the undesirable parasitic capacitance will slightly decrease the self-resonant frequency.

2.2.5 Resistance Modeling

The total power loss in the proposed self-resonant coil originates from two main components: copper loss and dielectric loss. The copper loss can be divided into two categories: low-frequency loss caused by the DC resistance of the copper traces, and high-frequency loss, which results from eddy current effects within the conductors. These high-frequency losses include both skin effect and proximity effect, which become significant as the operating frequency increases. The following equation represents the total loss:

$$R_{Total} = R_{DC} + R_{Skin} + R_{\Pr oximity} + R_{Dielectric} \tag{2.26}$$

For a simple spiral coil, the low frequency resistance is:

$$R_{DC\_Spiral\ coil} = \frac{\rho_{copper}\int \vec{E}.\vec{dl}}{\vec{E}.\vec{dS}} = \sum_{n=1}^{N} \frac{\rho_{copper}\pi n(d_i + w_n + n.s)}{w_n.t_n} \tag{2.27}$$

When the simple spiral coil conducts I_o, the loss can be calculated as follows:

$$P_{DC\_Spiral\ \text{coil}} = \sum_{n=1}^{N} \frac{\rho_{copper}\pi n(d_i + w_n + n.s)}{w_n.t_n}.I_o^2 \tag{2.28}$$

In a double layer self-resonant coil, the current distribution differs from the simple spiral coil. At the input, all current flows through one spiral conductor, with no current in the opposite one. As the current moves along the coil, it transitions from the top to the bottom conductor in a linear manner. The total current is I_o, and the current at any point l_1 from the first terminal is given by the following relation.

$$I_{l1} = l/l_o \, I_o \tag{2.29}$$

The total current on both sides sums to I_o. Consequently, the current at the same position on the opposite side is given by:

$$I_{l2} = I_o(l_o - l)/l_o \tag{2.30}$$

After substituting $I_{l1}+I_{l2}=I_0$ into equation (2.28) and simplifying, it is found that for the same current, the loss in the self-resonant coil is 2/3 of the loss in a simple spiral coil. Therefore,

$$R_{DC\_Self\ \mathrm{Re}sonant} = \frac{2}{3} R_{DC\_Spiral\ \mathrm{coil}} \tag{2.31}$$

In addition to the DC resistance, the time-varying magnetic field induces eddy current losses in the copper foil, which include the skin effect and proximity effect. Skin effect is the phenomenon where higher-frequency currents tend to concentrate near the surface of a conductor, limiting their penetration into the interior. This effect can be computed using the following formula:

$$R_{Skin} = \sum_{n=1}^{N} \frac{l_n}{\tau \sigma w_n \alpha^{0.5} \beta} \tag{2.32}$$

Where, σ and p_n stand for the coil's conductivity and pitch of coil, respectively. In (33), the parameters α, β, and τ are expressed as:

$$\alpha = 1/\pi\sigma\mu_o f \quad , \quad \beta = (1 - e^{-\frac{t_n}{p_n}}) \quad , \quad \tau = (1 + \frac{t_n}{w_n}) \tag{2.33}$$

Proximity effect refers to the phenomenon where the distribution of current in a conductor is affected by the presence of neighboring conductors, leading to non-uniform current density and increased resistance. The calculation is as follows:

$$R_{\text{Pr}oximity} = \sum_{n=1}^{N} \frac{4\pi l_n \Phi_n H_n^2}{\sigma} \tag{2.34}$$

Where,

$$\Phi_n = -0.998 + 0.112\frac{w_n}{t_n} - 0.689\frac{t_n}{\delta} + 0.543\frac{w_n}{\sigma} + 0.002(\frac{w_n}{t_n})^2 \tag{2.35}$$

H_n indicates the magnetic field that is perpendicular to the turn's surface when exposed to a current of 1A. The calculation of dielectric loss relies on the dielectric material's loss tangent, expressed as D_k, which given by:

$$R_C = \frac{D_K}{2\pi f C_S} \tag{2.36}$$

2.2.6 Power Quality Modeling

The inductance, resistance, and capacitance underscore the influence of variations in the number of turns, width, gap, and thickness of the traces in the multi-layer planar coil. Thus, the quality factor of the whole system can be derived from (2.37):

$$Q = \frac{wL_{eq}}{R_{Total}} \tag{2.37}$$

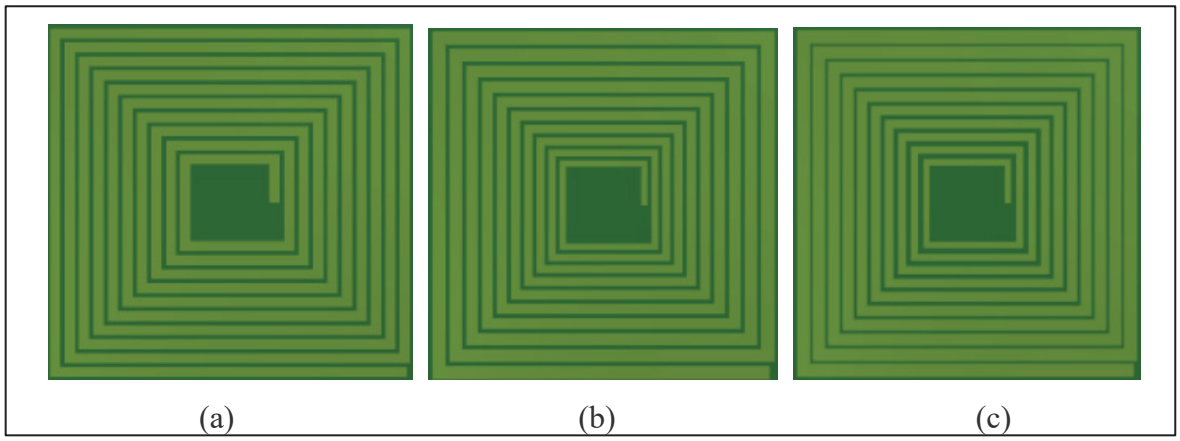

Figure 2.6 Coil topology. (a) Traditional coil, (b) TWR coil, (c) Proposed TWR-TGR coil

Where, R_{Total} is the equivalent resistance which can be calculated according to (2.26) (Awuah, Danuor, Moon & Jung, 2023; Li & Daniel, 2018). Furthermore, the generalized formula for multilayer coils with n double-layer coils is provided for accurate computation of system performance.

$$Q_n = \frac{n}{R_{Total}} \sqrt{\frac{L}{nC_{Layer-Layer} + (n-1)C_{insolated}}} \tag{2.38}$$

2.3 Design and Optimization of the PCB Coils

The principal performance of RWPT systems, such as the quality factor, resonant frequency and transfer efficiency, are determined by the AC resistance, inductance and intra-winding capacitance of the coils. Since inductance is proportional to the square of number of turns and intra-winding capacitance is proportional to number of turns. Increase the number of turns is an effective approach to reduce resonant frequency. However, increase the number of turns will significantly increase the coil size or increase AC resistance if the size is fixed. The gap between adjacent turns also changes the intra-winding capacitance. Therefore, it is necessary to optimize the fundamental parameters, which include conductor width, gap between adjacent turns, and number of turns to achieve an optimal overall performance. This section presents

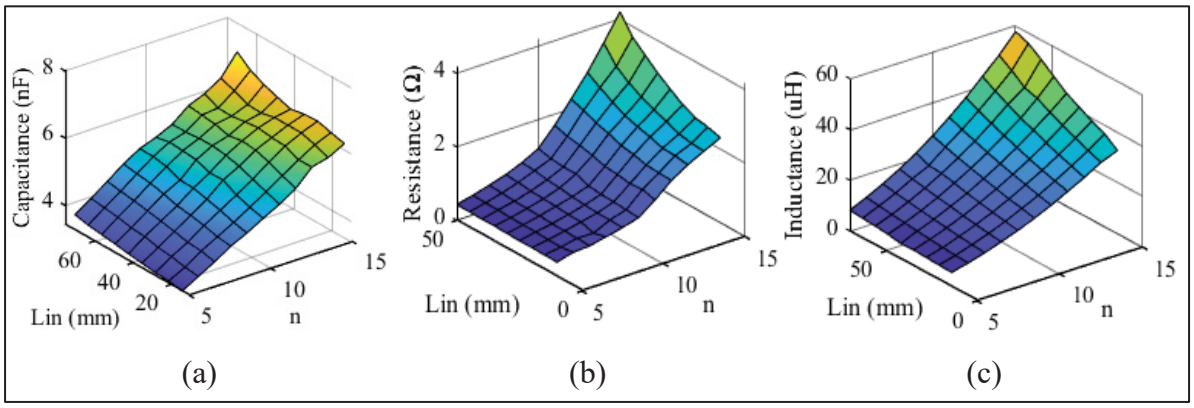

Figure 2.7 Effect of inner length and number of turns on the performance of a double-layer self-compensated coil: (a) Intra-winding capacitance, (b) Resistance, (c) Inductance

the optimization of self-compensated PCB coils, to maximize inductance and intra-winding capacitance, and minimize resistance. The optimization includes two steps. First, a traditional double-layer PCB coil is optimized, in which all coil turns have the same width and the gap between adjacent turns is also the same. Second, TWR and TGR are applied to the optimized coil, and a comparative study is conducted to select the best coil topology. Figure 2.6 shows the topologies of these three coils.

2.3.1 Optimization of a Traditional Double-Layer Coil

With consideration of reducing skin effect and easy fabrication, a constant coil thickness of 72 μm is chosen. The dielectric material is FR4. Although minimizing dielectric thickness is an effective method to increase capacitance, it is restricted by fabrication and a thickness of 0.25 mm is selected in this optimization. Design variables include the number of turns (n), coil width (W), and gap between wires (g), while coil's size (l_{out}), inner Length (l_{in}), dielectric thickness, and wire thickness are constant. Figure 2.7 (a) to (c) illustrates the effect of inner length and the number of turns on intra-winding capacitance, inductance, and resistance. Fig.7(a) shows that intra-winding capacitance increases almost linearly with the number of turns, as more turns result in a larger frontal area. Similarly, increasing the inner length also enhances intra-winding capacitance. However, this improvement increases proximity resistance and losses by reducing the spacing between turns in a fixed coil size as shown in

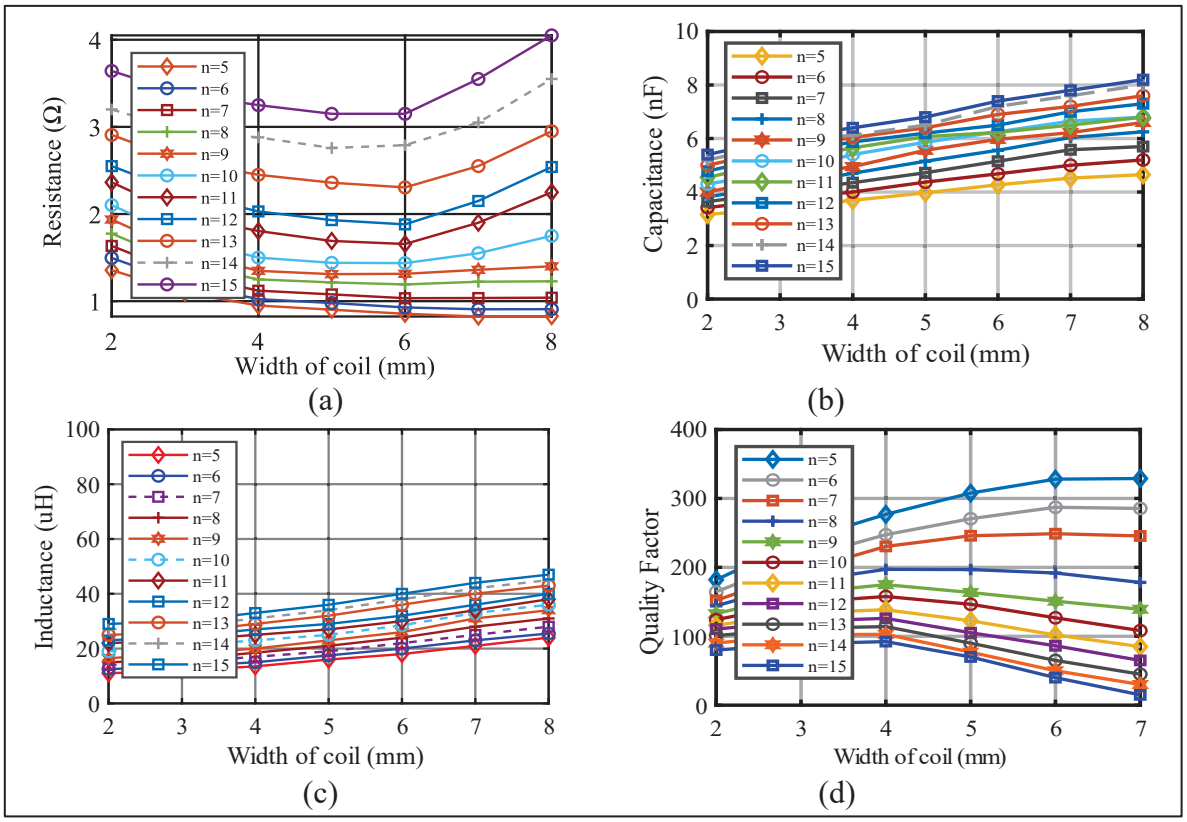

Figure 2.8. Effect of coil width and number of turns on (a) Resistance, (b) Inductance, (c) Capacitance, and (d) Quality-Factor

Figure 2.7(b). A similar trend is observed for inductance in Figure 2.7 (c), which rises with both the number of turns and the inner length. Consequently, increasing the number of turns and inner radius lowers the resonant frequency, bringing it closer to the target of operating below 150 kHz. However, this also leads to higher resistance and losses. Achieving an optimal balance between these factors is critical for designing a coil that enhances both capacitance and inductance, while minimizing adverse effects on performance. To achieve this, various designs were analyzed in ANSYS Maxwell to identify the optimal values. The influence of coil width and the number of turns on capacitance, resistance, and inductance are illustrated in Figure 2.8(a)–(c). From Figure 2.8 (a), it can be observed that the resistance initially decreases and then increases with the increase of coil width. This is because a wider width initially increases the cross-sectional area and reduces resistance accordingly. However, a larger coil

width will exacerbate proximity effect, leading to increased resistance in fixed coil size. As shown in Figure 2.8(b) and 2.8(c), both inductance and capacitance increase with coil width. Capacitance rises because it is proportional to the coil's facing area; as the width increases while maintaining the same overall coil size, the turn-to-turn gap narrows, enhancing parasitic capacitance. Likewise, inductance increases with wider coils due to the higher mutual inductance between turns, which contributes to the overall inductance. According to Fig. 8(a), the resistance is minimized at a coil width of 6 mm, making it the optimal choice for reducing losses. With this width fixed, the corresponding inductance (L) and capacitance (C) values are evaluated to determine the resonant frequency. Among all possible L and C values at 6 mm, the smallest number of turns (n) that ensures a resonant frequency below 150 kHz is selected. Choosing the minimum n is essential to limit losses, as a higher turn count increases resistance. Based on this trade-off, n = 10 is chosen, achieving a resonant frequency below 150 kHz while maintaining resistance below 1.5Ω. Figure 2.8 (d) indicates the quality factor against the width for various values of n at their self- resonant frequencies. As illustrated in the figure, the minimum power quality is observed at n=15, while n=5 exhibits the highest power quality. This is attributed to the fact that at n=5, the generated inductance and intra-winding capacitance are minimal, resulting in a high resonant frequency. Due to the direct correlation between frequency and quality factor, the resulting quality factor is higher. In contrast, as n increases, not only the resonant frequency decreases, but also the resistance grows, leading to a reduction in the quality factor. Additionally, increasing the width for any number of turns initially enhances the quality factor, but beyond a certain value of W, it declines due to the increasing parasitic capacitance and produced resistance. Therefore, for a double layer traditional coil, the optimal configuration is achieved with 10 turns, a 6 mm width, and turn to turn gap 2.5mm with the quality factor of 42.45.

2.3.2 TWR and TWR-TGR coils

To enhance the quality factor, it is essential to minimize coil resistance losses, specifically skin-effect resistance (R_{sk}) and proximity-effect resistance (R_{pr}). Inner turns, subjected to stronger magnetic fields, experience higher R_{pr}. Narrowing the trace width of these inner turns can reduce R_{pr} by decreasing the exposed area to the magnetic field, thus lowering eddy

currents; however, this also increases R_{sk}. Our novel approach improves the quality factor by integrating narrower trace widths with increased spacing between turns, effectively reducing overall resistance. Based on the optimized double-layer coil in section III-A, TWR and TGR are applied as shown in Figure 2.6. Figure 2.6 (b) shows the coil with TWR, in which the conductor width increases gradually from the inside to the outside, while the gap between adjacent conductors is kept constant. Figure 2.6 (c) shows the proposed TWR-TGR coil, in which the conductor width gradually increases from the inside to the outside, while the gap between adjacent conductors gradually decreases. In the traditional coil shown in Figure 2.6(a), coil width is 6mm, inter-turn gap is 2.5mm, and inner length is 50mm. In the TWR coil, the same inter-turn gap of 2.5 mm is maintained. The outermost wire has an initial value of 6 mm, and the width of each subsequent inner wire decreases exponentially based on a scaling factor (α_{TWR}) for each turn. This relationship is described by the following equation:

$$W_n = a_{TWR}^{n-1} W \tag{2.39}$$

Where n represents the turn number, starting from the outermost turn. The quality factor (Q) of the coils is calculated as a function of the scaling factor (α_{TWR}), as shown in Figure 2.9 (a),

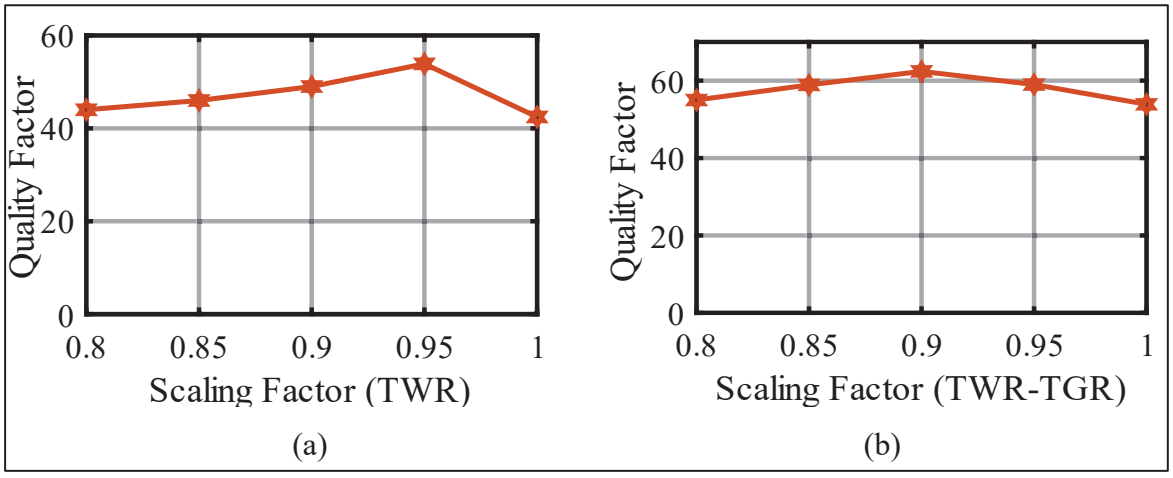

Figure 2.9 Simulated *Q*-factor of the proposed double layer coil for various scaling Factors. (a) TWR coil, (b) TWR-TGR coil

at the resonance frequency. The optimal scaling factor is determined to be α_{TWR}=0.95, resulting in a Q-factor of 53.89. By contrast, for the conventional coil, where the scaling factor remains α_{TWR} =1, the Q-factor is 42.45. In the TWR-TGR coil shown in Figure 2.6(c), the coil width is the same as TWR coil, but the inter-turn gap varies, gradually decreasing from the center toward the outer side. For the outermost turns, an inter-turn gap of 2.5 mm is applied. Moving toward the center, the gap increases following a specific relationship described by the equation:

$$G = a_{TWR-TGR}^{n-1} G_n \tag{2.40}$$

Where, n represents the turn number, starting from the outermost turn. The quality factor (Q) for the coils is evaluated as a function of the scaling factor ($\alpha_{TWR\text{-}TGR}$) as illustrated in Figure 2.9 (b), at the resonance frequency. The optimum scaling factor is found to be α=0.9, yielding a Q-factor of 62.4. In comparison, for the TWR coil with a constant scaling factor of $\alpha_{TWR\text{-}TGR}$=1, the Q-factor is measured at 53.89. The optimal design process is presented in Figure 2.10.

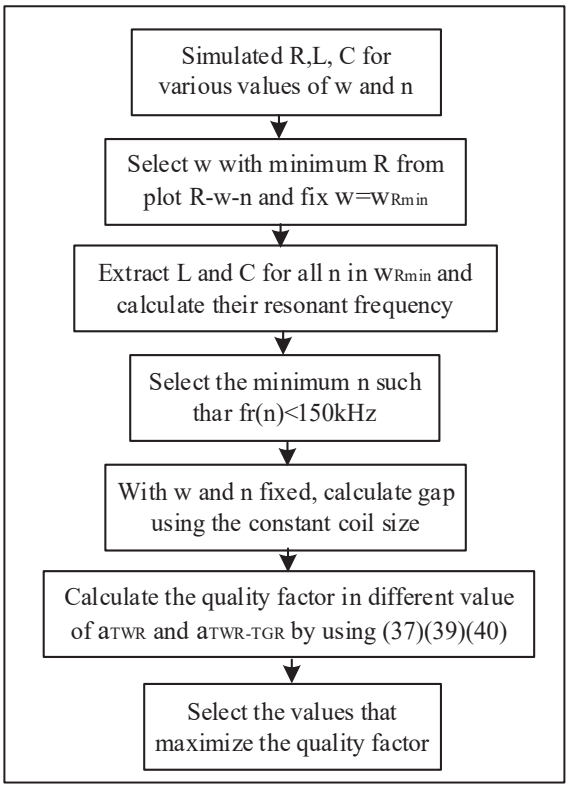

Figure 2.10. Optimal design process

The current density for the three coils is calculated using ANSYS Maxwell, as depicted in Figure 2.11. It can be observed that the traditional coil exhibits high current density concentrations and hot spots, indicating inefficient current distribution and potential overheating, which can increase AC resistance and reduce efficiency. The TWR coil in Figure 2.11 (b) improves performance by distributing current more uniformly. The proposed coil in Figure 2.11 (c) is the most efficient one, achieving an even current distribution and minimizing high-density areas, thus reducing AC resistance and the associated losses. This TWR-TGR strategy effectively suppresses skin effect and proximity effect and enables the proposed SRWPT system to achieve a high efficiency and high-quality factor. The inductance, intra-winding capacitance and AC resistance of these three coils are simulated using ANSYS Maxwell, and resonant frequency and quality factor are calculated. The results are given in TABLE 2.1. One can see that the proposed TWR-TGR coil has the lowest resistance.

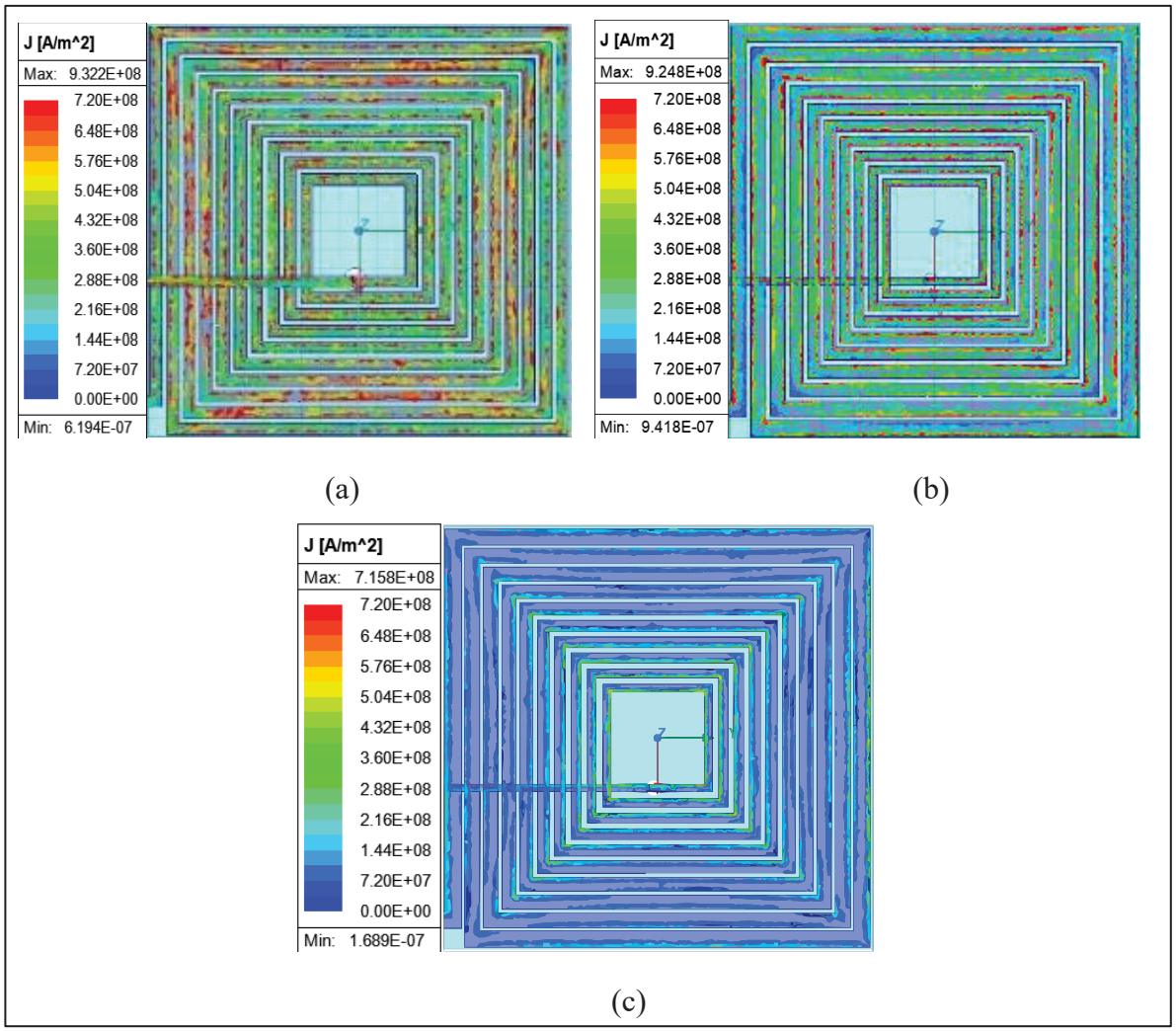

Figure 2.11 Current density. (a) Traditional coil, (b) TWR coil, (c) TWR-TGR coil

The quality factor of the proposed TWR-TGR coil is 47% larger than that of the traditional coil, and 15.98% larger than that of the TWR coil. When connecting 6 double-layer coils in parallel, namely multi-layer coil in TABLE 2.1, the resistance could be further reduced and capacitance is increased significantly, which increases quality factor and reduces resonant frequency. The comparison between the proposed TWR-TGR coil and representative coils reported in existing literatures are given in Table 2.2. It can be seen that the proposed coil has the highest quality factor and efficiency.

Table 2.1 Simulation Results of self-resonant compensated coils

Parameter	Double layer Coil			Multi-Layer Coil		
	Traditional	TWR	TWR+TGR	Traditional	TWR	TWR+TGR
L (uH)	25.6	23.2	24.97	26.6	23.84	25.76
C (nF)	6.7	6.03	6.12	48.8	43.61	45.5
R (mΩ)	1456	1151	1023.4	275	213	178

Table 2.2 Comparison of the multi-layer self compensated coils

Ref	CÔTE, Nathis, et al (2022)	WANG, Qingsong, et al (2020)	LEE, Young-Dal; KIM, Keon-Woo; MOON, Gun-Woo (2021)	JIANG, Chaoqiang, et al (2020)	Proposed
Structure	Six-4 Layer	8 Double Layer	4 Double Layer	24 Layer	6 Double Layer
Coil size	230mm*220mm* 9.6 mm	100mm*100mm* 6.4 mm	270mm*270mm* 9.6 mm	60mm*30 mm	214mm*200mm* 3.2 mm
Resonant frequency	120kHz	140kHz	80kHz	176kHz	147kHz
Generated Capacitance	20nF	25nF	12.8, 18.4, 21.1, 18.5 nF	10.8nF	45.6nF
Output power	67W	60W	360W	20W	210W
Efficiency	65%	75%	82%	83%	94.7%
Quality Factor	N/M	N/M	23	35	123

2.3.3 Insulation Evaluation

Insulation is crucial in multilayer, multi-turn coil designs to prevent electrical breakdown between adjacent turns and layers. Assessing insulation effectiveness involves evaluating the electric field distribution. At 147 kHz and with a 15 A peak-to-peak current in the self-compensated coil pad, each inductor coil experiences a maximum potential difference of 0.35

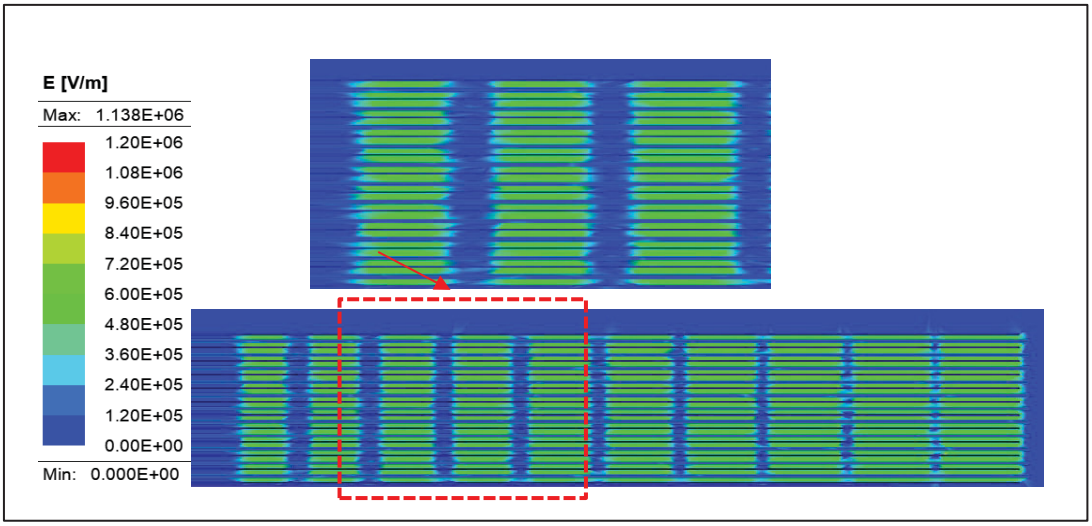

Figure 2.12 Insulation evaluation by analyzing the distribution of electric fields

Table 2.3 Design Parameters

Parameter	**Values**
Number of turns	10
Inner length	50 mm
Outer length	214 mm
Thickness of trace	0.072 mm
Scaling factor of TWR	0.95
Scaling factor of TWR-TGR	0.9
Thickness of dielectric layer	0.25 mm
Thickness of insulation paper	0.2 mm
Number of PCB	6

kV. From Figure 2.12, FEA results show the electric field distribution remains well below FR4's dielectric strength (20 kV/mm for 0.25 mm thickness). This confirms the coils can handle higher currents, with the selected dielectrics providing robust insulation for the self-compensated WPT system.

2.4 Experimental Verification

Two TWR-TGR coils with parameters given in Table 2.3 are fabricated, one as the transmitter and the other as the receiver, and experimental tests are conducted to verify the effectiveness of the proposed design. Figure 2.13 shows the experimental setup, in which the input power is provided by a 6554A DC power supply. The high-frequency AC input of transmitter is

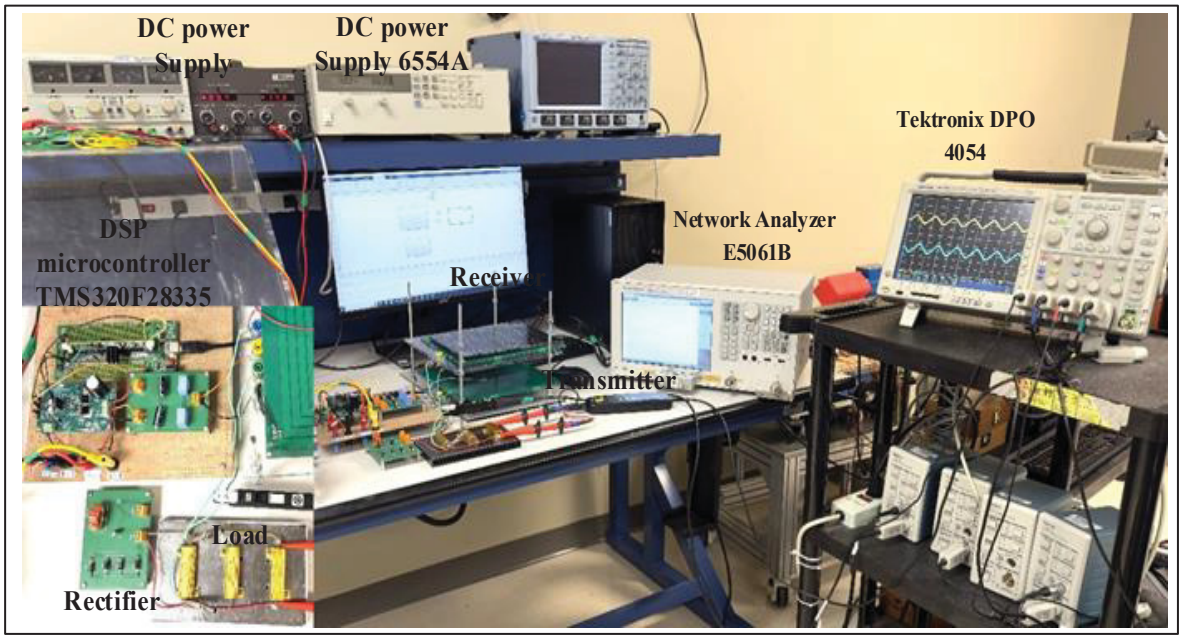

Figure 2.13 Experimental setup of the proposed SR WPT

Table 2.4 Comparison results of the calculation, simulation, and measurement

Parameter	Double layer Coil			Multi-Layer Coil		
	calculation	Simulation	Measured	calculation	Simulation	Measured
L (uH)	25.6	24.9	25.12	25.13	25.76	25.6
C (nF)	6.24	6.12	6.6	46.2	45.5	45.37
R (mΩ)	1104.1	1023	1151	175.12	178	193
F (kHz)	398.3	407.3	391	147.7	147.08	147.7
Q	58	62.4	53.59	133.2	133.6	123.07

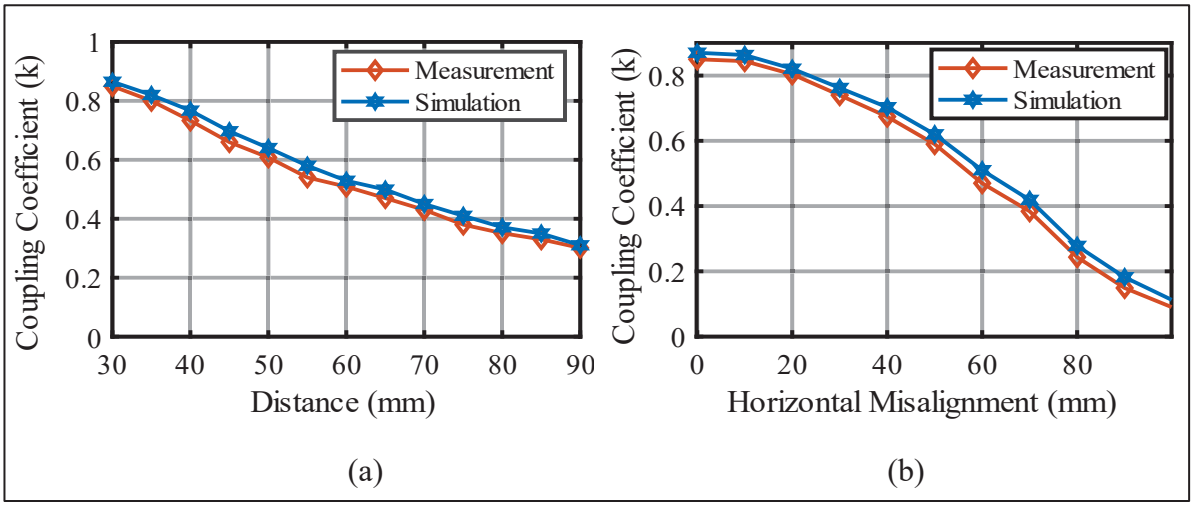

Figure 2.14 Coupling coefficient between the transmitter and receiver. (a) Without misalignment, (b) with horizontal misalignment

generated by an H-bridge inverter that employs MOSFETs (STL33N60DM2). The generation and regulation of PWM signals, featuring a 50 ns dead time and a 50% duty cycle, are carried out by the DSP microcontroller (TMS320F28335). The diode rectifier connected to the receiver is constructed using Schottky diodes (MBR10200FH-BP), and a 200uF capacitor is used as the output filter. To determine the resonant frequency of the coils, a network analyzer (E5061B ENA series Network Analyzer) is utilized. Table 2.4 presents a comparison of the calculated, simulated, and measured results for proposed double-layer and multi-layer coils, which shows a close agreement. Figure 2.14 shows the coupling coefficient between the transmitter and receiver with and without horizontal misalignment. The transmission distance is 30mm when misalignment is applied. The figures reveal that the coupling coefficient decreases with increasing distance. Therefore, the importance of improving the quality factor becomes crucial for enhancing efficiency and power transfer. Again, a good agreement between the simulation and experimental results can be observed. The impedance and phase of the proposed TWR-TGR coil across a frequency range from 100 kHz to 250 kHz are measured using a network analyzer, as shown in Figure 2.15 (a) and (b), respectively. The resonance frequency is identified at the minimum impedance, where the phase angle becomes zero. It can be observed that the resonant frequency of the coil is 147.5kHz.

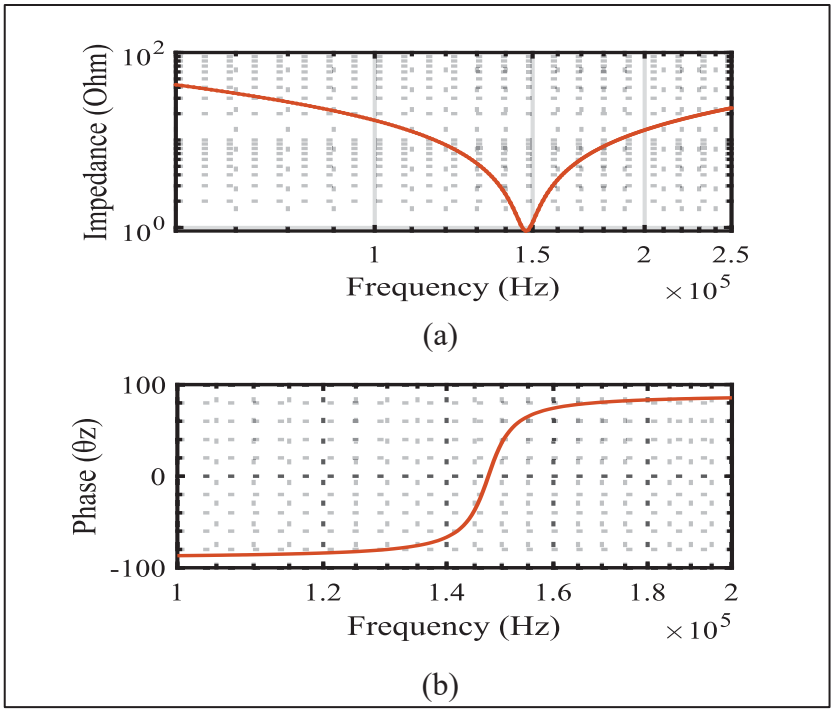

Figure 2.15. Frequency characteristics of the proposed TWR-TGR coil. (a) Impedance, (b) Phase angle

By keeping the transmission distance at 30mm, the influence of load resistance on the output power and coil-to-coil efficiency is investigated, as depicted in Figure 2.16. The results show that the proposed RWPT system achieves a maximum efficiency of 94.7% when the load is 25 Ω and a maximum power of 174.6W when the load is 55 Ω. The power and efficiency when the transmission distance is 30mm, 50mm and 70mm are tested, as given in Figure 2.17. One can see that both power and efficiency reach its maximum at the resonant frequency. Since the coupling coefficient reduces with the increasing of transmission distance, the efficiency at 30mm is larger than the efficiency at 50mm and 70mm.

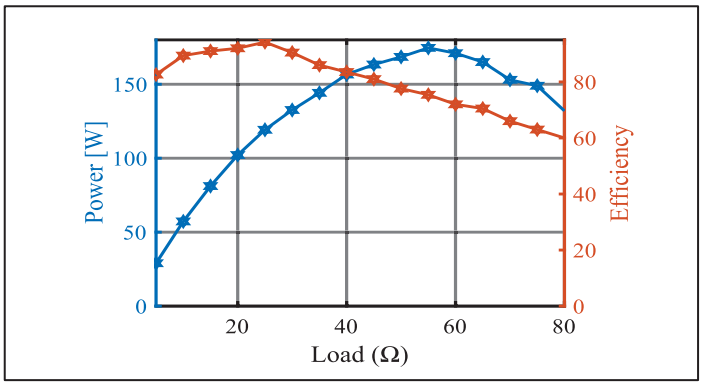

Figure 2.16 Coil-to-coil efficiency and output power as load varies at a transmission distance of 30mm

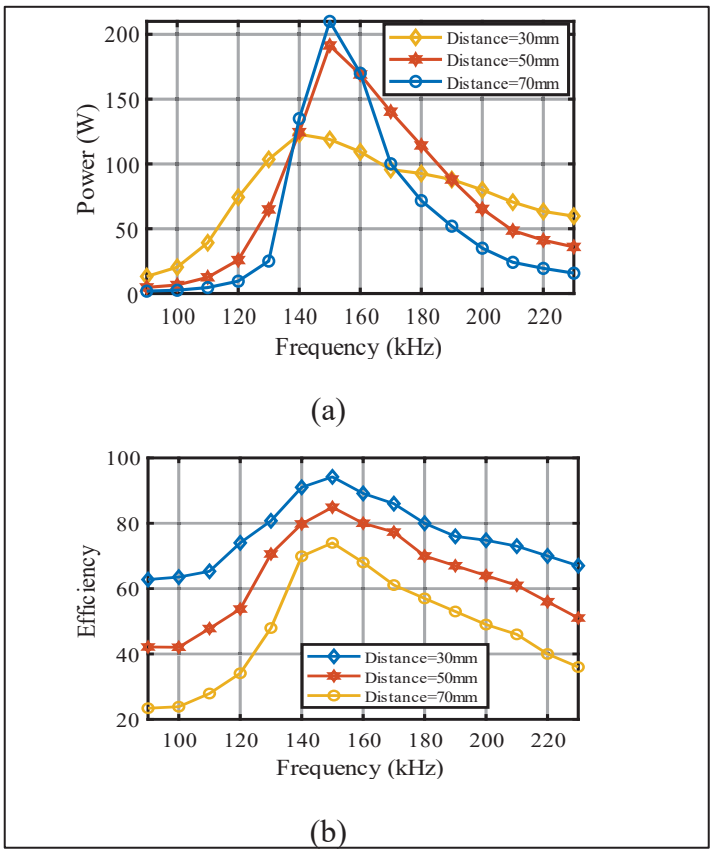

Figure 2.17 Output power and efficiency at different frequency when distance is 30, 50, and 70mm. (a) Output power, (b) Efficiency

Keep the load at 25 Ω, the resonant power and efficiency at different transmission distance are given in Figure 2.18. The maximum power appears when the distance is 50mm. Due to the

decrease in coupling coefficient as the distance increases, the efficiency also decreases. The maximum efficiency is achieved when the distance is 30 mm. Figure 2.19 displays the steady-state voltage and current waveforms of both the transmitter and receiver when the load is 25 Ω, transmission distance is 30 mm, and operating frequency is 147.5 kHz. It's noteworthy that there is no phase difference between the voltage and current of the receiver. Consequently, the proposed coil attains a maximum efficiency of 94.7% and achieves maximum power transfer of 210W. Fig.20 indicates thermal tests on the WPT system at 220W output power, captured by the FLIR thermal camera, showed a maximum temperature of 28.4°C on the self-resonant coil pads. This temperature is within acceptable limits, indicating effective thermal management of the system. The performance of the proposed RWPT system is summarized in Table V.

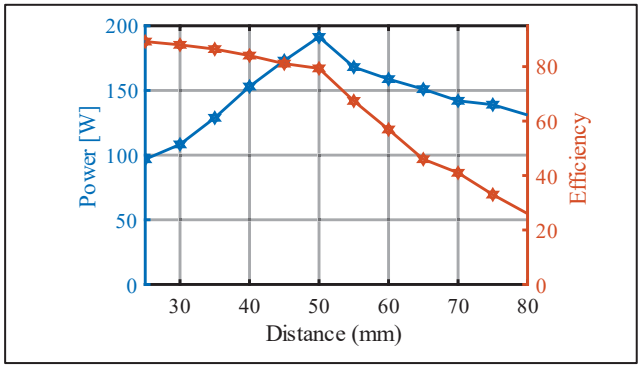

Figure 2.18. Output power and efficiency at different distances when the load is 25Ω

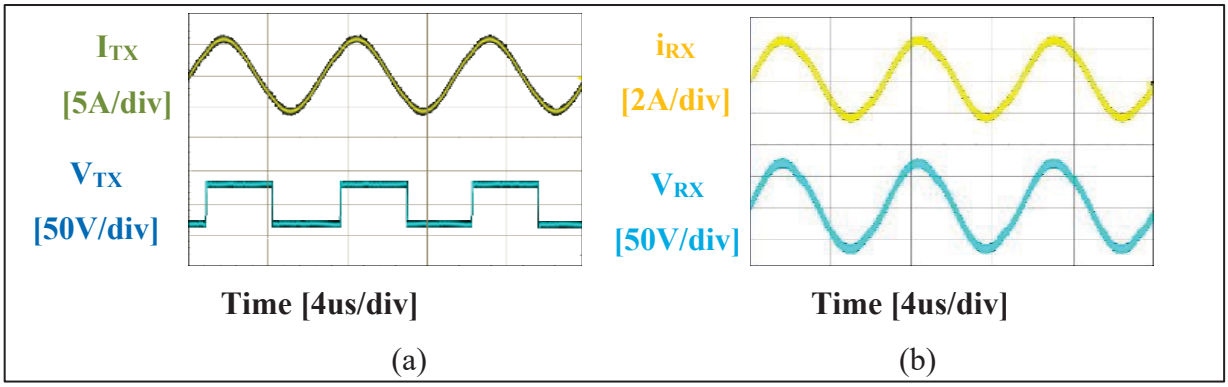

Figure 2.19. Steady-state voltage and current waveforms. (a) Transmitter coil, (b) Receiver coil

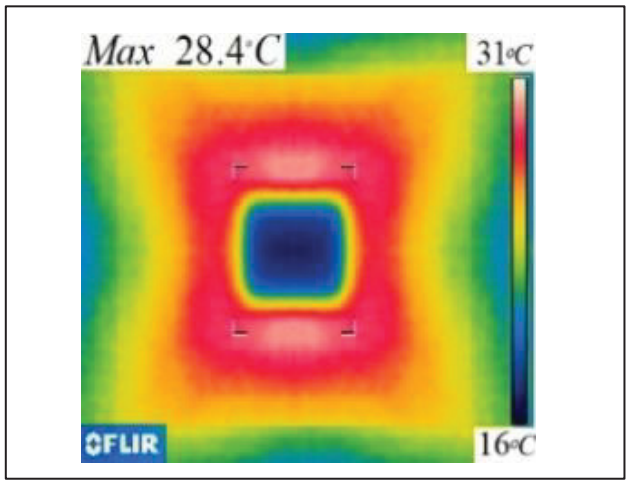

Figure 2.20 Thermal image of self-compensated WPT coil

Table 2.5 Hardware Proposed Specification

Parameter	Values
Parasitic capacitance	145.37 nF
Inductance	25.6 uH
Quality factor	123
Resonnat frequency	147.5 kHz
Input voltage	80 V
Output voltage	73 V
Output power	210 W
Efficiency	94.7%

2.5 Conclusion

This paper proposes a novel multilayer PCB coil for SRWPT systems. By connecting six double-layer PCB coils in parallel, the resonant frequency has been reduced to 147.5kHz. TWR and TGR have been employed in the coil design, which significantly reduces resistance and increases quality factor. Comprehensive theoretical analysis has been conducted to show the operating principle of the proposed SRWPT system. Finite element method is employed to

compare the proposed TWR-TGR coil with a traditional square coil and a TWR coil. Two TWR-TGR coils are fabricated and a SRWPT system is established. Experimental results demonstrate a maximum efficiency of 94.7%, a maximum power of 210 W, quality factor of 123 when the proposed SRWPT system works at its resonant frequency of 147.5 kHz.

CHAPTER 3

PERFORMANCE COMPARISON OF COIL GEOMETRIES IN SELF-RESONANT WIRELESS POWER TRANSFER SYSTEM

Neda Zahedi Saadabad [a], Qingsong Wang [a], Ambrish Chandra [a]

[a] Department of Electrical Engineering, École de technologie supérieure,
1100 Notre-Dame Ouest, Montréal, Québec, Canada H3C1K3

Article published in *Journal of IEEE Transaction on Industry Applications, February 2025* vol. 61 (2025), available at https://ieeexplore.ieee.org/abstract/document/10900424

Abstract

A self-resonant wireless power transfer (SRWPT) system offers exceptional reliability by eliminating the need for physical compensation capacitors. Planar coils with parasitic capacitance between adjacent layers are particularly ideal for such systems. The geometry of the coil significantly influences the performance of the WPT system. This paper thoroughly examines and compares four prominent coil geometries: circular, square, hexagonal, and octagonal. By optimizing the track-width ratio and track-gap ratio, the AC resistance of these PCB coils is markedly reduced, leading to highly efficient SRWPT systems. Comprehensive equivalent circuit models and theoretical frameworks for the inductance and capacitance of these PCB coils have been developed. The finite element method (FEM) is employed to optimize coil design and simulate performance. Four distinct SRWPT coils were constructed and subjected to rigorous experimental testing to evaluate their effectiveness. Results reveal that the hexagonal planar coil can transfer the highest power, at 82.3W, while the square coil achieves the highest efficiency of 93% and the highest quality factor of 54.

3.1 Introduction

Wireless Power Transfer (WPT) systems have gained significant attention due to their capacity to transmit power without the need for physical connectors, offering distinct advantages in terms of safety, convenience, and adaptability (Li, Wu, Yucel & Hui, 2023; Wang, Wang, Li, Yang & Hui, 2024). These systems operate based on the magnetic coupling between the transmitter and receiver coils, facilitating wireless energy transfer across a wide range of applications, such as medical implants (Campi et al., 2021), household appliances (Zhang, Georgiadis & Cecati, 2019), and electric vehicles (Wu, Liu, Zhou, Mao & Zhang, 2023). However, as the distance between the transmitter and receiver increases, flux leakage becomes a critical issue, leading to a reduction in power transfer efficiency. To mitigate this challenge, compensation circuits are employed on both the primary and secondary sides of the system. These circuits are designed to sustain resonance, thereby enhancing power transfer efficiency, particularly over longer distances (Yue Kang et al., 2023; Hou Xinyu et al., 2022; Saket, Shafiei & Ordonez, 2016; Shahsevani & Beiranvand, 2024).

In (WPT) systems, compensation capacitors can experience high voltage and current under resonant conditions, increasing the risk of failure. Moreover, their use adds to the size, cost, and reduces system reliability. To address these challenges, Self-Resonant WPT (SRWPT) systems harness parasitic capacitance from coil turns or parallel plates, thereby eliminating the need for physical capacitors and significantly improving both performance and reliability (Zahedi, Wang & Chndra, 2023; Wang, Saket, Troy & Ordonez, 2020; Xiang, Jiang, Ma, Wang & Fan, 2024).

Planar coils are well-suited for self-resonance, leveraging parasitic capacitance between layers for compensation. The coil geometry plays a pivotal role in minimizing energy losses in Resonant Inductive Wireless Power Transfer (RIWPT) systems (Yi, Li, Muneer, He & Yang, 2020). Evaluating various coil geometries is crucial for selecting the optimal design, as it influences the inductance, inter-capacitance, resonant frequency, coupling coefficient, and overall system performance. Additionally, the geometry affects alignment tolerance and efficiency, ensuring that the final design meets the specific requirements of WPT applications (Son, Shrestha & Williamson, 2024; Aydin, Kosesoy, Yildiriz & Aydemir, 2018; Ongayo &

Hanif, 2015; McDonough & Fahimi, 2014; Shevchenko, Husev, Pakhaliuk, Karlov & Kondratenko, 2019; Knaisch, Springmann & Gratzfeld, 2016; Zahedi, Wang & Chndra, 2023). Numerous studies have investigated various conventional coil geometries. In (Son, Shrestha & Williamson, 2024), a comparative analysis of circular, rectangular, and hexagonal coils highlights that circular coil offer the lowest resistance and highest safety, while rectangular coils excel in alignment tolerance for WPT applications. In (Aydin, Kosesoy, Yildiriz & Aydemir, 2018), a comparison of circular, rectangular, square, and hexagonal coils with identical areas shows that the circular coil achieves the highest coupling coefficient, while the hexagonal coil demonstrates superior misalignment tolerance. In (Ongayo & Hanif, 2015), it is found that while the rectangular coil has higher self-inductance, the circular coil provides a superior coupling coefficient, a conclusion also supported by (McDonough & Fahimi, 2014; Shevchenko, Husev, Pakhaliuk, Karlov & Kondratenko, 2019; Knaisch, Springmann & Gratzfeld, 2016). However, these studies do not consider self-resonant coil geometries nor provide a comprehensive comparison, focusing primarily on isolated parameters such as coupling coefficient or alignment tolerance.

This paper extends the work presented in (Zahedi, Wang & Chndra, 2023), which focuses on self-resonant coil designs, including hexagonal, circular, and square coils. Our study further expands on this by analyzing and comparing four primary planar coil geometries square, circular, hexagonal, and octagonal, in the context of self-compensated wireless power transfer WPT systems. The study examines essential parameters, including self-inductance, inter-capacitance, resonant frequency, mutual inductance, coupling coefficient, coil resistance, output power, and efficiency across different transmission distances. Aiming to improve quality factor and efficiency, this study introduces a novel coil design that integrates both track-width-ratio (TWR) and track-gap-ratio (TGR). By adjusting these parameters, the design effectively reduces AC resistance, primarily by suppressing the proximity effect that impacts coil performance. This reduction in AC resistance results in a more efficient energy transfer, making the design especially beneficial for high-frequency WPT applications. This paper is organized as follows: the second section presents the configuration and theoretical analysis of

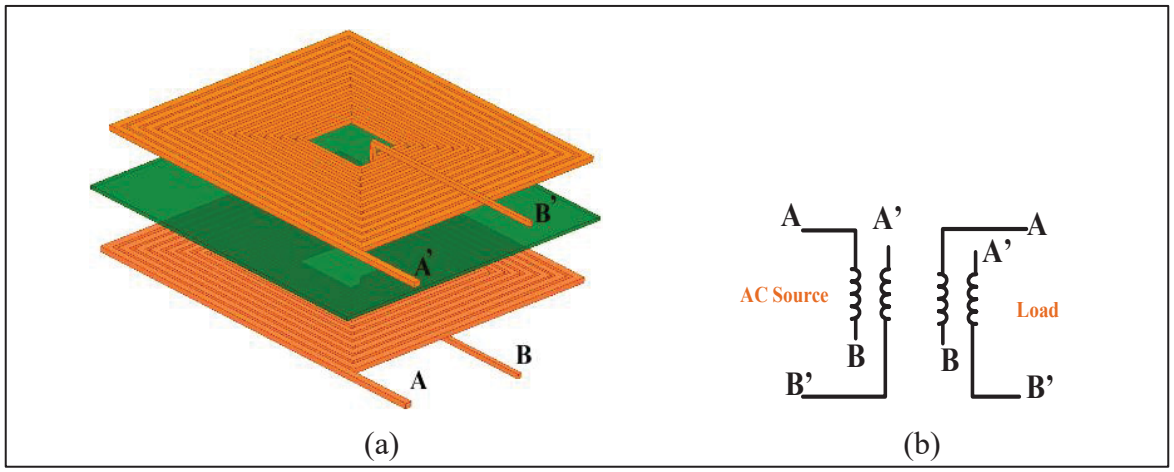

Figure 3.1 (a) Structure of the double layer square coil, (b) equivalent circuit of the coils

the coils, section III gives the design optimization and simulation results, experimental validation is presented in section IV, and the conclusion is summarized in section V.

3.2 Coil Topologies and Theoretical Models

3.2.1 Coil Topology

Figure 3.1 (a) depicts a double-layer PCB with square spiral coil, utilizing a dielectric layer between the coils to generate intra-winding capacitance. As illustrated in Figure 3.1 (a), terminals A' and B are left open, while terminals A and B' are connected to an AC source, creating a series LC resonant circuit. The design employs a hollow spiral structure and track-width-ratio (TWR), and track-gap-ratio (TGR) has been applied to minimize AC resistance by keeping current away from the central high magnetic field area. This method effectively reduces resistance across different coil geometries and improves the quality factor of the coils. The same design method has been applied to circular, hexagonal, and octagonal coils.

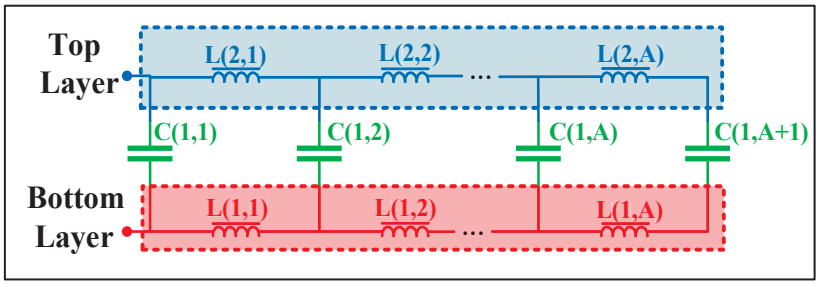

Figure 3.2 Equivalent circuit of the double layer planar coil

3.2.2. Equivalent Circuit

Four double-layer self-compensated WPT coils with square, circular, hexagonal, and octagonal geometry, each with 'A' identical turns per layer, are analyzed. Each turn is a single-turn inductor, denoted L(n,A), where n is the layer and A is the turn. Capacitance between the top and bottom conductors, C(n,A), depends on the conductor's subtended area, dielectric thickness, and conductivity.

3.2.2.1 Equivalent Capacitance

As shown Figure 3.2, L(1,n) and L(2,n) have the same length, they also have the same inductance. Thus, we have:

$$L(1,n)=L(2,n)\ ,\ n=1,2,\dots,A \tag{3.1}$$

For the double-layer coil with A loops, the voltages across the inductors L(1,A) and L(2,A) are given by:

$$V_{L(1,A)} = L_{(1,A)}di/dt, \quad V_{L(2,A)} = L_{(2,A)}di/dt \tag{3.2}$$

Due to identical materials in each coil, the inductance for each nth turn is consistent across layers. As a result, the voltages $V_{L(1,A)}$ and $V_{L(2,A)}$ across the inductors are identical. In a two-layer coil loop, the voltage is described by the following equation:

$$V_{C(1,1)} + \sum_{a=1}^{A} V_{L(2,a)} = V_{C(1,A+1)} + \sum_{a=1}^{A} V_{L(1,a)} \tag{3.3}$$

Here, $V_{C(1,\ A)}$ is the voltage across the capacitor between the conductors. Equal inductor voltages imply equal capacitor voltages. Thus:

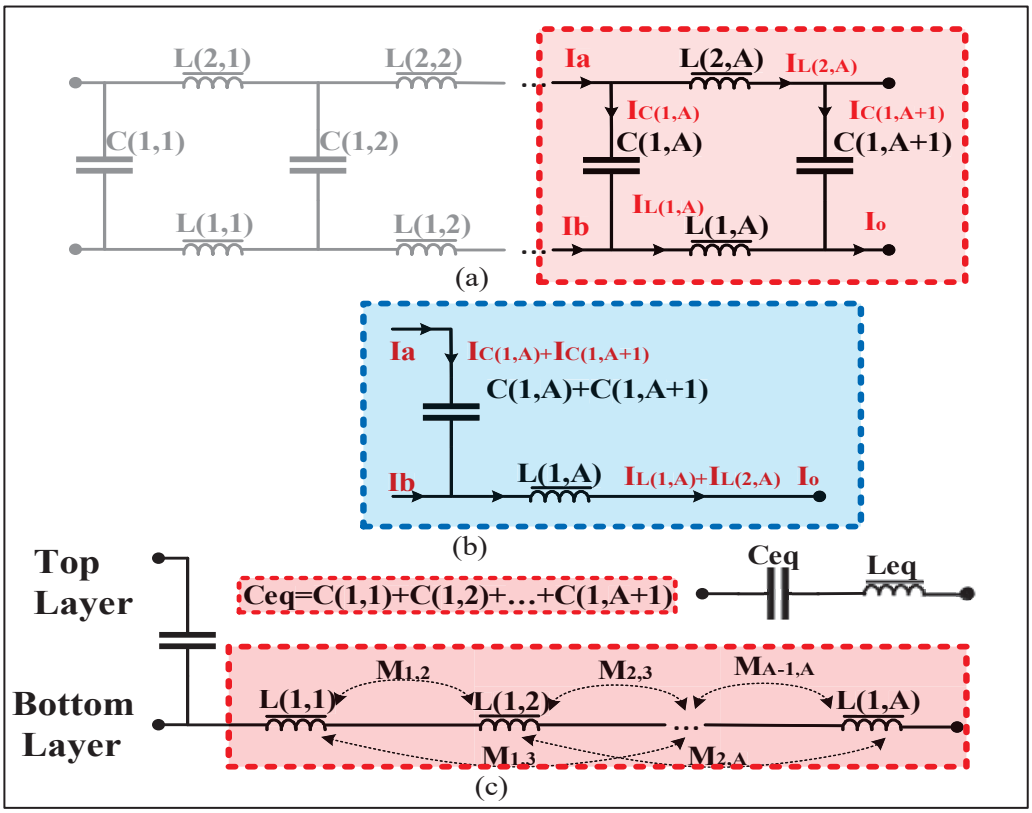

Figure 3.3 Equivalent circuit of a double-layer coil. (a) Circuit with distributed inductance and capacitance. (b) Circuit shows equivalent capacitance and inductance of the end loop. (c) Final equivalent circuit

$$V_{C(X,1)} = V_{C(X,A+1)},\ \text{X=1,2} \tag{3.4}$$

By applying Kirchhoff's Current Law (KCL), the equivalent capacitance of a double-layer coil can be determined. As illustrated in Figure 3.3 (a), designate I_a and I_b as the input currents, and I_o as the output current. According to KCL, the relationship is as follows:

$$I_a = C_{(1,A)} \frac{dv_{C(1,A)}}{dt} + C_{(1,A+1)} \frac{dv_{C(1,A+1)}}{dt} \tag{3.5}$$

Given that the voltages across the capacitors are equal as illustrated in Fig.3 (b), the equation in (3.5) can be expressed as:

$$I_b = (C_{(1,A)} + C_{(1,A+1)}) \frac{dv_{C(1,A)}}{dt} = (C_{(1,A)} + C_{(1,A+1)}) \frac{dv_{C(1,A+1)}}{dt} \tag{3.6}$$

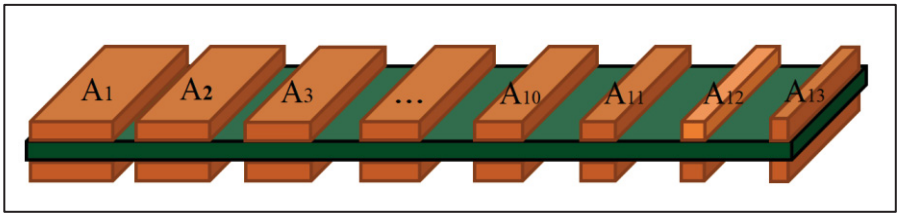

Figure 3.4 Calculations of capacitance in double layer WPT coils

Thus, the total capacitance is obtained by adding the capacitances of each individual section. For modeling the intra-winding capacitance, the coil features two layers with a dielectric material positioned between them. The electric field within this setup consists of a vertical component passing through the dielectric and minor fringing fields occurring between adjacent traces. As shown in Figure 3.4, a delicate dielectric layer is sandwiched between two copper layers. The capacitance between these upper and lower conductors is determined similarly to that of a parallel plate capacitor. The total area of each layer is calculated by summing the areas of all individual turns:

$$A_T = A_1 + A_2 + \ldots + A_N \tag{3.7}$$

Thus, the intra-winding capacitance between the layers is calculated using the formula:

$$C_{Layer-Layer} = k\varepsilon_o \frac{A}{d} \tag{3.8}$$

where d denotes the dielectric thickness, k is the relative permittivity of the dielectric material, and ε_0 represents the permittivity of free space.

3.2.2.2 Equivalent Inductance

By assessing the voltage across L(1,A) , the coil's equivalent inductance can be determined. This voltage is comprised of the self-inducted component as well as the voltage contributed by L(2,A), as outlined below:

$$V_{L(1,A)} = L_{(1,A)} \frac{dI_{L(1,A)}}{dt} + M_{(1,A)(2,A)} \frac{dI_{L(2,A)}}{dt} \tag{3.9}$$

In this context, M denotes the mutual inductance linking L(1,A) and L(2,A), which is expressed as:

$$M_{(1,A)(2,A)} = K_{(1,A)(2,A)} \sqrt{L_{(1,A)} L_{(2,A)}} \tag{3.10}$$

Considering the consistent coil design and the thin layer of insulation, the coupling coefficient K is assumed to be 1. As a result, the self-inductance of the coils is equal to their mutual inductance. Consequently, the voltage across the inductance L(1,A) can be written as follows:

$$V_{L(1,A)} = L_{(1,A)} \frac{d(I_{L(1,A)} + I_{L(2,A)})}{dt} = L_{(1,A)} \frac{dI_o}{dt} \tag{3.11}$$

As illustrated in Figure 3.3 (c), the equivalent circuit for the nth loop consists of an inductor and a capacitor. Thus, the circuit can be represented by a series combination of a capacitor and an inductor. The total inductance modeling of self-resonant coils is comprised of the self-inductance and the mutual inductance between turns as given by:

$$L = L_S + M_{Positive} + M_{Negative} \tag{3.12}$$

Due to the thin thickness of the dielectric layer, the current path in the double self-compensated coil is almost identical to that of a conventional planar spiral inductor. Consequently, both coils possess the same inductance. The inductance of a planar spiral coil is:

$$L_S = \frac{\mu N^2 D_{average} A_1}{2} \left[ln\left(\frac{A_2}{B}\right) + A_3 B + A_4 B^2 \right] \tag{3.13}$$

Where μ is the magnetic permeability, N is the number of turns, the coefficients A_i (for (i = 1, 2, 3, 4)) represent different coil shapes. The specific values for these coefficients can be found in table 3.1. Average diameter D_{ave} and B can be calculated as follows:

Table 3.1 Coefficient value

Coil	A_1	A_2	A_3	A_4
Square	1.27	2.07	0.18	0.13
Circle	1.00	2.46	0.00	0.20
Hexagonal	1.09	2.23	0.00	0.17
Octagonal	1.07	2.29	0.00	0.19

$$D_{average} = \frac{D_{in}+D_{out}}{2}, B = \frac{D_{out}-D_{in}}{D_{out}+D_{in}} \tag{3.14}$$

Where D_{in} and D_{out} are the inner diameter and outer diameter of the coil. Positive mutual inductance arises when the currents in the coil sections flow in the same direction, while negative mutual inductance occurs when the currents are directed oppositely. The following equations detail how to calculate both positive and negative mutual inductance:

$$M_{Positive} = 4\sum_{i=1}^{N}\sum_{j=1}^{N-k} M(i, i+j) \tag{3.15}$$

$$M_{Negative} = 2\sum_{i=1}^{N}\sum_{j=1}^{N} M(i, j) \tag{3.16}$$

3.2.2.3 Equality Factor Modeling

The inductance, resistance, and capacitance underscore the influence of variations in the number of turns, width, gap, and thickness of the traces in the multi-layer planar coil. Thus, the quality factor of the whole system can be derived from (3.17):

$$Q = \frac{wL_{eq}}{R_{eq}} \tag{3.17}$$

Where, R_{eq} is the equivalent resistance, incorporating the skin effect and proximity effect, can be calculated according to (Awuah, Danuor, Moon & Jung, 2023), while the dielectric losses can be determined as outlined in (Li & Costinett, 2018).

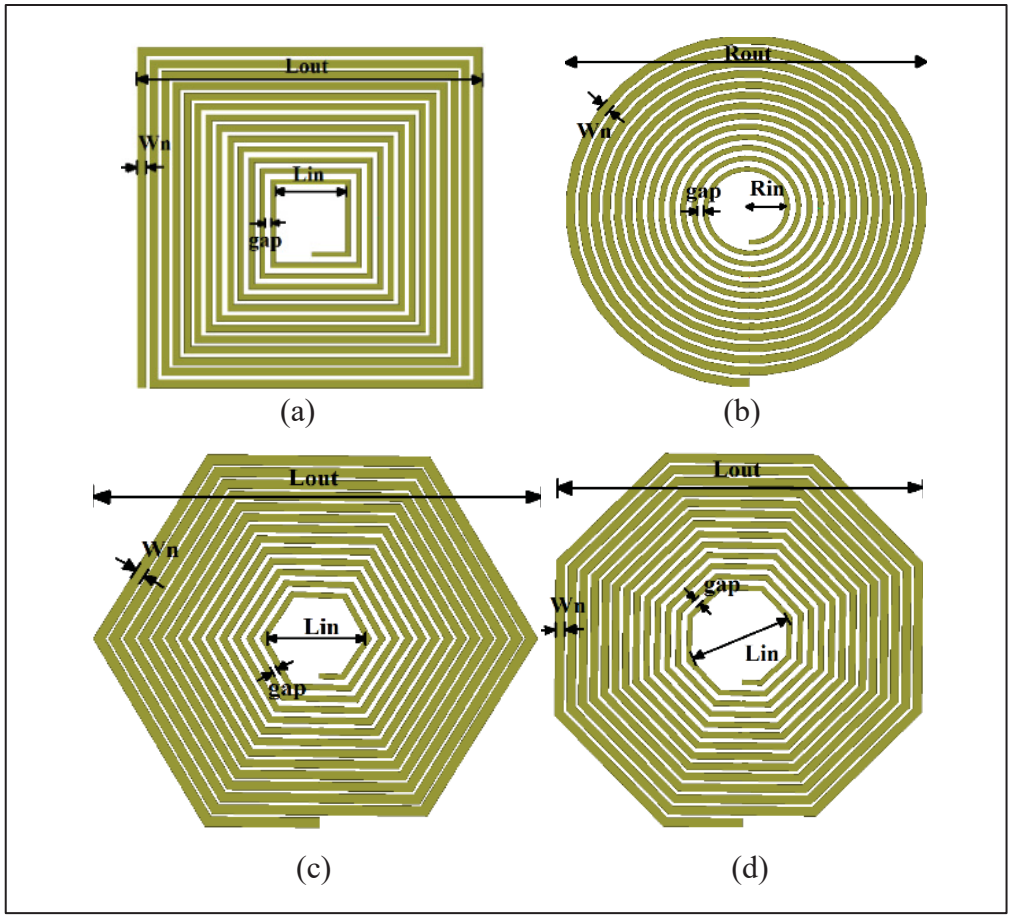

Figure 3.5 Schematics of spiral arrangement of different coil geometries. (a) square, (b) circular, (c) hexagonal, (d) octagonal

3.3 Coil Optimization and Simulation

To achieve optimal performance in SRWPT systems, it is essential to fine-tune parameters such as conductor width, turn spacing, and inner coil length. Key performance indicators, including quality factor, resonant frequency, and transfer efficiency, are significantly influenced by AC resistance, inductance, and intra-winding capacitance of the coils. Increasing the number of coil turns can effectively lower the resonant frequency, as inductance and intra-winding capacitance increases with additional turns. However, this can also result in a larger coil size or higher AC resistance. Therefore, meticulous adjustment of these parameters is crucial to ensuring that the RWPT system meets the desired performance criteria efficiently.

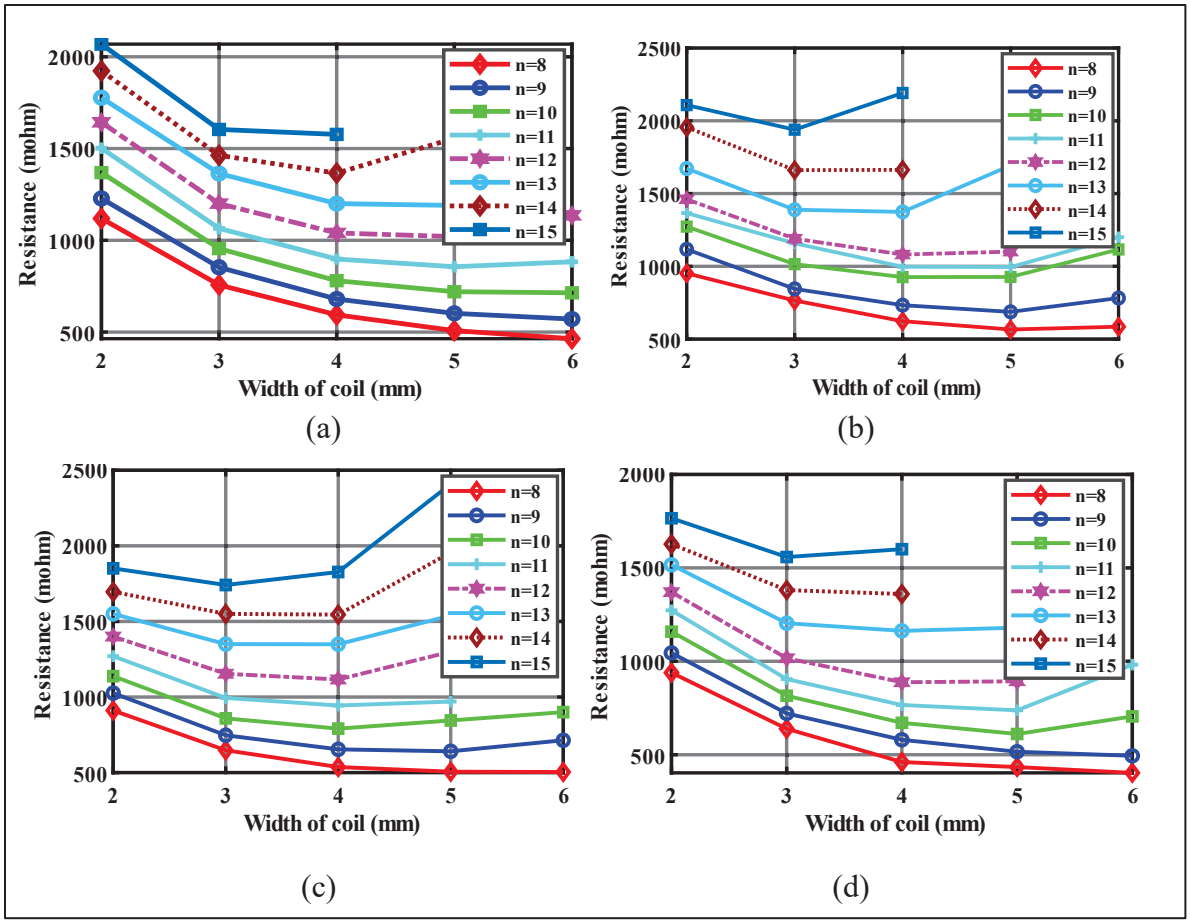

Figure 3.6 Influence of number of turns and coil width on the resistance. (a) Square, (b) Circular, (c) Hexagonal, (d) Octagonal

3.3.1 Traditional Coil

To optimize the SRWPT system within practical fabrication constraints, we focus on adjusting specific design variables while keeping certain parameters fixed. For all the coils, the design variables include the number of turns (n), coil width (W), and the gap between wires (g) as shown in Figure 3.5. Fixed parameters are the inner/outer radius, inner/outer length, dielectric thickness, and wire thickness. A constant thickness of dielectric is 0.17mm, and coil thickness of 72 μm is chosen to facilitate fabrication and mitigate the skin effect, with FR4 as the dielectric material. Figure 3.6 (a) to (d) illustrate the resistance of four different coils as a function of various widths and numbers of turns. The data reveal that resistance initially

decreases with increasing width due to the larger cross-sectional area, which effectively lowers resistance. However, as the width continues to increase, proximity effects become more pronounced, causing a rise in resistance for a given size. While increasing the number of turns

Table 3.2 Design parameters

Parameter	|Square	Circle	Octagonal	Hexagonal
Number of turns	13	13	13	13
Inner length/ radius	40	20	25	20
Outer length/radius	200	200	200	200
Thickness of trace	0.072	0.072	0.072	0.072
Outer coil width	5	5	5	5
Scaling factor	0.9	0.9	0.9	0.9
Inter-turn gap	3.7	3.7	3.7	3.7
Thickness of dielectric	0.17	0.17	0.17	0.17

enhances inductance and capacitance, it also raises resistance and lowers the quality factor. To achieve an optimal balance, all coils are designed with 13 turns and a width of 5mm. Additionally, to ensure a fair comparison, the inner and outer lengths of all coils are kept consistent.

3.3.2 TWR-TGR Coil

Inner turns experience higher proximity-effect resistance loss (R_{pr}) due to stronger magnetic fields. Narrowing trace widths reduces R_{pr} but increases skin-effect resistance (R_{sk}). Increasing the spacing between turns also lowers R_{pr}, as the magnetic field mainly comes from adjacent turns. Our novel TWR-TGR coil layout addresses this by employing narrower trace widths combined with wider spacing between turns, achieving a balanced reduction in both R_{sk} and R_{pr}, and consequently, an improved quality factor. In the proposed TWR-TGR coil, the conductor width (w) gradually increases from the inner turns outward, while the gap between adjacent conductors decreases. Once the width of the outermost wire (w) is determined, the width of each inner wire is reduced exponentially by a scaling factor (α) for each turn (n) as follows:

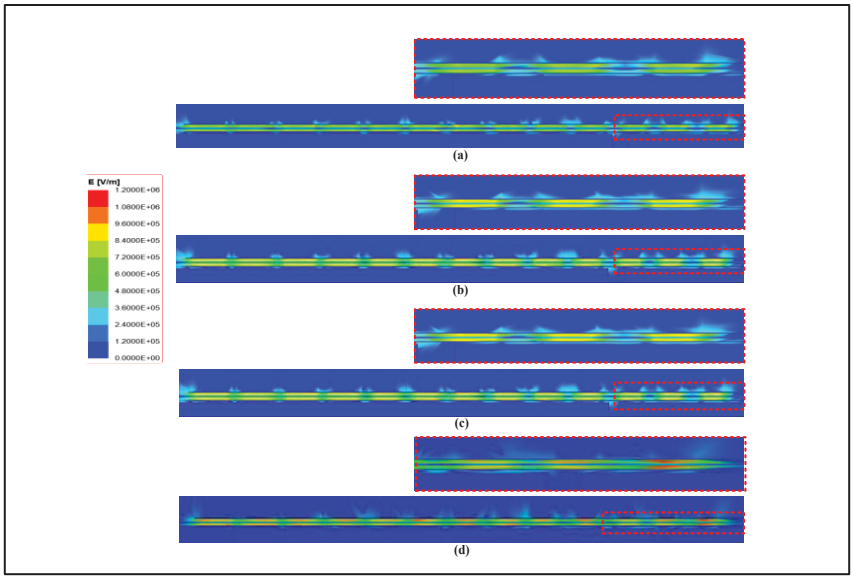

Figure 3.7 Insulation evaluations. (a) Square, (b) Circular, (c) Hexagonal, (d) Octagonal

$$w_n = \alpha^{n-1} W \tag{3.18}$$

Where n indicates the turn number, starting from outer turn, ranging from 1 to N. Additionally, the gap (g) between the wires widens from the center towards the outer edge of the coil from 3.7mm, 3.5mm, …, 2.1mm. These adjustments result in reduced losses. All values are detailed in table 3.2.

3.3.3 Insulation Evaluations

To prevent electrical breakdown between adjacent turns and layers, we evaluated the electric field distribution in the coils and shown in Figure 3.7 The maximum potential differences at each coil's resonant frequency, and when the current is 10A are as follows: 0.578 kV, 0.61kV, 0.636kV, and 0.603kV for the square, circular, octagonal, and hexagonal coils, respectively. Considering that the dielectric strength of FR4 with a thickness of 0.17 mm is 20 kV/mm, the FEA results indicate that the electric field distributions are well within the material's dielectric strength limits. This confirms that the coils are capable of sustaining significantly higher

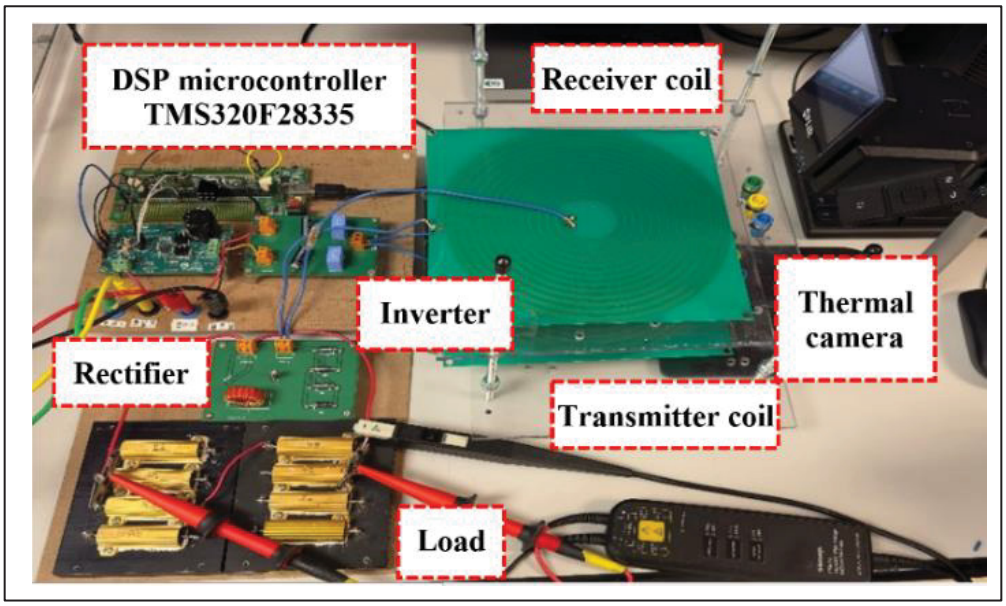

Figure 3.8 Experimental test setup.

currents and exhibit excellent insulation properties. Among the tested coil geometries, the square coil demonstrates the lowest electric field distribution, highlighting its superior capability to handle high currents and efficiently transfer power.

3.4 Experimental Results

Four self-resonant coils, specified in table 3.2, were fabricated, and experimental tests were conducted to validate the design's effectiveness. Figure 3.8 illustrates the experimental setup, featuring a 50 mm air gap between the transmitter and receiver coils. The DC/AC inverter is built using an H-bridge configuration with MOSFETs (STL33N60DM2), generating high-frequency AC input for the transmitter, which operates at a 50% duty cycle. PWM signals are produced by the DSP controller TMS320F28335, with a dead time set to 40 ns. Power input is supplied by a 6554A DC power source. The rectifier connected to the receiver utilizes Schottky diodes (MBR10200FH-BP). Thermal distribution is monitored with a FLIR ETS320 thermal camera.

Figure 3.9 illustrates the self-inductance characteristics with and without a ferrite core under varying vertical distances and horizontal misalignments for four different coils. As shown in Figure 3.9 (a) and (c), the presence of a ferrite core leads to significant inductance variations at very low distances, whereas horizontal misalignments only cause minor changes. In contrast,

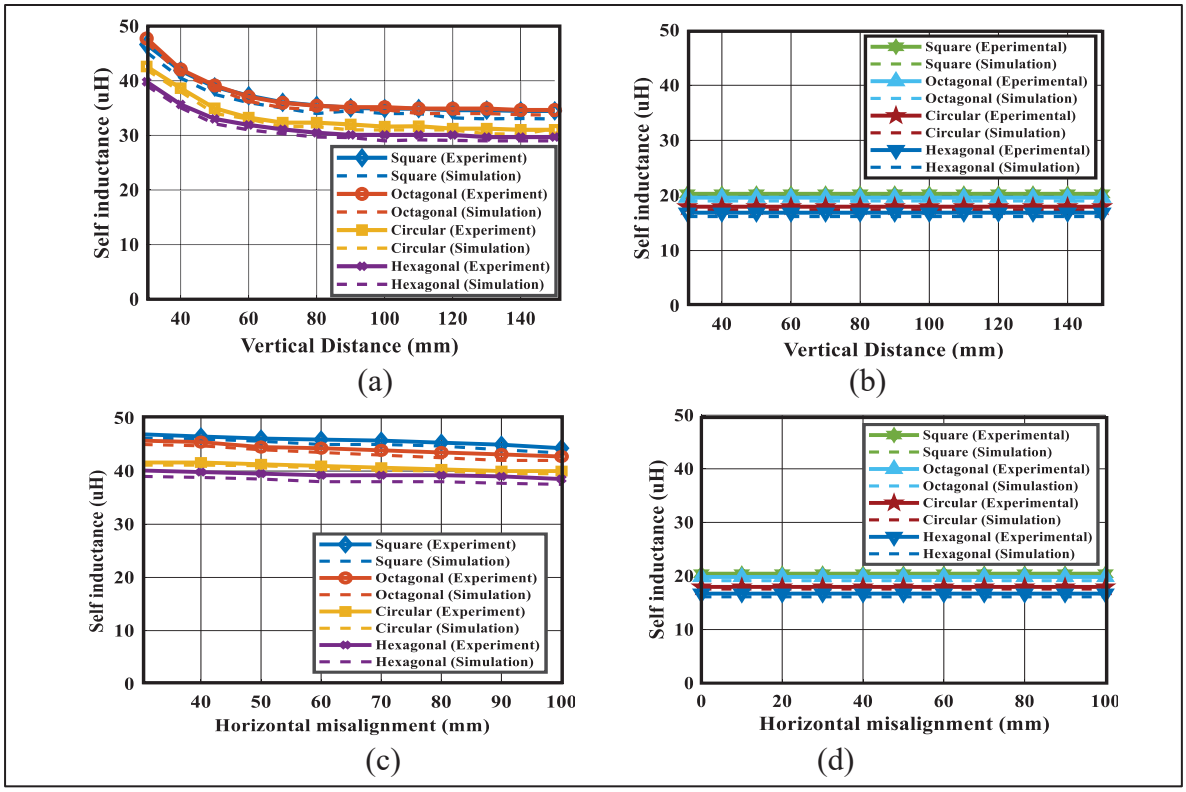

Figure 3.9 Experimental measurements and simulation results of the self-inductance in different distances for square, circular, hexagonal, and octagonal coil geometries. (a) in vertical distances with ferrite core, (b) in vertical distances without ferrite (c) in horizontal misalignments with ferrite, (d) in horizontal misalignments without ferrite

without a ferrite core as shown in Figure 3.9 (b) and (d), the inductance remains consistent regardless of horizontal and vertical distances. These minimal variations during substantial misalignments indicate that the integrated capacitor can sustain resonance despite some misalignment. The figures reveal that square and octagonal coils exhibit the highest self-inductance values, primarily due to their geometry, which results in a longer conduction path compared to circular and hexagonal coils. Significant variations are observed at distances less than 50 mm for square and octagonal coils. In contrast, the circular coil shows slightly lower inductance values, while the hexagonal coil consistently demonstrates the lowest inductance with only minor variations. Furthermore, corresponding simulations performed in ANSYS Maxwell yielded comparable results, further validating the experimental findings.

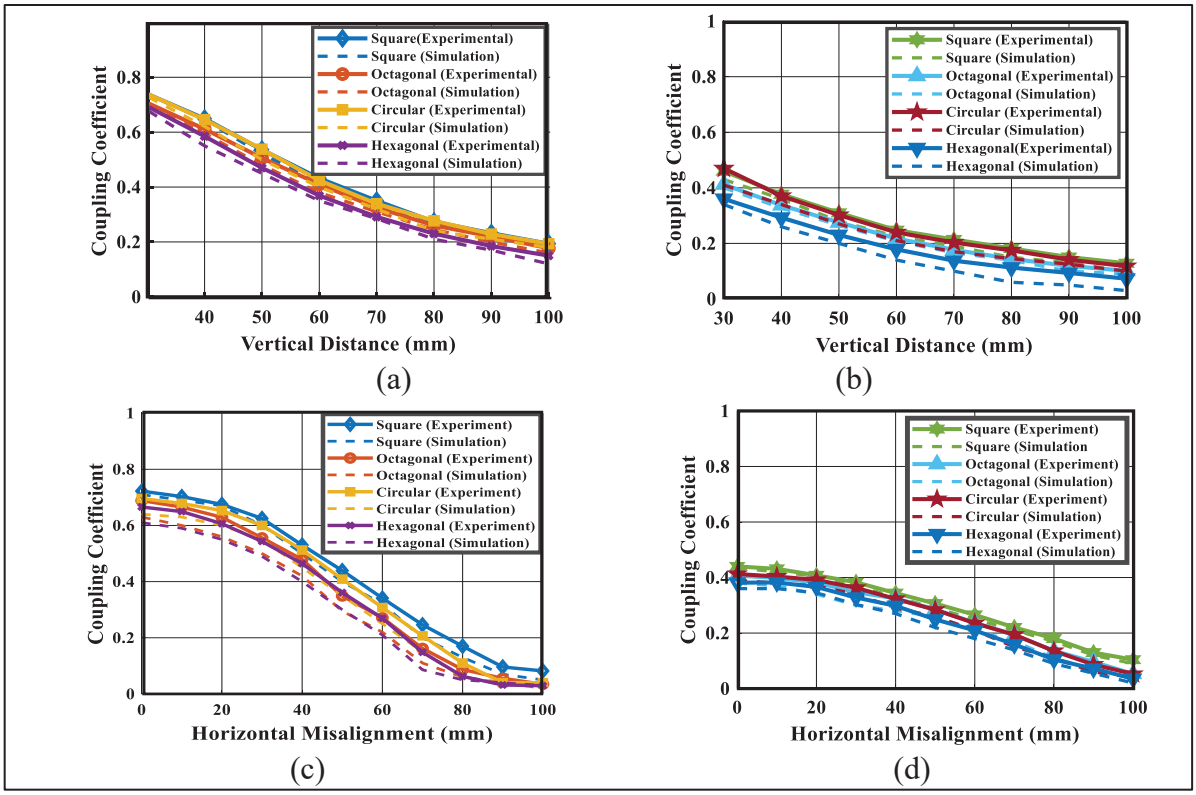

Figure 3.10 Experimental measurements and simulation results of the coupling coefficient in different distances for square, circular, hexagonal, and octagonal coil geometries. (a) in vertical distances with ferrite core, (b) in vertical distanced without ferrite (c) in horizontal misalignment with ferrite core, (d) in horizontal misalignment without ferrite core

Figure 3.10(a) further reveals that the coupling coefficient with a ferrite core decreases more sharply, particularly at larger distances, compared to the system without a ferrite core, as shown in Figure 3.10(b). Meanwhile, Figure 3.10(c) and 3.10(d) demonstrate that both configurations, with and without the ferrite core, experience an exponential decrease in coupling coefficient as vertical misalignment increases. Notably, the square and circular coils outperform the other coil shapes, maintaining a higher coupling coefficient even with increased vertical distance. However, under misalignment conditions, the square coil demonstrates superior performance compared to the circular coil. This enhanced performance contributes to improved efficiency, making both the square and circular coils more effective in preserving strong inductive coupling across varying distances and misalignments. Furthermore, the results from simulations closely align with the experimental findings, further validating the accuracy of the observed performance. Table 3.3 presents the self-inductance results obtained from theoretical

Table 3.3 Comparison results of the calculation, simulation, and measurement of self inductance

Parameter	|Square	Circle	Octagonal	Hexagonal
Calculation W Ferrite (uH)	38.26	34.36	38.14	33.29
Measured W Ferrite (uH)	38.87	34.96	39.14	33.016
Simulation W Ferrite (uH)	38.26	34.65	38.14	33.29
Calculation W/O Ferrite (uH)	19.8	17.2	18.8	16.42
Measured W/O Ferrite (uH)	20.3	17.96	19.6	16.87
Simulation W/O Ferrite (uH)	19.5	17.02	18.93	16.39

calculations, FEA simulations, and experimental measurements at self-resonance frequency for each coil, with and without ferrite cores. The results reveal that the inductance values for the square and octagonal coils are similar, whereas those for the circular and hexagonal coils are comparatively lower. Notably, the measurements, simulations, and calculations are in close agreement with each other. Impedance and phase measurements of self-resonant coils, both with and without ferrite cores, were performed over a frequency range of 150 to 500 kHz using the E5061B ENA Series Network Analyzer. The self-resonant frequency is identified where the impedance reaches its minimum and the phase angle crosses zero, as shown in Figure 3.11 and Figure 3.12 The self-resonant frequencies for the coils without ferrite cores are 329.4 kHz, 394.96 kHz, 365.427 kHz, and 411.939 kHz for the square, circular, octagonal, and hexagonal coils, respectively. When ferrite cores are introduced, these frequencies shift to 235 kHz, 276 kHz, 254 kHz, and 291 kHz for the square, circular, octagonal, and hexagonal coils, respectively. These findings indicate that the square coil, with its highest inductance and inherent capacitance, has the lowest resonant frequency. The octagonal coil follows with a slightly higher frequency, then the circular coil, and the hexagonal coil exhibits the highest resonant frequency among the designs tested.

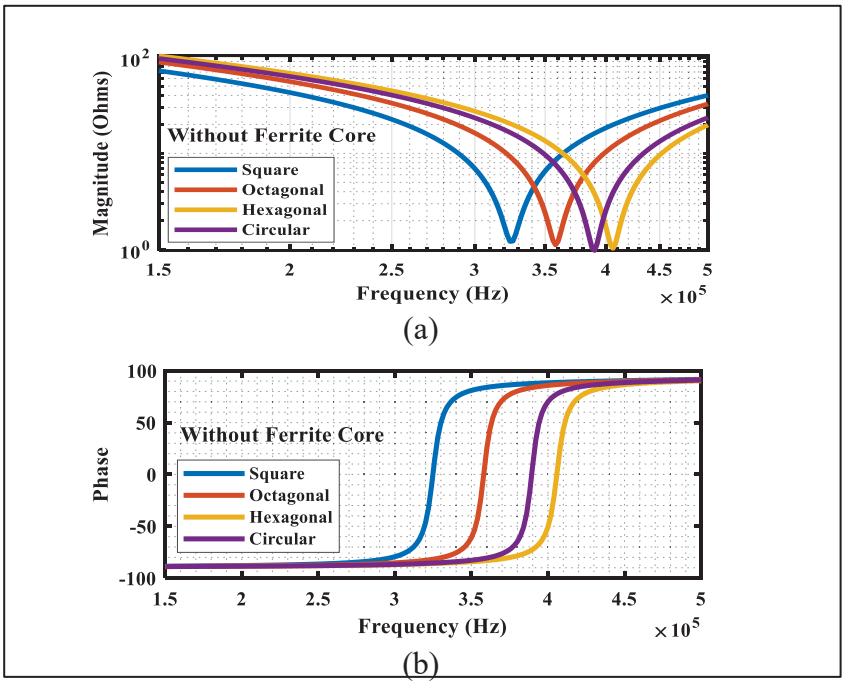

Figure 3.11 Frequency characteristics of self-resonant coils with ferrite cores: (a) impedance and (b) phase angle for four different coil geometries

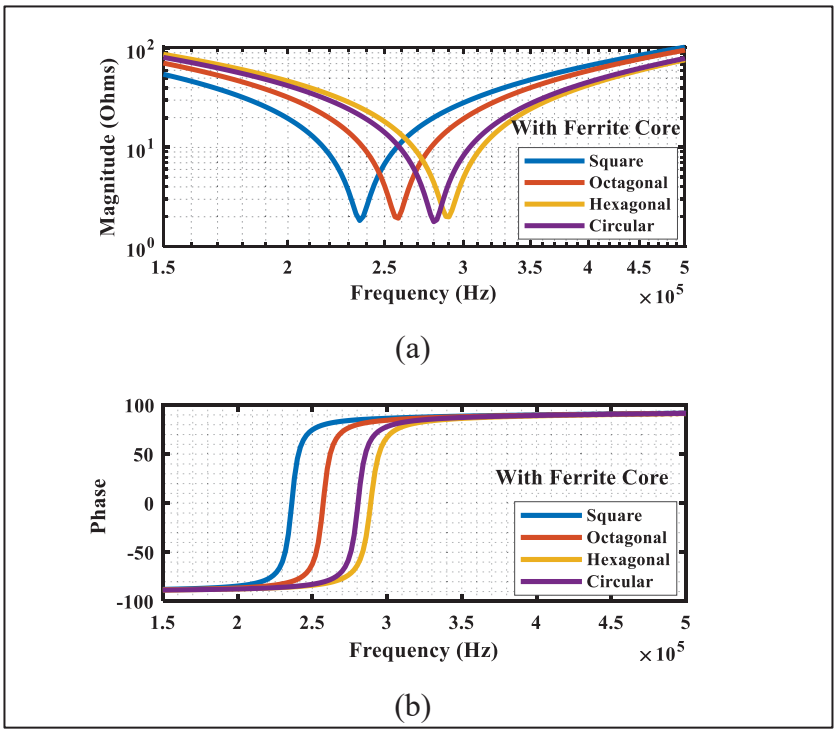

Figure 3.12 Frequency characteristics of self-resonant coils without ferrite cores: (a) impedance and (b) phase angle for four different coil geometries

Table 3.4 Comparison results of the calculation, simulation, and measurement of intra-winding capacitance

Parameter	|Square	Circle	Octagonal	Hexagonal
Calculation W Ferrite (nF)	11.6	9.45	9.51	9.02
Measured W Ferrite (nF)	12.1	9.51	10.03	9.06
Simulation W Ferrite (nF)	11.6	9.42	9.81	8.77
Calculation W/O Ferrite (nF)	11.6	9.45	9.51	9.02
Measured W/O Ferrite (nF)	12.1	9.67	9.91	8.85
Simulation W/O Ferrite (nF)	11.6	9.42	9.81	8.77

The parasitic capacitances measured for the square, circular, octagonal, and hexagonal double-layer coils with ferrite cores are 12.1 nF, 9.51 nF, 10.03 nF, and 9.06 nF, respectively. Table 3.4 provides a comprehensive comparison of intrinsic capacitance results derived from theoretical calculations, finite element analysis (FEA) simulations, and experimental measurements at the self-resonance frequency for each coil, both with and without ferrite cores. The data reveal only minimal variations between capacitance values with and without the ferrite core, indicating that the ferrite core exerts a negligible effect on the overall capacitance. Among the coils, the square coil demonstrates the highest parasitic capacitance, followed by the octagonal, circular, and hexagonal coils. This order underscores the superior performance of the square coil in terms of parasitic capacitance for a given area.

The performance of four self-compensated coils is assessed at transmission distances of 30 mm, 50 mm, and 70 mm, using an input voltage of 80V and a load resistance of 30 ohms, as illustrated in Figure 3.13 and Figure 3.14 respectively. Power and efficiency reach their maximum at the resonant frequencies for each coil. At a 70 mm distance, the hexagonal coils deliver the highest power output of 82.3 W, followed by the square coils at 80.136 W, the circular coils at 78.62 W, and the octagonal coils at 77.894 W. However, as the transmission distance grows, the coupling coefficient decreases, reducing efficiency. Consequently, the

highest efficiency is observed at 30 mm, where the square coil achieves the best efficiency of 93%, followed by the octagonal coils at 91.04%, the circular coils at 90.04%, and the hexagonal coils at 89.57%. The performance of the four self-compensated coils is also simulated under identical conditions using MATLAB and ANSYS Simplorer. The results, presented in Figure 3.13 and Figure 3.14, corroborate the experimental findings, highlighting that maximum power and efficiency are achieved at the resonant frequency for each coil. These simulations further validate that the coils operate at peak performance under resonance, consistent with the observed experimental trends.

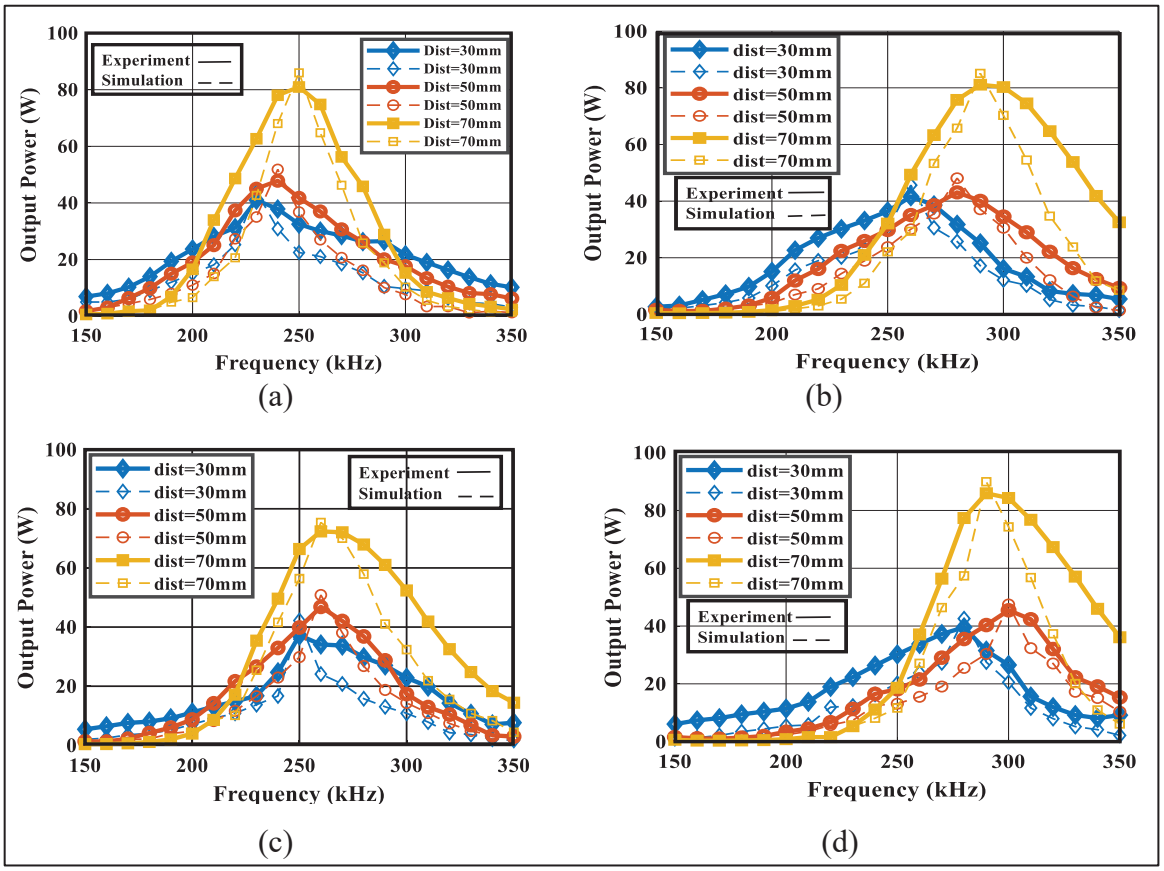

Figure 3.13 Experimental measurement and simulation results of the output power at different frequencies when the distance is 30mm,50mm, and 70mm. (a) Square coils, (b) Circular coils, (c) Octagonal coils, (d) Hexagonal coils

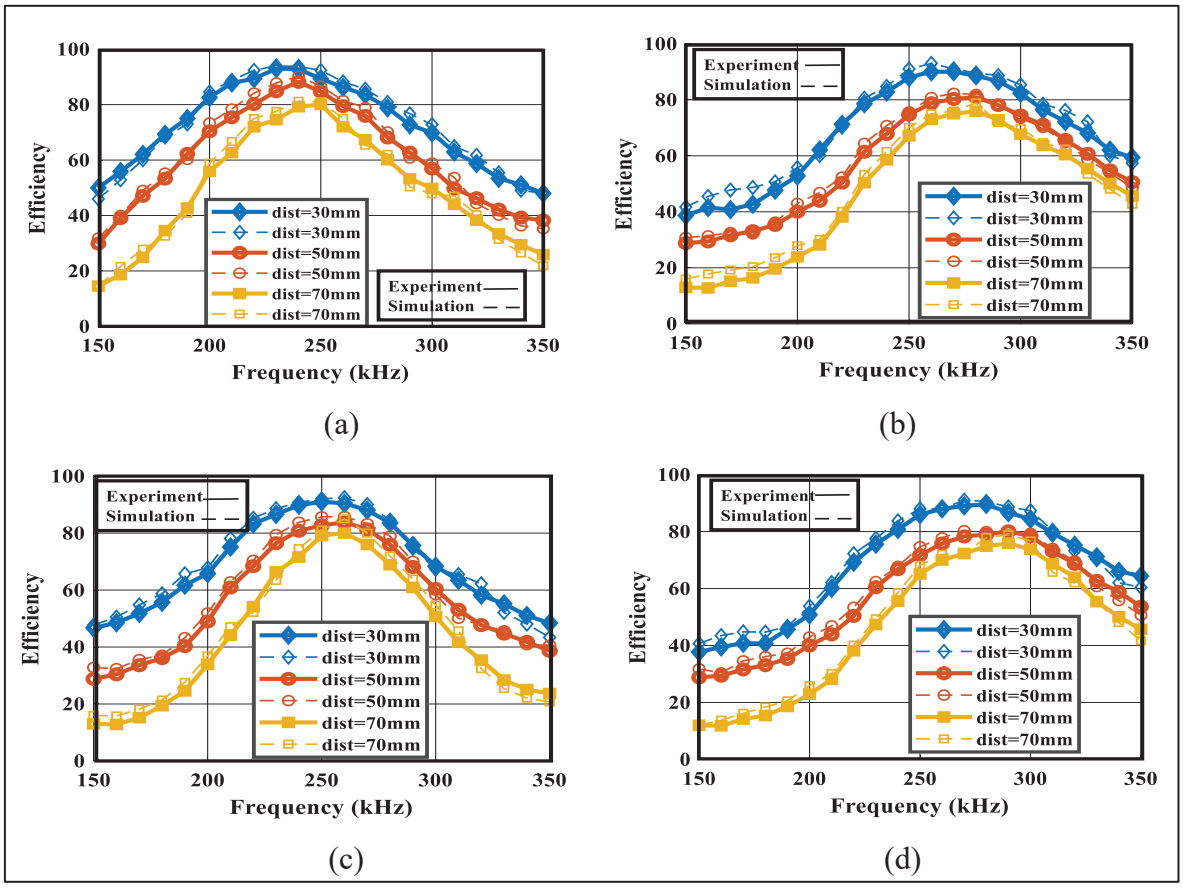

Figure 3.14 Experimental measurement and simulation results of the efficiency at different frequencies when the distance is 30mm,50mm, and 70mm. (a) Square coils, (b) Circular coils, (c) Octagonal coils, (d) Hexagonal coils

Figure 3.15 illustrates the power and efficiency of four different coil geometries square, circle, octagonal, and hexagonal across various vertical transmission distances. In Figure 3.15(a), square coils consistently achieve the highest efficiency at all distances, making them the most reliable choice for applications requiring optimal efficiency over varying transmission distances. Octagonal and circular coils exhibit competitive performance, especially at mid-range distances. Although hexagonal coils have the lowest initial efficiency, they maintain a steady performance trend as the distance increases. Overall, square coils demonstrate superior efficiency, followed by octagonal, circular, and hexagonal coils. Figure 3.15(b) shows the maximum power output for each coil type: square coils achieve 140.8 W at 100 mm, circle

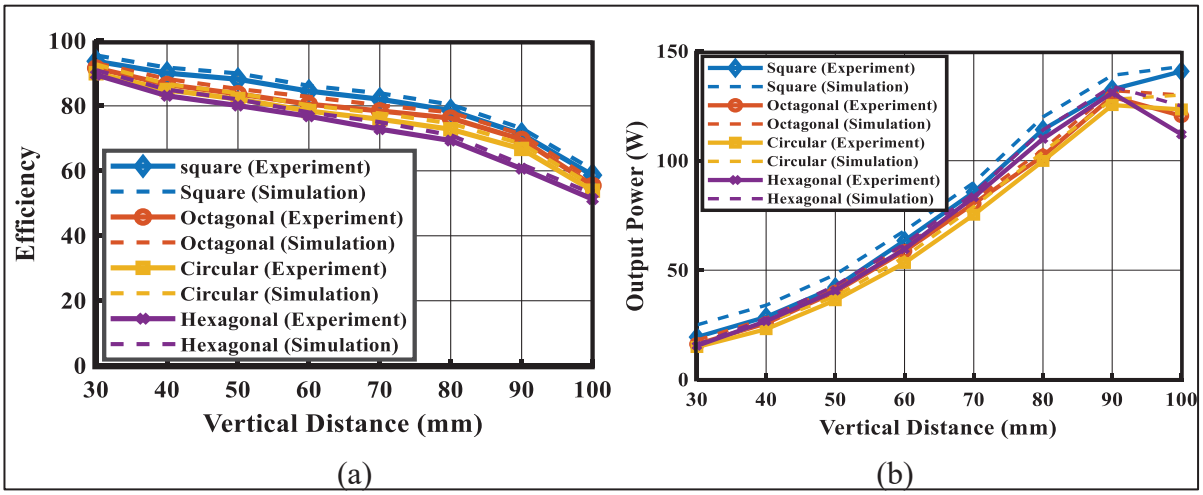

Figure 3.15 Experimental measurement and simulation results of the efficiency and output at different distances, when load is 30 Ω

coils reach 129.14 W, octagonal coils deliver 125 W, and hexagonal coils produce 131 W at 90 mm. These results, obtained through both experimental and simulation methods, confirm the overall trends observed in the study.

Figure 3.16 shows the steady-state voltage and current waveforms for the transmitter and receiver coils, measured with a 30 Ω load, a transmission distance of 70 mm, and an input DC voltage of 80 V. The operating frequency is adjusted to the self-resonant frequency of each coil. Accurate power measurement requires precise calibration of the gating settings. The data obtained from these measurements are used to compute received power and transmission efficiencies, as summarized in Table 3.5. Thermal testing of the WPT system was performed on a flat surface platform at an output power of 80 W. Figure 3.17, featuring data from the FLIR ETS320 thermal camera, displays the temperature distribution across the system. The highest temperature recorded was 32.4 °C in the hexagonal coil, specifically at the edge of the inner turn of the self-resonant coils. Among the various coil configurations tested, the square core demonstrated the lowest operating temperature.

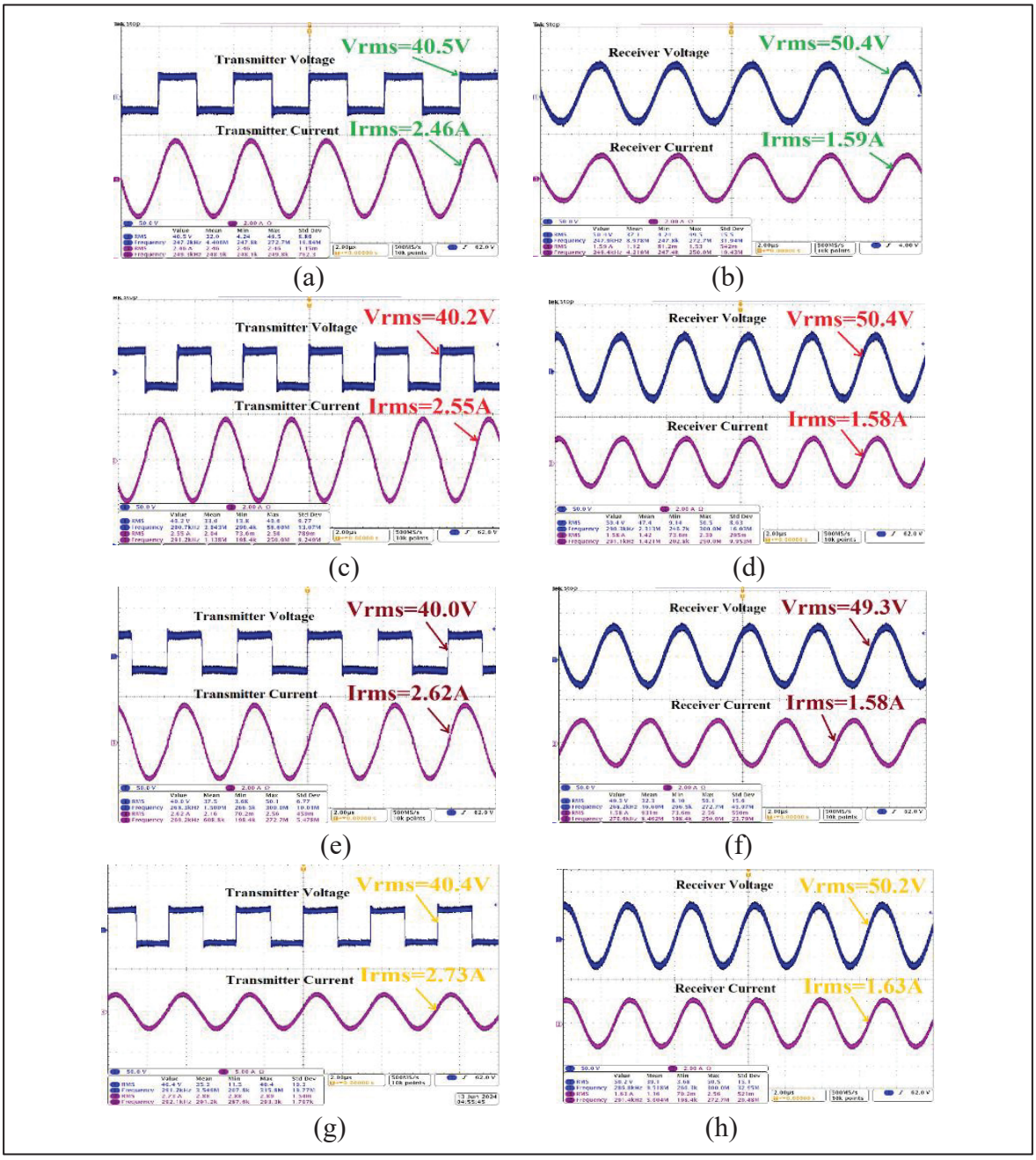

Figure 3.16 Steady state voltage and current waveforms when distance is 70mm. (a) Transmitter voltage and current of square coil, (b) Receiver voltage and current of circle coil, (c) Transmitter voltage and current of circle coil, (d) Receiver voltage and current of circle coil, (e) Transmitter voltage and current of octagonal coil, (f) Receiver voltage and current of octagonal coil, (g) Transmitter voltage and current of hexagonal coil, (h) Receiver voltage and current of hexagonal coil

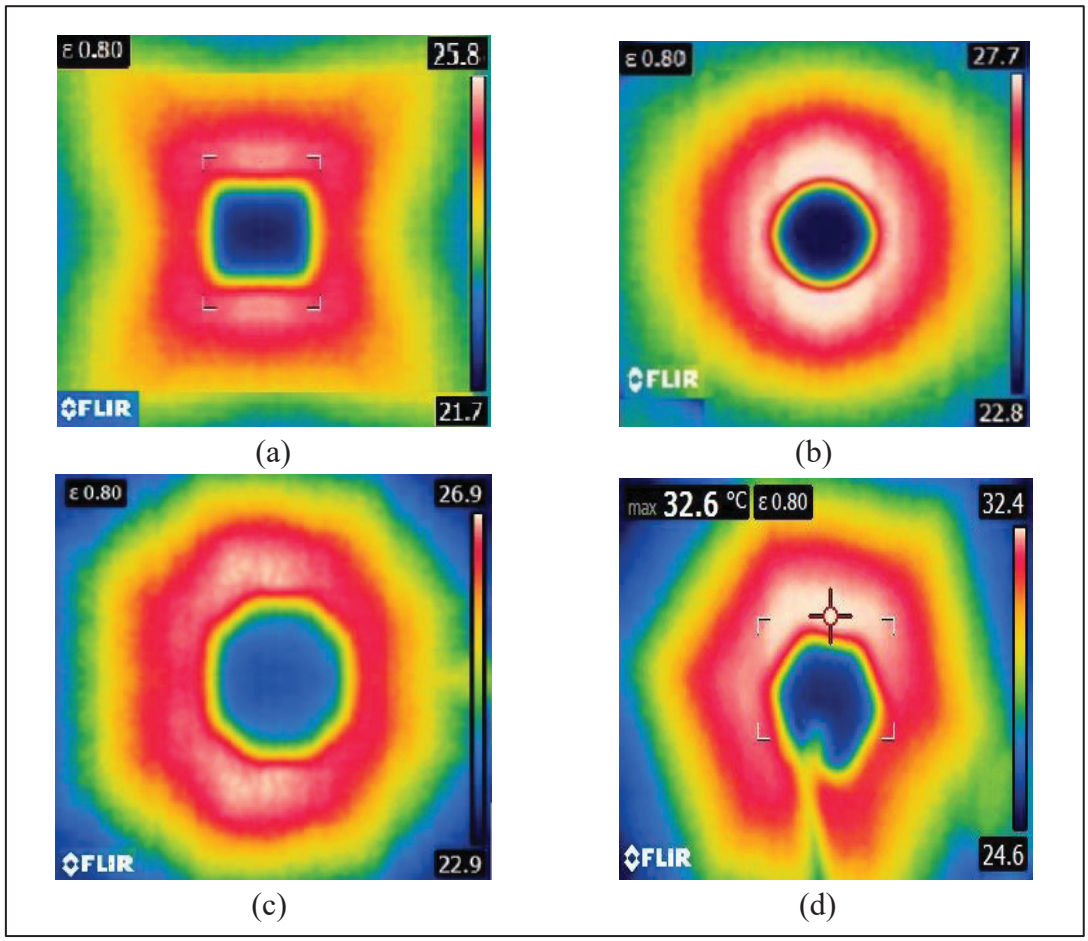

Figure 3.17 Thermal camera images of different coils. (a) Square coils, (b) Circle coils, (c) Octagonal coils, (d) Hexagonal coils

Table 3.5 Comparison of different coil geometries

Parameter	|Square	Circle	Octagonal	Hexagonal
Inductance (uH)	38.87	34.96	39.14	33.016
Capacitance (nF)	12.1	9.51	10.03	9.06
Resistance (mohm)	1050	1287	1160	1310
Resonant Frequency (kHz)	235	276	254	291
Coupling coefficient (k)	0.7294	0.7224	0.7070	0.7042
Maximum power (W)	80.136	78.62	77.894	82.3
Maximum Efficiency	93	90.04	91.04	89.57
Quality Factor	54.63	47.08	53.82	46.058

3.5 Conclusion

This study investigates the performance of four coil geometries, circle, square, hexagonal, and octagonal for self-resonant wireless power transfer (SRWPT) systems, highlighting the importance of self-resonance in eliminating external capacitors and improving system efficiency. The geometries were optimized, and innovative TWR and TGR structures were introduced to reduce losses and enhance the quality factor. Simulations and experiments showed that the square coil, due to its extended conductor length, exhibited the highest inductance and inter-capacitance, resulting in the lowest resonant frequency. Circular and square coils achieved better coupling and efficiency, while hexagonal and square coils transferred higher power. Additionally, square and octagonal coils performed better under misalignment conditions. These findings demonstrate the practical advantages of different coil geometries in balancing efficiency, power transfer, and misalignment tolerance, offering valuable insights for designing optimized SRWPT systems and guiding future exploration of new geometries and design refinements.

CHAPTER 4

EFFICIENT HIGH EFFICIENCY SELF-RESONANT THREE-COIL WIRELESS POWER TRANSFER SYSTEM FOR BIMEDICAL IMPLANTS

Neda Zahedi Saadabad [a], Javad Nekoui, Qingsong Wang [a], Ambrish Chandra [a]

[a] Department of Electrical Engineering, École de technologie supérieure,
1100 Notre-Dame Ouest, Montréal, Québec, Canada H3C1K3

This article is submitted to the *IEEE Journal of Emerging and Selected Topics in Industrial Electronics (JESTIE) in February 2026.*

Abstract

Self-Resonant Wireless Power Transfer (SWPT) systems eliminate external compensation components by exploiting the intrinsic parasitic properties of planar coils, making them attractive for compact receiver designs. This paper proposes a self-resonant three-coil WPT architecture that enables high inductance generation and efficient power transfer within a limited receiver footprint. The receiver is implemented using two interconnected double-layer PCB coils, enabling a substantial increase in effective inductance without enlarging the coil area. An auxiliary resonant path is formed using the inherent inductive (L_m) and capacitive (C_m) properties of the coil structure, resulting in enhanced impedance characteristics and improved power transfer robustness. On the transmitter side, an air-gap configuration is employed to allow flexible resonance tuning through coil spacing while reducing dielectric losses associated with conventional substrates. The proposed system is systematically evaluated and compared with conventional self-resonant three-coil and self-resonant two-coil configurations under identical operating conditions. Comprehensive simulation and experimental results show that the proposed architecture achieves a peak efficiency of 92%, compared to 73% for a conventional self-resonant three-coil system, along with a voltage gain of 25.1 and an output power of 360 mW, while maintaining a compact, capacitor-free receiver structure.

4.1 Introduction

Advances in microelectronics, system integration, and biocompatible materials have enabled the rapid development of implantable medical devices for monitoring and therapeutic applications. However, providing a reliable and long-term power supply remains a fundamental challenge, as conventional batteries increase device size and require surgical replacement. Wireless power transfer (WPT) has therefore emerged as a key enabling technology, enabling non-invasive energy delivery and supporting the practical implementation of implantable biomedical devices (Lee, Kim, Kang, Song & Lee, 2024; Ha-Van, Tretyakov & Simovski, 2025; ESSA Amine et al., 2025).

WPT systems are commonly implemented using inductively coupled coils, where capacitive compensation is required to cancel inductive reactance and suppress reactive power that does not contribute to useful energy transfer. Resonant operation improves the system power factor and enables efficient power delivery to the load (Zahedi, Wang & Chandra, 2023) (Zahedi, Wang & Chandra,, 2025). To further enhance coupling strength, load tolerance, and misalignment robustness, impedance matching techniques (Xu et al., 2024; Weng et al., 2025), and multi-coil configurations have been widely investigated (Guan, Qiao, Mai, Wang & Xu, 2025; Schelles et al., 2025). In particular, three-coil WPT architectures have demonstrated advantages over conventional two-coil systems, including improved misalignment tolerance, enhanced power transfer capability, and reduced electromagnetic field exposure in biological tissue (Fang, Zhong & Lu, 2024; Munsi, Pradhan & Aditya, 2025).

In biomedical applications, however, these approaches are subject to strict constraints on system size, safety, and long-term operation. Conventional WPT architectures rely on external lumped capacitors to achieve resonance and matching, which increase circuit complexity and are subjected to high voltage and current stress under high-Q operation, limiting their suitability for compact implantable systems (Chakibanda & Komanapalli, 2024; Park Yechan et al., 2025; Moisello, Liotta, Malcovati & Bonizzoni, 2023). Self-resonant coils address these limitations by achieving resonance through the inherent interaction between coil inductance

and distributed parasitic capacitance, thereby eliminating the need for external compensation components (Zahedi, Wang & Chandra, 2025; Zahedi, Wang & Chandra, 2023; Li Yong et al., 2026; Wu, Jiao, Cai, Yu & Ren, 2025). This intrinsic resonance mechanism simplifies the system structure and avoids the voltage and current stress associated with discrete capacitors. Consequently, self-resonant WPT systems enable compact and highly integrated implementations and are well suited for biomedical implants operating under stringent constraints on size, safety, and long-term reliability (Zahedi, Nekoui, Dehbozorgi, Wang & Chandra, 2025).

This paper presents a compact self-resonant three-coil PCB-based WPT system designed to enhance efficiency while maintaining a reduced receiver (RX) coil size. Efficient load matching and resonance control are achieved through three independent design degrees of freedom: optimization of the relative voltage polarity between the RX coils, exploitation of mutual inductance and mutual capacitance within a self-resonant structure to eliminate external compensation components and enhance reflected impedance, and precise tuning of the operating frequency by adjusting the air gap between the transmitter coils. The proposed self-resonant architecture reduces system complexity and supports highly integrated implementations suitable for implantable applications. A comprehensive performance comparison with a self-resonant three-coil system and a self-resonant two-coil configuration demonstrates that the proposed design achieves superior impedance matching and higher power transfer efficiency, resulting in improved overall system performance. The structure of this paper is as follows. Section II provides an overview of conventional three-coil WPT configurations. Section III presents an enhanced system architecture for compact receiver design. The design procedures for the TX and RX coils are presented in Section IV, while Section V reports the corresponding simulation results. Finally, Section VI presents the experimental validation and summarizes the main conclusions of the study.

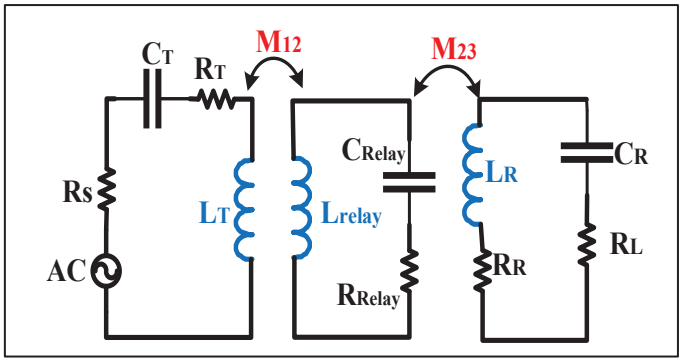

Figure 4.1 Traditional Three-Coil WPT Layout

4.2 Operating Principal of Conventional Three-Coil WPT System

In WPT systems, energy is transferred through three magnetically coupled resonators arranged between the source and the load. Compared with a conventional two-coil system, the additional resonant coil enhances magnetic coupling and improves power transfer robustness under variations in load resistance and coupling conditions. As shown in Fig. 1, the transmitter (TX) coil is driven by an AC source, while two coupled coils are located on the receiving side, where the intermediate coil acts as a resonant link that facilitates energy transfer to the load-connected receiver (RX) coil. Efficient operation requires all resonators to be tuned to the same operating frequency, which is typically achieved using capacitive compensation to cancel inductive reactance, establish resonance, and minimize reactive power circulation. For resonant operation, the angular frequency ω must satisfy the following condition for each coil:

$$\frac{1}{jwC_T} = jwL_T \ , \quad \frac{1}{jwC_{Relay}} = jwL_{Relay} \ , \quad \frac{1}{jwC_R} = jwL_R \tag{4.1}$$

Where L_T, L_{Relay}, L_R, C_T, C_{relay}, and C_R denote the self-inductance and compensation capacitance of the TX, relay, and RX coils, respectively. To analyze the system behavior, Kirchhoff's Voltage Law (KVL) is applied to the coupled circuit, resulting in an impedance matrix representation. Based on reflected impedance theory (Kiani & Ghovanloo, 2012), the

presence of the relay and receiver coils introduces reflected impedances into the preceding stages. The reflected impedance seen by the TX coil due to the relay coil and that seen by the relay coil due to the RX coil are expressed as

$$Z_{ref1} = \frac{w^2 M_{TX.\mathrm{Re}lay}^2}{R_{\mathrm{Re}lay} + Z_{ref2}}, \quad Z_{ref2} = \frac{w^2 M_{\mathrm{Re}lay.RX}^2}{R_{\mathrm{R}} + R_L} \tag{4.2}$$

Where $M_{TX.Relay}$ and $M_{relay.RX}$ are the mutual inductances between adjacent coils. The power transfer efficiency of the three-coil WPT system can then be derived as

$$\eta = \frac{Z_{ref1}}{R_T + Z_{ref1}} \frac{Z_{ref2}}{R_{\mathrm{Re}lay} + Z_{ref2}} \frac{R_L}{R_R + R_L} \tag{4.3}$$

Where R_T, R_{Relay}, and R_R are the parasitic resistances of the TX, relay, and RX coils, respectively, and R_L denotes the load resistance. Alternatively, the overall efficiency can be expressed as the product of the efficiencies of individual stages:

$$\eta = \eta_T \times \eta_{Relay} \times \eta_R \tag{4.4}$$

Where η_T corresponds to the transmitter efficiency and $\eta_{Relay} \times \eta_R$ represents the efficiency of the receiver sections.

4.3 Operating Efficiency Enhancement Strategy for Compact Receiver Designs

In implantable WPT systems, the RX coil is subject to strict size constraints. Reducing the RX dimensions decreases its self-inductance (L_{relay}, L_R) and weakens the mutual coupling with adjacent coils (M_{23}), which directly reduces the reflected impedance from the receiver stage (Z_{ref2}). As the reflected impedance diminishes, the relay coil becomes less effective in transferring power, resulting in increased losses on the receiver side. Meanwhile, the reflected impedance observed at the TX either increases or saturates, depending on the extent of RX size

reduction. As a result, the relay stage becomes the dominant efficiency bottleneck, causing both the power transfer efficiency and the power delivered to the load to decrease as the RX coil size shrinks. To address this challenge, this paper proposes a method to enhance the receiver-side reflected impedance while preserving fully self-resonant operation across all coils. This approach enables efficient power transfer even with compact receiver coils, making it well suited for implantable WPT applications.

An effective way to mitigate efficiency degradation caused by receiver miniaturization is to enhance the receiver-side reflected impedance Z_{ref2} by strengthening the interaction between the relay and receiver coils. This is achieved by modifying the resonance condition of the three-coil system. Instead of the conventional resonance criterion in (1), an alternative tuning strategy is adopted, as defined in (5). Although the physical coil arrangement remains unchanged (Fig. 1), this modification leads to a different equivalent circuit representation (Fig. 2). The proposed resonance condition is established by introducing an additional coupling capacitor C_m, and inductance L_m which participates in forming resonance at the receiver coils. The resulting resonance conditions are expressed as

$$\frac{1}{jwC_1} = jwL_1 \ , \quad \frac{1}{jwC_m} + \frac{1}{jwC_2} + jwL_m = jwL_2$$
$$\frac{1}{jwC_m} + \frac{1}{jwC_3} + jwL_m = jwL_3 \tag{4.5}$$

The impact of this modification is evaluated using impedance matrix analysis. Compared with the conventional three-coil model, the impedance matrix of the proposed system includes the contribution of C_m and L_m which alters the coupling between the relay and receiver coils. From the determinant of the impedance matrix, the reflected impedances of the modified system are obtained as

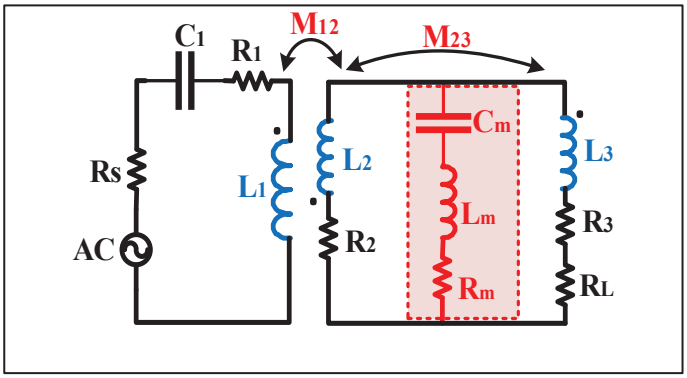

Figure 4.2 Proposed Three-Coil WPT Configuration

$$Z_{ref1-p} = \frac{w^2 L_{12}^2}{R_2 + \left[(wL_{23} + wL_m + \frac{1}{wC_m})^2 \Big/ (R_3 + R_L) \right]} \tag{5.6}$$

$$Z_{ref2-p} = (wL_{23} + wL_m + \frac{1}{wC_m})^2 \Big/ (R_3 + R_L) \tag{5.7}$$

These expressions indicate that the added capacitive and inductive coupling effectively increases the interaction between the relay and receiver coils, which can be interpreted as an enhancement of the equivalent mutual inductance

$$jwL_{23} \rightarrow j(wL_{23} + wL_m + \frac{1}{wC_m}) \tag{5.8}$$

Since receiver size reduction leads to a decrease in Z_{ref2}, the proposed resonance adjustment compensates for this effect by increasing Z_{ref2p}, thereby improving both power transfer efficiency and power delivered to the load. Observations on the proposed three-coil system are:

- For $R_L \gg R_3$, the RX efficiency η_{RX} approaches unity, indicating minimal dissipation in the load coil. However, losses in the implanted secondary coil may still remain significant. $R_L \gg R_3$ and $Z_{ref2P} > R_2$ are two requirements to reduce losses in the RX coils.

- Although C_m and L_m improve receiver-side coupling, they reduce the transmitter-side reflected impedance Z_{ref1p}, leading to a decrease in η_{TXp} . This trade-off highlights the need for careful transmitter optimization.

- Unlike conventional three-coil systems, the proposed architecture allows all receiver-side coil impedances to jointly contribute to the reflected impedance, enhancing both power transfer efficiency and power delivered to the load while enabling receiver miniaturization. The resulting reflected impedance is

$$R_{ref2p} = (w^2 L_{23}^2 + \frac{1}{w^2 C_m^2} + w^2 L_2 L_{23}^2 + w^2 L_3 L_{23}^2) / (R_3 + R_L) \tag{5.9}$$

- The reflected impedance is polarity-dependent. Reversing the coil orientation reduces Z_{ref2p}, negating the intended enhancement. In this case

$$R_{ref2p} = (wL_{23} - \frac{1}{wC_m})^2 / (R_3 + R_L) \tag{5.10}$$

Based on these observations, the proposed approach incorporates two complementary strategies to enhance receiver-side efficiency and an additional method to improve transmitter performance, which are discussed in detail in the following sections.

4.3.1 Compact RX Inductance Optimization Using Equal Coil Splitting (L_2=L_3)

In implantable three-coil WPT systems, receiver performance is constrained by the limited allowable coil size. Reducing the receiver dimensions inherently decreases both inductance and magnetic coupling. Since increasing the coil size is not feasible under implantable constraints, performance enhancement must instead rely on how inductance is distributed among the receiver coils. Proper inductance allocation and equal coil diameters strengthen

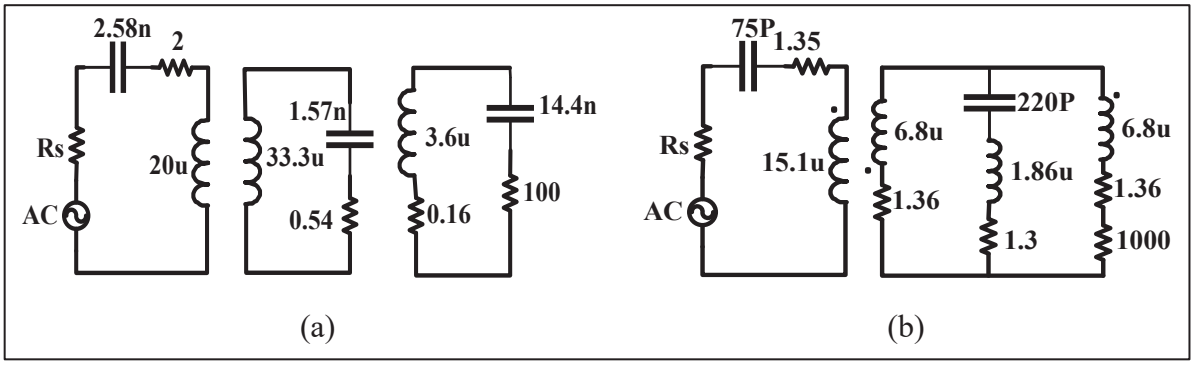

Figure 4.3 (a) Conventional three-coil RX configuration adopted from Ram Rakhyani, Mirabbasi & Chiao (2010). (b) Proposed three-coil RX configuration employing L_2=L_3 and $(1/\omega C_2)=(1/\omega C_3)=0$ to maximize the receive-side reflected impedance

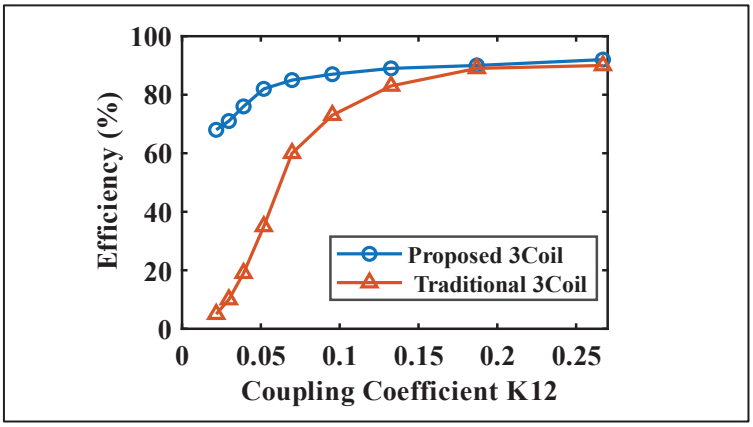

Figure 4.4. Efficiency comparison between a reference three-coil system in Ram Rakhyani, Mirabbasi & Chiao (2010), and the proposed compact receiver design

mutual coupling and improve system performance. This approach maximizes the RX-side reflected impedance, without increasing the implant footprint.

$$L_2 + L_3 = L_{\max} \tag{4.11}$$

$$Z_{ref\,2\_\max} = \frac{w^2 L_{23}^2}{R_3 + R_L} = \frac{w^2 K_{23}^2 L_2 L_3}{R_3 + R_L} \tag{4.12}$$

To maximize Z_{ref2}, the ideal configuration is:

$$L_2 = L_3 = L_{\max}/2 \tag{4.13}$$

The implanted receiver configuration reported in (Ram Rakhyani, Mirabbasi & Chiao, 2010) and the proposed compact receiver are illustrated in Fig. 3 (a) and (b) for direct comparison. In addition, Fig. 4 presents the corresponding efficiency and coupling characteristics of both systems. While the design in [21], relies on larger inductances and longer conductor length, the proposed receiver achieves comparable efficiency with significantly reduced inductance values. This performance is enabled by maximizing the RX-side reflected impedance through the condition L_2=L_3 and the use of the mutual coupling capacitor C_m and inductance L_m.

4.3.2 Capacitive Balancing for Improved Receiver Efficiency [$(1/\omega C_2)=(1/\omega C_3)=0$]

Beyond geometric constraints, the receiver efficiency is fundamentally determined by the resonance behavior of the implanted coils. In conventional three-coil systems, the receiver efficiency is governed by (2), whereas the proposed architecture introduces a modified resonance condition, resulting in the efficiency expression in (6) and (7). By suppressing reactive power circulation through increasing $1/(\omega C_m)$, the resonance condition in (2) enforces $1/(\omega C_2)=1/(\omega C_3)=0$, enabling the receiver section to operate at its maximum efficiency.

$$\eta_{RX} = \left[\left(\frac{w^2 L_{23}^2}{R_3 + R_L}\right) \Big/ \left(R_2 + \frac{w^2 L_{23}^2}{R_3 + R_L}\right)\right] . \frac{R_L}{R_3 + R_L} \tag{5.14}$$

$$\eta_{RX} = \left[\left(\frac{(wL_{23} + wL_m + \frac{1}{wC_m})^2}{R_3 + R_L}\right) \Big/ \frac{(wL_{23} + wL_m + \frac{1}{wC_m})^2}{R_3 + R_L}\right] . \frac{R_L}{R_3 + R_L} \tag{5.15}$$

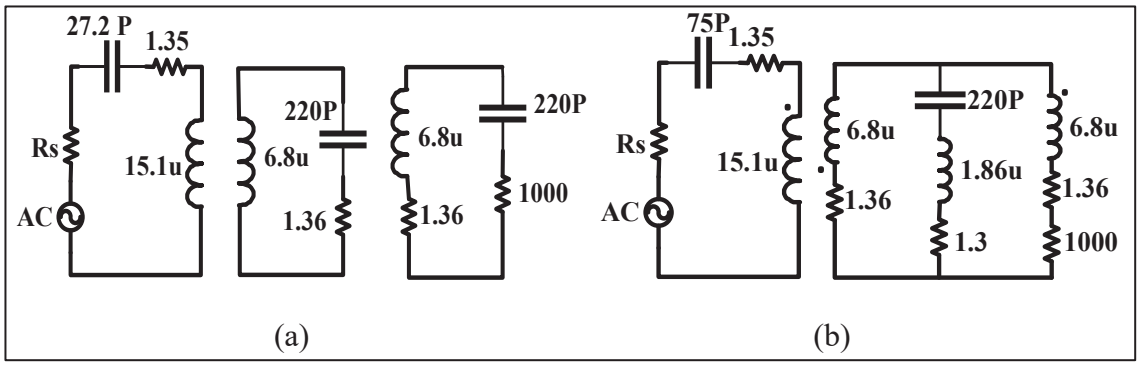

Figure 4.5 (a) Conventional self-resonant three-coil RX configuration with L_2=L_3. (b) Proposed three-coil RX configuration employing L_2=L_3 and $(1/\omega C_2)$=$(1/\omega C_3)$=0

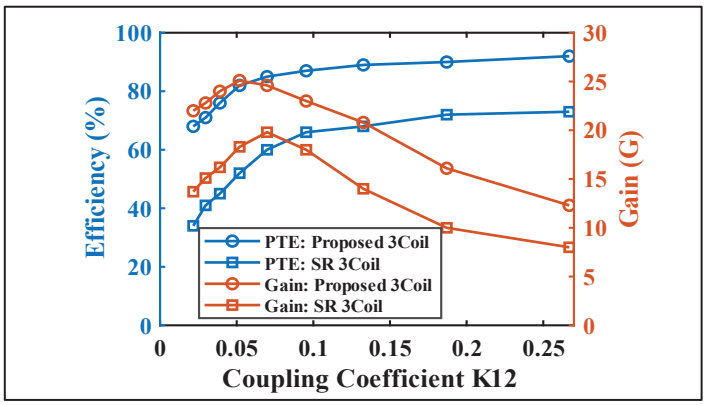

Figure 4.6 Efficiency and gain comparison between a conventional self-resonant three-coil system, and the proposed compact receiver design

As a second evaluation case, as shown in Fig. 5 a conventional self-resonant three-coil system employing distributed capacitors C_2 and C_3 with L_2=L_3 is considered. For a fair comparison, both systems are evaluated under identical coil geometries, load, and transmitter conditions. While the baseline configuration achieves resonance using local capacitive compensation, the proposed architecture removes C_2 and C_3 and instead realizes resonance through the combined effect of mutual capacitance C_m and mutual inductance L_m. Under these identical conditions, the proposed system attains a receiver efficiency of approximately 92%, compared to about 73% for the conventional design. As shown in Fig. 6, this improvement becomes more pronounced at higher coupling coefficients k_{12}, demonstrating that the enhanced performance originates from the mutual capacitive and inductive coupling introduced at the receiver side.

4.3.3 Transmitter Optimization Strategy for Improved Power Transfer

Increasing the RX-side reflected impedance improves the RX efficiency; however, due to the coupling between the TX and RX coils, this increase simultaneously modifies the effective loading seen by the TX and can adversely affect transmitter efficiency. To ensure balanced system performance, the proposed design regulates the current distribution within the coupled coils. Specifically, reducing the current ratios I_{1p}/I_{3p} and I_{2p}/I_{3p}, defined in (16) and (17), simultaneously improves both transmitter and receiver efficiencies.

$$\frac{I_{1-p}}{I_{3-p}} = \frac{R_2(R_3 + R_L) + (wM_{23} + wL_m + \frac{1}{wC_m})^2}{wM_{12}(wM_{23} + wL_m + \frac{1}{wC_m})} \tag{4.16}$$

$$\frac{I_{2-p}}{I_{3-p}} = \frac{(R_3 + R_L)}{jw(M_{23} + L_m) + \frac{1}{jwC_m}} \tag{4.17}$$

When the condition $R_2(R_L+R_3)=2\omega^2M_{23}^2$ is satisfied, the transmitter efficiency becomes insensitive to variations in mutual inductance. This balance is achieved by introducing a conductive link between the receiver coils, forming mutual capacitance C_m and mutual inductance L_m, which enhance coupling without increasing the implant size. A compact RX system with limited mutual coupling is analyzed to demonstrate the proposed method, showing that RX efficiency can be improved without compromising TX performance. The system is evaluated at an operating frequency of 4.68 MHz with R_L=1 kΩ, R_1=1.35 Ω, and R_2=R_3=1.36 Ω. The inductances are selected as L_1=15.1 μH and L_2=L_3=6.83 μH. These parameters satisfy the design conditions considered in this study, namely L_2=L_3, $R_L \gg R_3$, and $R_2(R_L+R_3)=2\omega^2M_{23}^2$. By applying the proposed self-resonant condition, the current

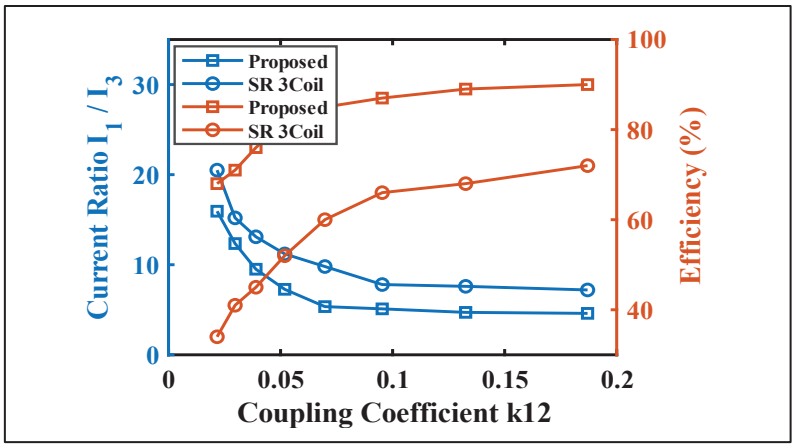

Figure 4.7 The proposed design lowers $I_{2\text{-}p}/I_{3\text{-}p}$ to 5.9 from 13.3 in the self-resonant conventional system, improving receiver performance without affecting transmitter efficiency

distribution within the receiver section is modified, leading to a reduction in the ratio I_{2p}/I_{3p} while keeping I_{1p}/I_{3p} nearly unchanged. As a result, the receiver efficiency is significantly enhanced without degrading the transmitter efficiency, as confirmed by the simulation results presented in Fig. 7.

4.3.4 Load-Independent RX Behavior

In practical WPT systems, a stable receiver performance under load mismatch is highly desirable. In the proposed structure, this stability is achieved by shaping the effective coupling seen by the receiver rather than relying on low-loss relay coils. As a result, variations in load resistance produce only minor changes in RX efficiency. For a conventional three-coil configuration, the RX efficiency strongly depends on the product of magnetic coupling and relay resistance, leading to noticeable efficiency degradation as the load varies. This dependence is captured by

$$\frac{\partial(\eta_{RX\_SR})}{\partial R_L} = \frac{-\omega^2 M_{23}^2 R_2}{(\omega^2 M_{23}^2 + R_2 R_L)^2} \tag{4.18}$$

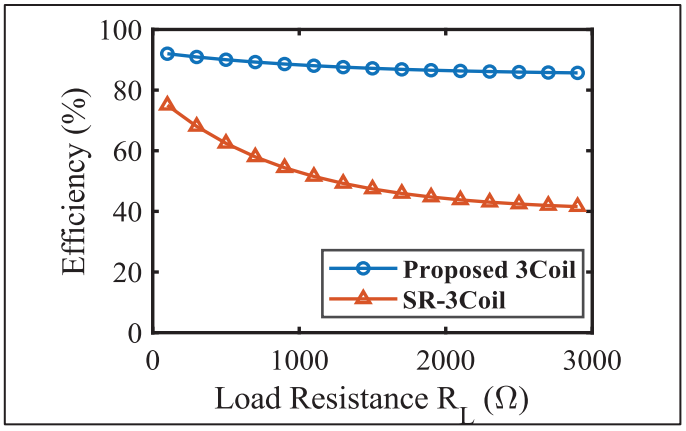

Figure 4.8 Impact of load variations on efficiency

In contrast, the proposed system introduces an additional coupling path (C_m-L_m), which effectively strengthens the interaction between the receiver coils. Consequently, the RX sensitivity to load changes follows as

$$\frac{\partial(\eta_{RX\_proposed})}{\partial R_L} = \frac{-(\omega M_{23} + 1/\omega C_m)^2 R_2}{((\omega M_{23} + 1/\omega C_m)^2 + R_2 R_L)^2} \tag{4.19}$$

This enhanced coupling reduces the rate at which efficiency changes with load resistance, yielding a more load-tolerant RX response. The resulting improvement in efficiency stability is illustrated in Fig.8.

4.3.5 RX Current Redistribution

4.3.5.1 Reduction of the intermediate-coil current I_2

In three-coil WPT systems, losses in the implanted section are strongly influenced by the current flowing through the intermediate RX coil. For a given load condition, lowering this current directly reduces conduction losses. As demonstrated in Fig. 9, the proposed architecture

decreases the required intermediate-coil current by increasing the effective mutual impedance between the implanted coils. For V_{in}=1.5, the intermediate-coil currents in the conventional and proposed systems are given by

$$I_2 = \frac{j\omega M_{12}(R_3 + R_L)}{R_1 R_2 (R_3 + R_L) + \omega^2 M_{23}^2 R_1 + \omega^2 M_{12}^2 (R_3 + R_L)} \tag{4.20}$$

$$I_{2p} = \frac{j\omega M_{12}(R_3 + R_L)}{R_1 R_2 (R_3 + R_L) + (\omega M_{23} + 1/\omega C_m)^2 R_1 + \omega^2 M_{12}^2 (R_3 + R_L)} \tag{4.21}$$

At higher TX–RX coupling levels k_{12}, the terms associated with ωM_{12} dominate, causing I_2 and I_{2p} to converge. At lower k_{12}, however, the increased mutual impedance introduced by L_m-C_m results in I_{2p}<I_2 for the same operating condition.

4.3.5.2 Increase of load current I_3

The effect of current redistribution becomes more evident when examining the load current. The load currents in the conventional and proposed systems can be expressed as

$$I_3 = \frac{I_2(j\omega M_{23})}{R_{3t}}, \quad I_{3P} = \frac{I_{2p}(j\omega M_{23} + 1/j\omega C_m)}{R_{3t}} \tag{4.22}$$

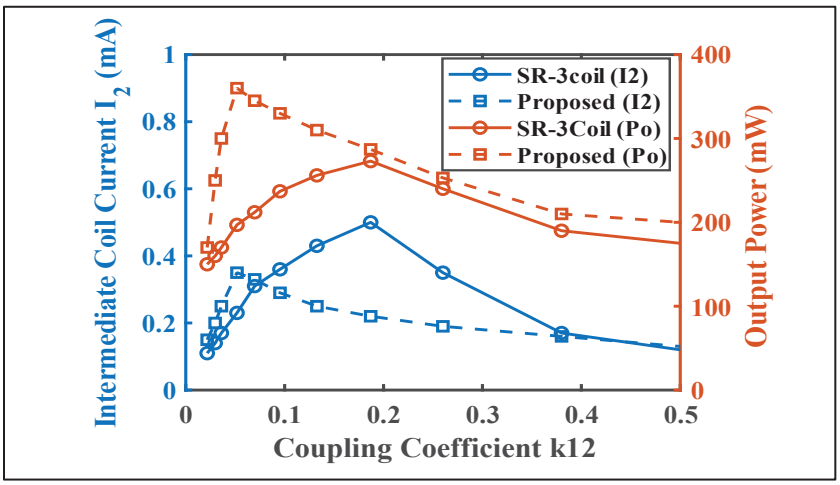

Figure 4.9. Comparison of output power and secondary coil current in conventional and proposed three Coil systems

These expressions indicate that, for a given intermediate-coil current, the proposed system delivers a higher load current ($I_{3p}>I_3$). Equivalently, to achieve the same power delivered to the load, the proposed architecture requires a smaller intermediate-coil current. As shown in Fig. 9, this leads to higher PDL and reduced losses in the implanted coils. The maximum PDL occurs when the reflected impedance equals the TX resistance, and in the proposed system this maximum is higher and appears at a slightly larger k_{12}, which is also influenced by the chosen coil polarity.

4.4 Operating Design Considerations for Transmitter And Receiver Coils

4.4.1 Design of the Receiver Coil

The proposed stacked PCB coil structure, in which three circular spiral windings are fabricated on separate PCB layers and electrically isolated by a thin dielectric spacer is shown in Fig.10 (a) Each winding layer provides two terminals: one terminal pair is internally short circuited, while the remaining terminals are used for external electrical connections. When the internal terminals are shorted, the two windings behave as a strongly magnetically coupled pair. Under this configuration, the equivalent inductance for each coil can be expressed as $L=L_1+L_2+2M$, where M denotes the mutual inductance between the two layers. With this electrical connection, due to the thin dielectric layer, the proposed structure effectively achieves an approximately fourfold increase in inductance within the same physical footprint. At the same time, the interlayer parasitic capacitance is inherently suppressed to a negligible value ($C\approx0$). Consequently, both a significant inductance enhancement and the elimination of interlayer capacitance are realized simultaneously using a single compact coil structure. This configuration therefore satisfies the second key condition for maximizing the receiver side power transfer efficiency. The same stacked-coil configuration is applied to coil L_3. Owing to the symmetric design of the system, the condition $L_2=L_3$ is inherently fulfilled, thereby satisfying the first required condition for achieving maximum system efficiency.

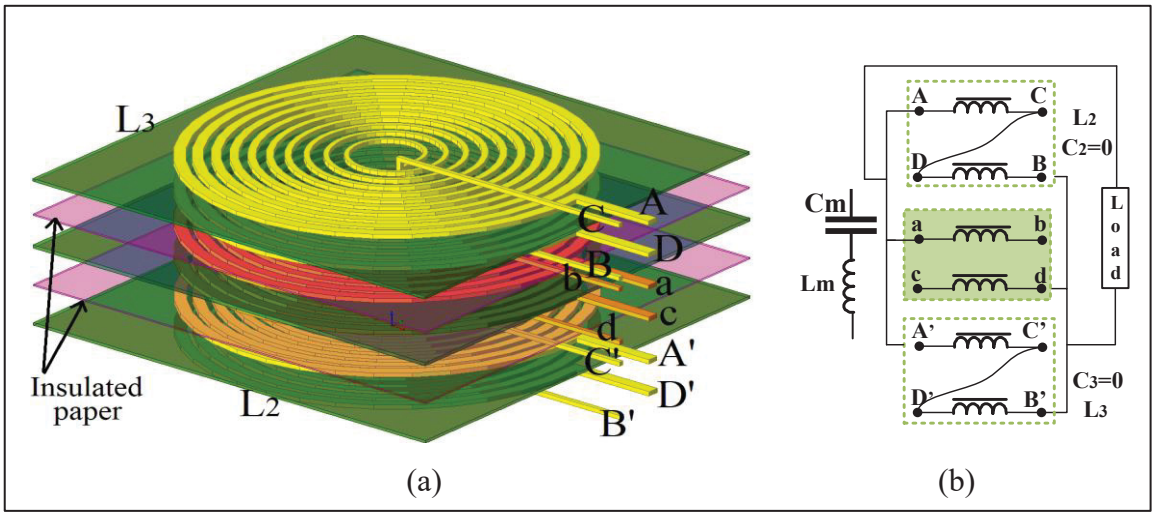

Figure 4.10 (a) Receiver coil structure based on three double-layer circular coils, (b) simplified equivalent circuit representation

A supplementary double-layer coil with a thinner dielectric layer is inserted between L_2 and L_3 to increase the effective system impedance. In this intermediate coil, the reduced dielectric thickness is intentionally employed to establish capacitive coupling between the upper and lower windings. Terminals b and c are left open, whereas terminals a and d are connected to terminals A and B′, respectively. This connection forces the alternating current to interact with both winding layers through the dielectric interface, causing the structure to operate as an intrinsic series-resonant element. The resonance condition is defined by the equivalent inductance L_m and the internally generated capacitance C_m, as illustrated in Fig. 10 (b). Impedance enhancement is achieved with proper polarity alignment, whereas polarity reversal causes flux cancellation and impedance reduction (Fig. 2).

To improve high-frequency performance, the spiral geometry of the proposed coil is intentionally designed to be non-uniform. Rather than maintaining constant conductor dimensions, the trace width is gradually increased toward the outer turns of the coil, while the spacing between adjacent turns is progressively reduced. This geometric shaping is described using the Track Width Ratio (TWR) and Track Gap Ratio (TGR), as defined in (16).

$$W_n = a_{TWR}^{n-1} W \ , \ G = a_{TWR-TGR}^{n-1} G_n \tag{4.23}$$

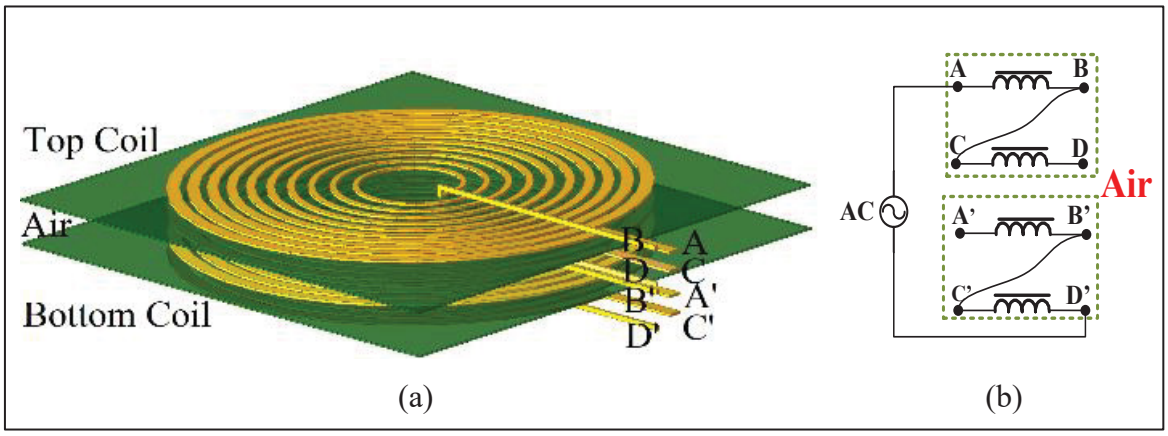

Figure 4.11 (a) Transmitter coil structure based on two double-layer circular coils with air distance, (b) simplified equivalent circuit representation

Where, n denotes the turn index measured from the outermost turn, and α controls the degree of geometric variation along the spiral. This gradual redistribution of conductor dimensions mitigates current crowding in regions exposed to stronger magnetic fields near the coil center. As a result, the effective AC resistance is lowered, which directly contributes to reduced conduction losses and improved efficiency.

4.4.2 Design of the Transmitter Coil

Fig. 11 depicts the transmitter coil, which is formed by two spatially separated double-layer PCB coils. In each PCB coil, an internal shorting connection is applied to increase the effective inductance. Specifically, terminals B and C are shorted in the upper coil, resulting in an equivalent inductance of $L_{top}=L_1+L_2+2M$. The same internal connection is implemented in the lower coil by shorting terminals B′ and C′. The TX coil is excited by connecting terminals A and D′ to the AC power source, while terminals D and A′ are intentionally left open. With this terminal configuration, the resulting inductance L_{top} or L_{bottom} interacts with the capacitance C to establish a series-resonant condition. For efficient wireless power transfer, the resonance frequencies of the TX and RX coils must be matched. Since the TX and RX coils have different

physical dimensions, their natural resonance frequencies are inherently different. As a result, the transmitter coil requires frequency tuning to ensure proper alignment with the receiver. In the proposed TX design, frequency tuning is achieved by adjusting the spacing between the two PCB layers. Varying this spacing directly modifies the interlayer capacitance, allowing precise control of the TX resonance frequency. Unlike conventional PCB implementations that rely on FR4 as the dielectric material, air is used as the dielectric medium in this configuration. Owing to its low dielectric constant (ε_r=1) and nearly zero loss tangent, air significantly reduces dielectric losses compared to FR4 (ε_r≈4.2). Moreover, using air provides greater design flexibility, as the PCB spacing serves as the primary tuning parameter.

4.5 Experimental Evaluation and Validation

To verify the proposed three-coil WPT architecture and quantify its power transfer capability, three different system implementations are realized and experimentally evaluated. The investigated cases, listed in Table I, comprise: (i) the proposed fully self-resonant three-coil topology with integrated mutual capacitance C_m and mutual inductance L_m, (ii) a conventional self-resonant three-coil configuration, and (iii) a baseline self-resonant two-coil system. The complete experimental arrangement is depicted in Fig. 12. As shown, DC input power is supplied by a programmable 6554A source, while a high-frequency AC waveform is generated using an H-bridge inverter built with EPC2305 GaN field effect transistor (FET). The inverter is driven by PWM signals with a 50% duty cycle and a 5-ns dead time, which are produced by a TMS320F28335 DSP controller. Prior to testing, the self-resonant frequencies of all fabricated planar coils are identified experimentally using an E5061B ENA network analyzer to ensure accurate resonance alignment across all configurations. The prototype is designed based on the receiver-side optimization criteria derived in this work. In particular, the intermediate and load coil inductances are chosen to be identical L_2=L_3, to promote balanced operation. For the proposed 3Coil system, receiver self-resonance is enforced by eliminating external tuning capacitances, such that $1/\omega C_2=1/\omega C_3=0$. Moreover, the receiver-side impedance is adjusted to satisfy $R_2(R_L+R_3)=2\omega^2 M_{23}^2$, which stabilizes the TX-RX current relationship even as the mutual inductance M_{23} is increased Table II summarizes the close

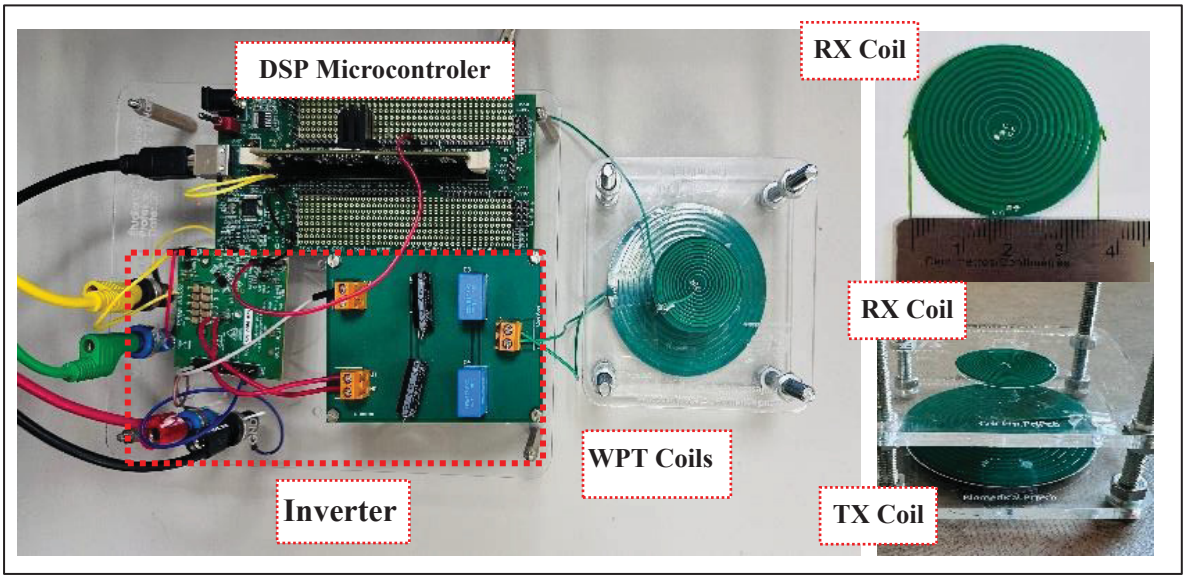

Figure 4.12 Experimental setup of the proposed SR WPT

agreement between simulated and measured results between proposed three coil and conventional three coils.

Fig. 13 compares the coupling coefficient for the investigated configurations under aligned and horizontally misaligned conditions, with a fixed transmission distance of 20 mm in the presence of misalignment. For all cases, the coupling coefficient decreases as the transfer distance increases. Compared to the self-resonant conventional three-coil and two-coil systems, the proposed 3Coil configuration consistently exhibits a higher coupling coefficient. This improvement is attributed to the inclusion of C_m and L_m, which enhance the reflected impedance and strengthen the effective magnetic coupling between the transmitter and receiver. A close agreement between simulation and experimental results is observed for all configurations.

Table 4.1 Design parameters of transmitter and receiver coils

Parameter	**TX**	**RX**
Number of turns	10	10
Inner radius	5 mm	2.5 mm
Outer radius	35 mm	17.5 mm
Thickness of trace (coil 2 & coil 3 in RX)	0.07mm	0.05mm
Thickness of trace (middle coil)	-	0.07mm
Scaling factor of TWR	0.9	0.9
Scaling factor of TGR	0.9	0.9
Thickness of dielectric layer (coil2 & coil3 in RX)	0.28mm	0.25mm
Air gap between top and bottom layer	0.6mm	-
Thickness of dielectric layer (middle coil)	-	0.30mm
Thickness of insulation layer	-	0.06mm

Table 4.2 Comparison measurement results of self-resonant three-coil and proposed SR three-coil topologies

Parameter	**Conventional SR 3Coil**		**Proposed 3Coil**	
	Transmitter	**Receiver**	**Transmitter**	**Receiver**
L (uH)	15.36	6.85	15.36	6.85
C (PF)	32	220	75	220
R (Ω)	1.35	1.36	1.35	1.47
f_r (MHz)	7.6	7.6	4.68	4.68

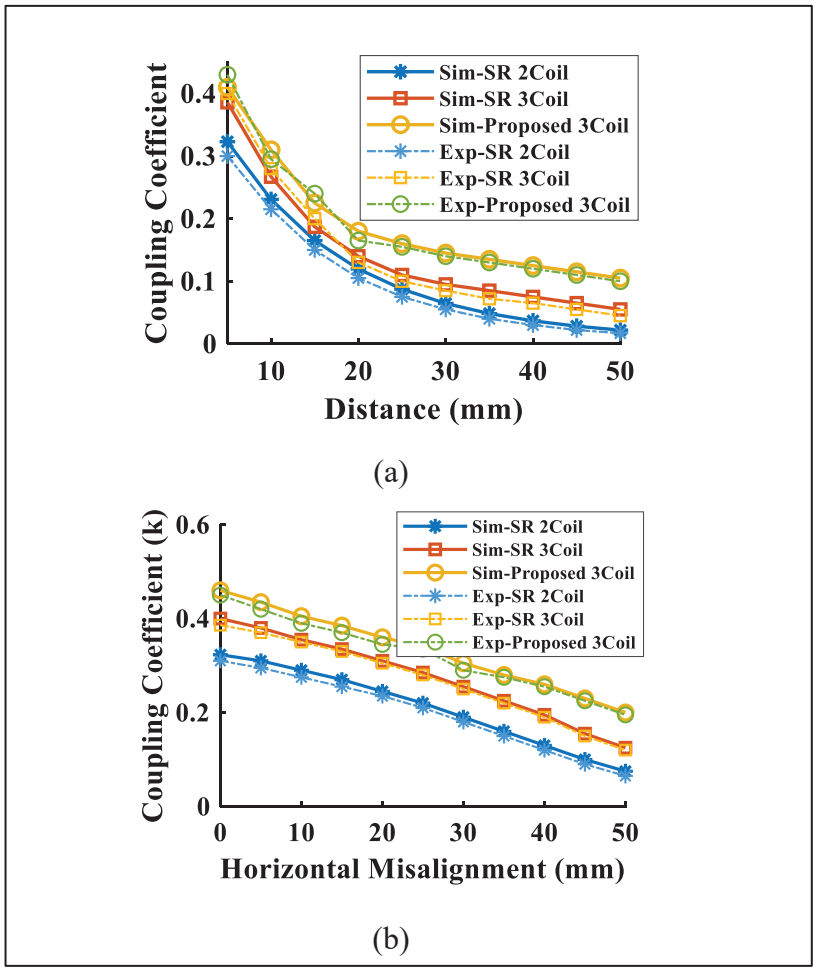

Figure 4.13 Coupling coefficient for SR 2-coil, conventional SR three-coil, and proposed three-coil systems: (a) vertical distance and (b) horizontal misalignment when the distance is 20mm

Fig. 14 presents the impedance magnitude and phase responses of the investigated coil configurations measured using an impedance network analyzer. For the self-resonant two-coil and conventional three-coil systems shown in Figs. 14(a) and (b), resonance occurs at approximately 7.6 MHz and 7.8 MHz, respectively, as indicated by the impedance minimum and zero phase crossing. The proposed three-coil configuration, depicted in Figs. 15(a) and (b), exhibits self-resonant behavior at 4.68 MHz with a pronounced impedance peak, reflecting an enhanced reflected impedance at the transmitter. The phase response confirms stable self-resonant operation at the corresponding resonant frequencies.

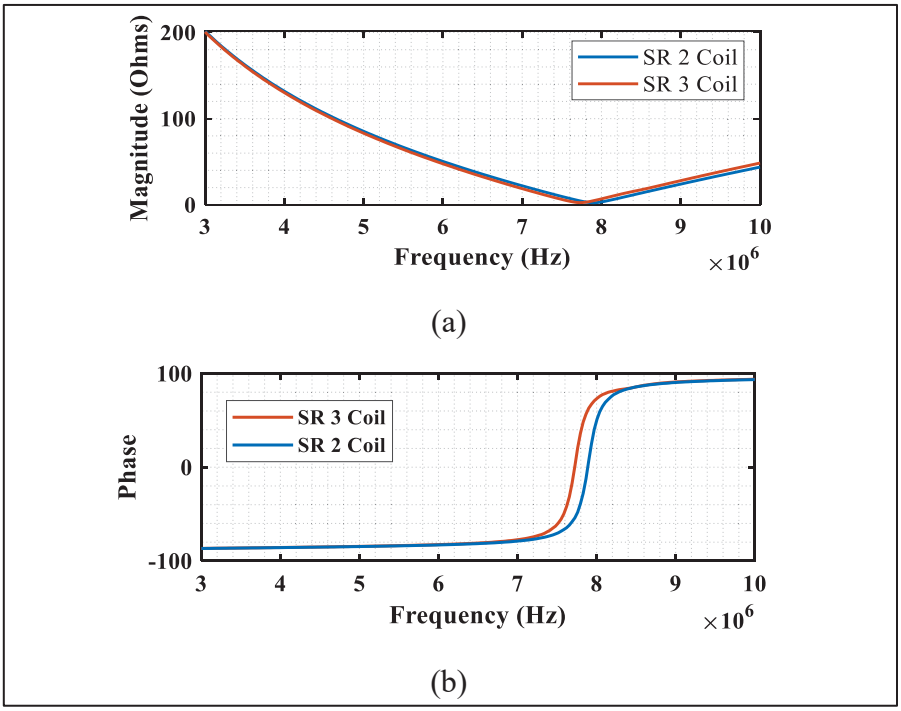

Figure 4.14 Frequency characteristics of the self-resonant 2Coil and conventional self-resonant 3coil. (a) Impedance, (b) Phase angle

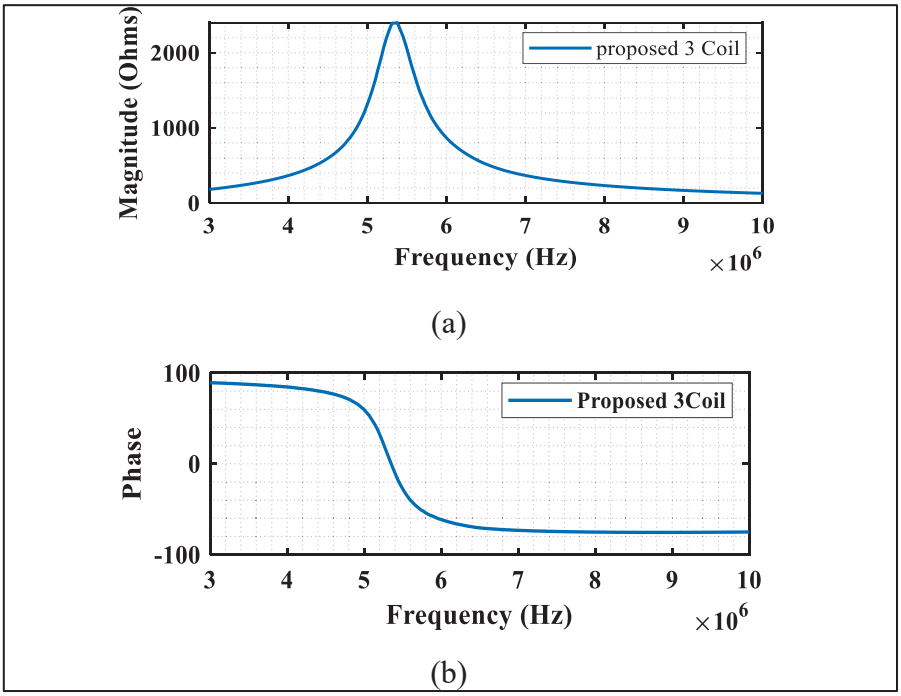

Figure 4.15 Frequency characteristics of the proposed self-resonant 3Coil. (a) Impedance, (b) Phase angle

Fig. 16 shows the output power and efficiency versus operating frequency at transmission distances of 20 mm and 40 mm. In all configurations, both metrics peak near resonance. At 20 mm, the proposed three-coil system achieves 267 mW with 89% efficiency, outperforming the conventional three-coil (240 mW, 78%) while remaining comparable in power to the two-coil system (301 mW, 77%). At 40 mm, the proposed configuration maintains superior performance, delivering 360 mW with 76% efficiency, compared to 212 mW and 67% for the conventional three-coil system and 113 mW and 31% for the two-coil system, demonstrating its effectiveness at extended distances.

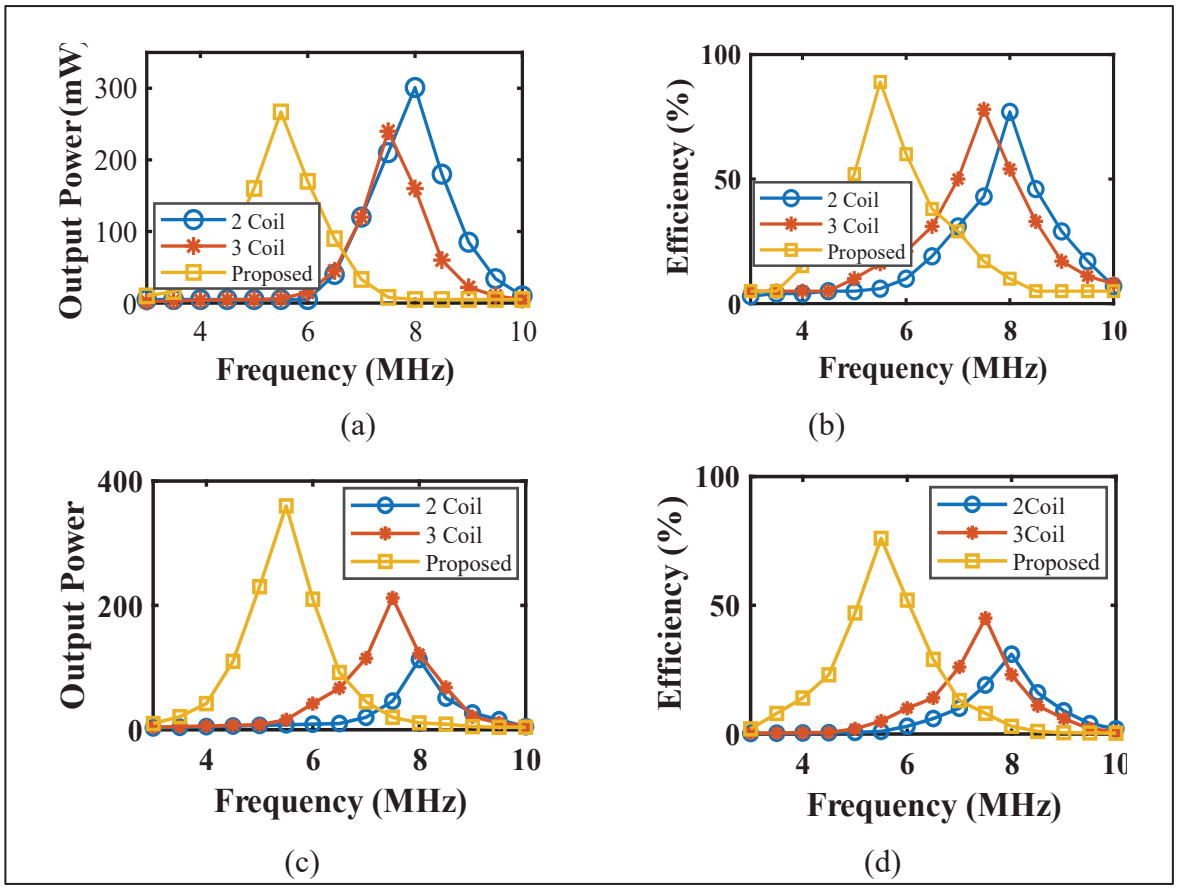

Figure 4.16 Output power and efficiency versus operating frequency at transfer distances of 20 mm and 40 mm**:** (a) output power at 20 mm, (b) efficiency at 20 mm, (c) output power at 40 mm, and (d) efficiency at 40 mm

Fig.17 and Fig.18 present a comprehensive comparison between simulation and experimental results for the three investigated coil configurations at V_{in}=1.5 V and R_L=1000 Ω, under different transmission distances and horizontal misalignment. As the transmission distance increases, the magnetic coupling weakens, leading to a gradual reduction in efficiency, output power, and gain for all configurations. Despite this degradation, the proposed three-coil system consistently maintains superior performance compared to the conventional three-coil and two-coil systems. While the two-coil configuration achieves its maximum output power of 365 mW only at a short distance of 5 mm and decreases to 273 mW at 25 mm for conventional three-coil, the proposed system delivers a comparable output power of 360 mW with 78% efficiency at a significantly larger distance of 40 mm, demonstrating an extended effective transmission range. A similar trend is observed under horizontal misalignment in Fig. 18 (a)-(c). Lateral displacement reduces the magnetic coupling in all cases; however, the proposed configuration exhibits enhanced robustness, preserving higher efficiency, output power, and gain over the entire misalignment range when compared with the reference systems.

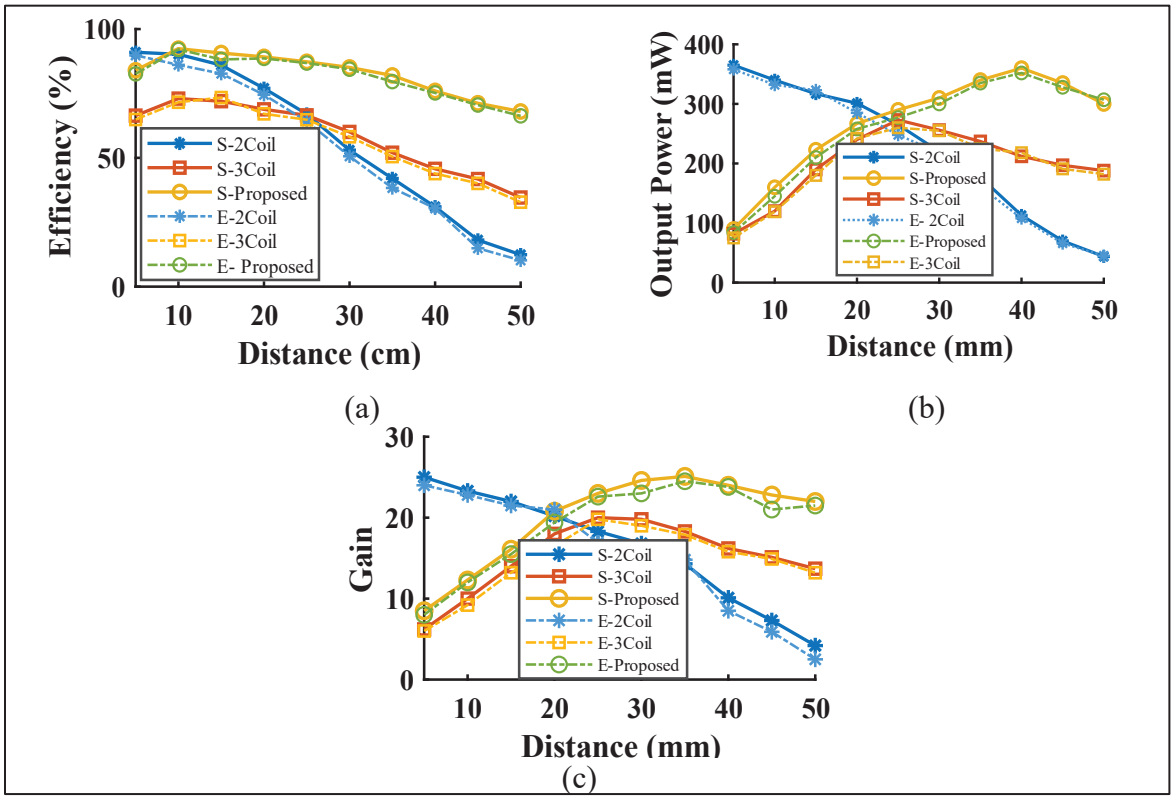

Figure 4.17 Simulation and experimental results of the three coil configurations at different transmission distances: (a) output power, (b) efficiency, and (c) voltage gain

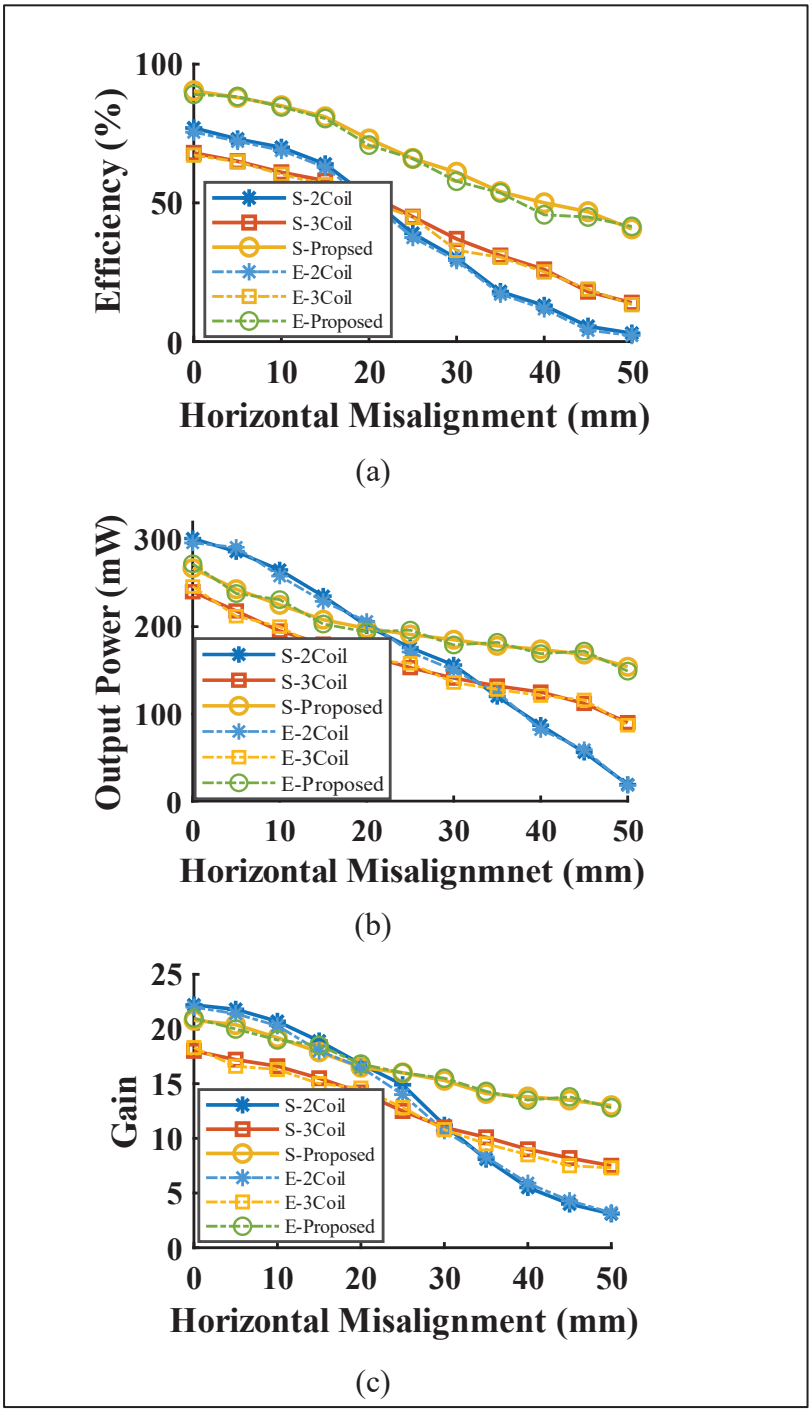

Figure 4.18 Simulation and experimental results of the three coil configurations at different horizontal misalignment**:** (a) output power, (b) efficiency, and (c) voltage gain.

4.6 Conclusion

This study introduces an enhanced self-resonant three-coil WPT topology specifically developed for applications with size-constrained receiver coils, and evaluates its performance against conventional self-resonant three-coil and self-resonant two-coil configurations. By jointly tuning the mutual capacitance C_m, mutual inductance L_m, coil voltage polarity, and coupling factor K_{23}, the proposed design increases the reflected impedance R_{ref2}, thereby enhancing power transfer efficiency. A compact, capacitor-free RX is implemented using three double-layer PCB coils. Proper interconnection of Coil 2 and Coil 3 increases the effective inductance up to four times, while in relay coil, leaving auxiliary terminals unconnected naturally forms a series L_m–C_m combination, boosting impedance and robustness. Two RX-side strategies equal inductor splitting (L_2=L_3) and capacitive reactance balancing ($1/\omega C_2 \approx 1/\omega C_3 \approx 01$) further improve efficiency. On the transmitter side, the condition $R_2(R_L + R_3) = 2\omega^2 M_{23}^2$ stabilizes the TX–RX current ratio as M_{23} increases. Replacing the FR4 dielectric with an air-core structure allows flexible resonance tuning and reduces dielectric losses. The proposed system achieves load-independent RX operation, reduces intermediate coil current I_2, and enhances load current I_3. Simulations and experiments confirm peak efficiency of 92%, a voltage gain of 25.1, and 360 mW output power, outperforming conventional self-resonant three-coil and self-resonant two-coil WPT system.

CHAPTER 5

EFFICIENT WIRELESS POWER TRANSFER WITH SELF-RESONANT THREE COIL DESIGN

Neda Zahedi Saadabad [a], Javad Nekoui [a], Qingsong Wang [a], Ambrish Chandra [a]

[a] Department of Electrical Engineering, École de technologie supérieure,
1100 Notre-Dame Ouest, Montréal, Québec, Canada H3C1K3

Article published in *IEEE Canadian Conference on Electrical and Computer Engineering (CCECE), May 2025,* available at https://ieeexplore.ieee.org/abstract/document/11364471

Abstract

Wireless power transfer (WPT) systems face challenges in maintaining high efficiency over long distances due to energy losses and misalignment. Multi-coil architectures, particularly three-coil configurations, provide an effective solution to enhance both transfer efficiency and range. Series compensation is widely adopted for its simplicity and ease of implementation. In addition, using self-resonant coils eliminates the need for external capacitors, further enhancing system efficiency and simplifying the design. This study proposes a series-series self-resonant three-coil WPT system with planar coils. Track width ratio (TWR) and track gap ratio (TGR) structures have been implemented to reduce losses and improve the quality factor of the coils. Experimental results demonstrate the system's effectiveness, achieving maximum efficiency of 87.2% at 70mm and 42% at a 150 mm distance between the relay and load coils, with 200 mm coil diameters and a 10 Ω load.

5.1 Introduction

Wireless Power Transfer (WPT) enables the efficient and seamless transmission of electrical energy across an air gap without the need for physical connections between the transmitter coil and receiver coil, which has garnered substantial interest from academia and industry alike, finding critical applications in areas such as electric vehicles and biomedical implants (Faisal, Farooq et al., 2024; SHIN, Shin Jaegue et al., 2023). The primary objective of WPT is to provide adequate power delivery to the load while sustaining high power transfer efficiency (PTE) under conditions of significant distances or coil misalignment. In a two-coil wireless power transfer system, consisting of a transmitter coil and a receiver coil, the power transfer efficiency declines as the distance between the coils grows, which poses a major challenge for its application in long-range scenarios. As a result, considerable research has focused on using relay coils to extend the power transfer distance. It has been demonstrated that incorporating relay coils can significantly enhance both the efficiency and range of a wireless power transfer system (Moon, Kim, Cho, Ahn & Moon, 2014; Machnoor, Rodríguez, Kosta, Stang, & Lazzi, 2018; Kiani Jow & Ghovanloo, 2011; Abatti, de Miranda, da Silva & Pichorim, 2018; Zhong, Zhang, Liu & Hui, 2014; de Miranda & Pichorim, 2022; Zhang et al., 2024). Furthermore, by fine-tuning the position of the relay coil relative to the primary or secondary coils, the load voltage can be accurately controlled to meet particular requirements (Zahedi, Nasiri & Nekoui, 2024; Zahedi, Hosseini, Nasiri & Sabahi, 2020). In (Moon, Kim, Cho, Ahn & Moon, 2014), adding a relay coil coplanar with the transmitter and receiver coil enhances its self-inductance and coupling with the load, significantly improving the efficiency of three-coil WPT systems over two-coil designs. In (Machnoor, Rodríguez, Kosta, Stang, & Lazzi, 2018), a three-coil system was proposed to improve efficiency in implantable devices by utilizing mutual coupling, capacitance, and polarity. At a 50 mm separation, the system achieved 40% efficiency, significantly surpassing conventional three-coil and two-coil designs with less than 10% efficiency. A 3-coil inductive power transfer link has been developed to enhance both PTE and output power, as demonstrated in (Kiani Jow & Ghovanloo, 2011). This system achieved a 37% PTE at 13.56 MHz and a 12-cm distance, with an output power of 1.5 and 59 times higher than 2-coil and 4-coil links, respectively. In (Abatti, de Miranda, da Silva &

Pichorim, 2018), another three-coil WPT system is analyzed, revealing that efficiency and power transfer depend solely on the transmitter and relay circuits, not on load resistance or mutual inductance. The conditions for improving the efficiency of a three-coil WPT system compared to a two-coil system are examined in (Zhong, Zhang, Liu & Hui, 2014; de Miranda & Pichorim, 2022). It is shown that when the mutual inductance between the transmitter coil and relay coils is sufficiently large, the power transfer efficiency is significantly enhanced. The studies recommend positioning the relay coil coplanar with the transmitter coil to optimize performance. A three-coil WPT system was presented in (Zhang et al., 2024), where impedance matching was achieved on both TX and RX sides by electronically adjusting the inductance of the reconfigurable relay coil (RRC), resulting in improved transmission ratio and load power.

In Wireless Power Transfer (WPT) systems, self-resonant coils have become an attractive solution for eliminating the need for external tuning capacitors (Zahedi, Wang & Chandra, 2023; Zahedi, Wang & Chandra, 2023). These coils rely on their inherent self-inductance and self-capacitance to reach their self-resonant frequency (SRF), avoiding issues like capacitor damage and the high voltage and current stress typically seen in resonant conditions. By harnessing parasitic capacitance from coil turns or parallel plates, Self-Resonant
WPT (SRWPT) systems improve system reliability and performance and eliminate the size and cost associated with external capacitors (Wang, Saket, Troy & Ordonez 2020). Planar coils, in particular, are well-suited for this purpose, utilizing the parasitic capacitance between layers to achieve self-resonance, making them ideal for applications requiring miniaturized circuits, such as those in implanted biomedical devices (Yi, Li, Muneer, He & Yang, 2020).
This work aims to integrate the benefits of optimized self-resonant coils, characterized by high-quality factors operating at their intrinsic SRF, with the multiple-coil architecture in a WPT system. By employing series RLC compensation where the resonant impedance is minimized, this design enhances efficiency and practicality, offering a robust solution for implementing a multiple-coil self-resonant WPT system. This paper is structured as follows: section II provides

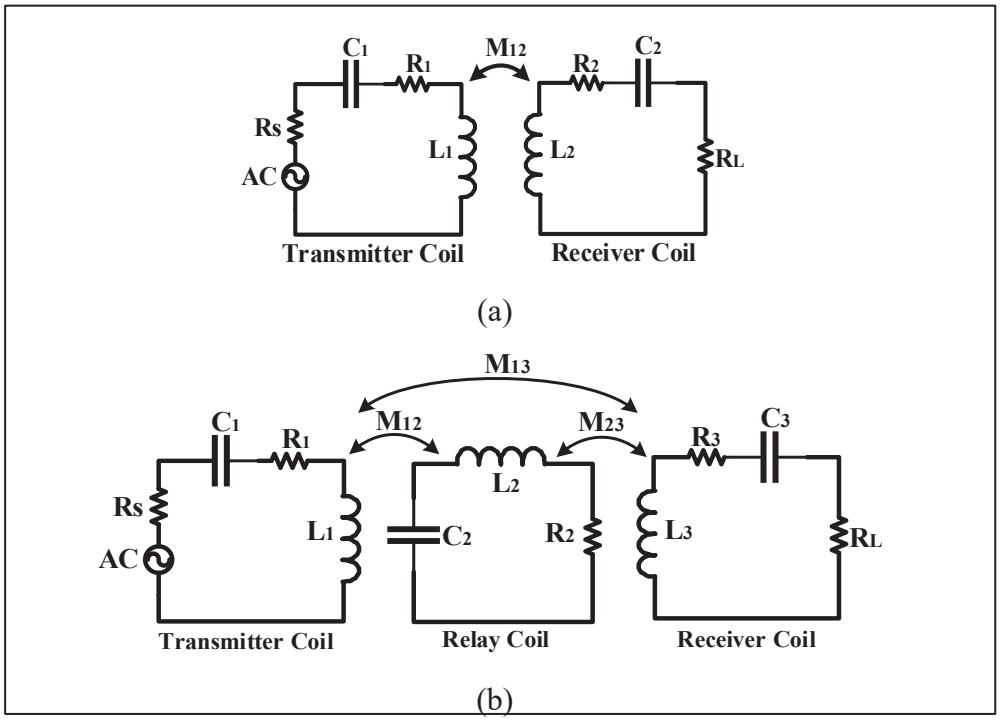

Figure 5.1 Lumped circuit models of (a) Two coil WPT, (b) Three-coil WPT

an analysis of conventional two-coil and three-coil systems. Section III outlines the coil configurations along with their theoretical analysis. Section IV presents simulation results and experimental validation, and Section V concludes the study.

5.2. Analysis of Conventional Two-Coil and Three-Coil Wireless Power Transfer System

5.2.1 Conventional Two-Coil WPTs

A series-series two-coil inductive power transfer system is presented in Figure 5.1 (a), where V_{in} represents the excitation voltage, R_1, C_1, and L_1 are the transmitter's resistance, capacitance, and inductance, respectively. On the receiver side, L_2, R_2, C_2, and R_L are the receiver's inductance, resistance, capacitance, and load resistance, respectively. The mutual inductance between the transmitter and receiver coils is denoted by M_{12}. Maximum power transfer efficiency (PTE) is achieved when both LC circuits are tuned to the same resonant frequency

($w_o = \sqrt{L_1 C_1}^{-1} = \sqrt{L_2 C_2}^{-1}$). The efficiency can be determined by calculating the load power and the total power supplied by the source as follows:

$$\eta_{2coil} = \frac{w_o^2 M_{12}^2}{R_1 R_2 + w_o^2 M_{12}^2} \tag{5.1}$$

Based on the (5.1), the efficiency improves as mutual inductance (M_{12}) increases. However, if the distance between the coils grows or M_{12} decreases, the efficiency decreases substantially.

5.2.2 Conventional Three-coil WPTs

A series-series three-coil inductive power transfer system is shown in Figure 5.1 (b), where the transmitter, relay, and receiver coils are coupled. Maximum power transfer efficiency (PTE) is reached when all coils are tuned to the same resonant frequency ($w_o = \sqrt{L_1 C_1}^{-1} = \sqrt{L_2 C_2}^{-1} = \sqrt{L_3 C_3}^{-1}$), and the efficiency is determined by the load power and total power from the source, as follows:

$$\eta_{3coil} = \frac{R_2 w_o^2 M_{12}^2 w_o^2 M_{23}^2}{(R_2 w_o^2 M_{12}^2 + R_1 (R_2 R_3 + w_o^2 M_{23}^2))(R_2 R_3 + w_o^2 M_{23}^2)} \tag{5.2}$$

(5.2) illustrates how maximum efficiency is influenced by the mutual coupling between the transmitter and relay coils (M_{12}), as well as between the relay and load circuits (M_{23}). This highlights a significant benefit of multi-coil WPT systems, where efficiency can be enhanced as the distance between the coils increases. When the relay coil is lossless ($R_2 = 0$), the efficiency is described as follows:

$$\eta_{3coil\_ideal} = \frac{R_3 M_{12}^2}{R_3 M_{12}^2 + R_1 M_{23}^2} \tag{5.3}$$

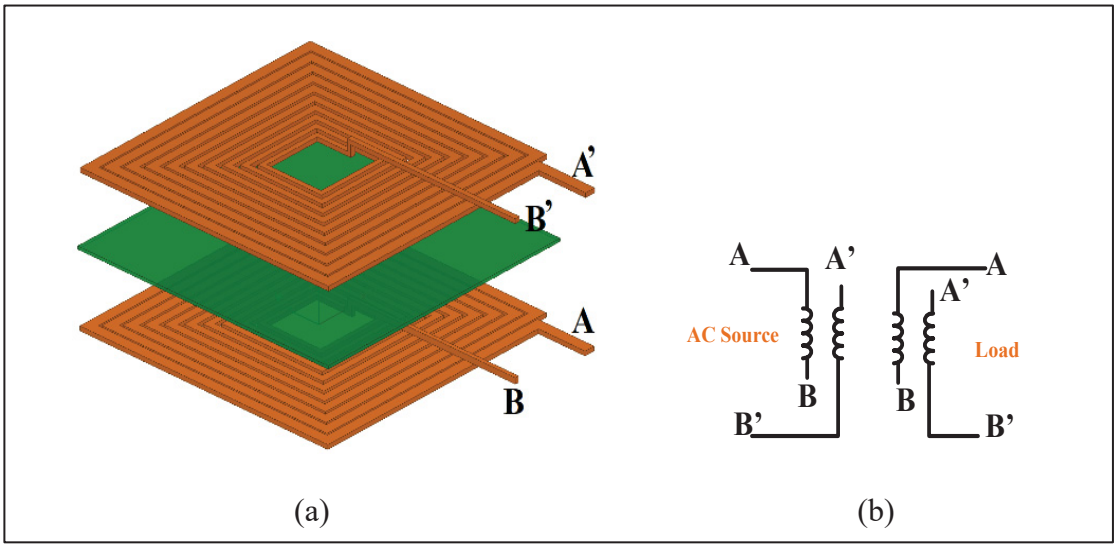

Figure 5.2 (a) Structure of the proposed double-layer self-compensated PCB coils, (b) Equivalent circuit of the coils

In the absence of losses in the relay coil (R_2=0), the efficiency depends solely on the mutual inductance between the transmitter and relay coils (M_{12}), rather than the transmitter and receiver (M_{13}). Under these ideal conditions, the efficiency approaches 100% when the transmitter and relay coils are tightly coupled, while the mutual coupling between the relay and load diminishes ideally as the distance between the relay and load circuits tends to infinity.

5.3 Coil Topology and Theoretical Model

The design shown in Figure 2 (a) features a dual-layer PCB with a spiral coil, where a dielectric material separates the coils to create inter-turn capacitance. In this configuration, connections at A' and B are left open, while A and B' are linked to an alternating current (AC) source, forming a series LC circuit. The structure incorporates a hollow spiral pattern, and adjustments to the track width and gap are employed to reduce the AC resistance by preventing the current from flowing through the core area, which experiences the highest magnetic field. This strategy significantly lowers the resistance for various coil shapes and enhances the overall quality factor.

5.3.1 Inductance

The inductance of a planar coil is calculated by combining the self-inductance of each individual trace and the mutual inductance between traces. The concept of partial inductance is used to model these interactions. Mutual inductance is positive when the currents in the traces flow in the same direction and negative when they flow oppositely.

$$L = L_s + M_P + M_N \tag{5.4}$$

$$L_S = \sum_{n=1}^{N} 0.8 d_n \left[\ln\left(\frac{2d_n}{w_n + t} \right) + \frac{w_n + t}{3d_n} + 0.5 \right] \tag{5.5}$$

$$M_P = 4 \sum_{i=1}^{N} \sum_{j=1}^{N-k} M(i, i+j) \tag{5.6}$$

$$M_N = 2 \sum_{i=1}^{N} \sum_{j=1}^{N} M(i, j) \tag{5.7}$$

The total inductance L, self-inductance L_S, positive mutual inductance M_P, and negative mutual inductance M_N of the coil are defined in (μH). The parameter d_n represents the side length of each coil turn, while t is the trace thickness. The mutual inductance between two traces on the same side is denoted as $M_1(j,j+k)$ for the jth and (j+k)th turns, and the mutual inductance between traces on opposite sides is denoted by $M_2(x,y)$, for the x-th and y-th turns.

5.3.2 Capacitance

To simulate the intra-winding capacitance, the coil is made up of two layers separated by a dielectric material. In this setup, the electric field includes a vertical component passing through the dielectric, as well as minimal fringe fields between neighboring traces. As shown in Fig. 3, a thin dielectric layer is placed between the copper layers. The capacitance between

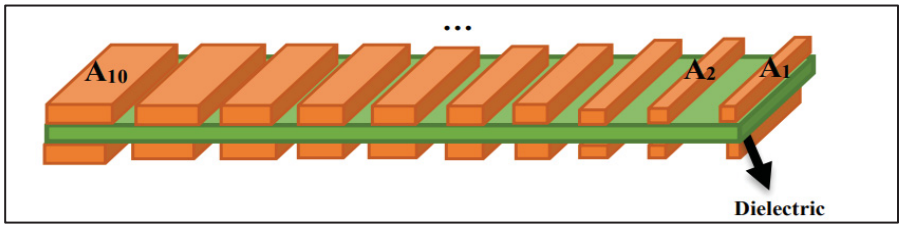

Figure 5.3 Capacitance calculation of proposed coil structure

the top and bottom conductors is calculated in the same way as a parallel plate capacitor, with the total area of each layer being the sum of the areas of all individual turns.

$$A_T = A_1 + A_2 + \ldots + A_N \tag{5.8}$$

The capacitance between the winding layers is derived using the following expression:

$$C_{intra-winding} = k\varepsilon_o \frac{A}{d} \tag{5.9}$$

Where, d refers to the thickness of the dielectric layer, k is the relative permittivity of the dielectric material, and ε_0 is the permittivity of free space.

5.3.3. Quality Factor

The inductance, intra-winding capacitance, and resistance emphasize the influence of variations in the number of turns, trace thickness, width, and gap in a self-resonant planar coil. Consequently, the quality factor of the system is given by (5.10):

$$Q = \frac{wL_{eq}}{R_{eq}} \tag{5.10}$$

In this context, R_{eq} represents the equivalent resistance, which accounts for both the skin effect and proximity effect and can be calculated as described in (Awuah, Danuor, Moon & Jung, 2023). Additionally, the dielectric losses are computed based on the method provided in (Li & Costinett, 2018).

5.3.4 TWR+TGR

The resistance losses caused by proximity effects are higher in the inner turns of the coil due to stronger magnetic fields. Reducing the trace width can minimize these losses, but it also increases resistance due to the skin effect. Increasing the distance between turns can reduce proximity losses because the magnetic field strength from adjacent turns becomes weaker. Our proposed TWR-TGR coil design addresses this issue by using narrower trace widths and larger gaps between turns, which reduces both skin-effect and proximity-effect losses, ultimately improving the coil's quality factor. In this design, the conductor width increases from the center to the outer turns, while the gap between adjacent turns decreases. After determining the width of the outermost conductor, each inner conductor width is progressively reduced by a factor (α) according to the following equation:

$$W_n = \alpha^{n-1} W \tag{5.11}$$

Where n represents the turn number, starting from 1 for the outermost turn. Additionally, the gap between the turns reduces from the center to the outer edge of the coil, ranging from 3.7mm down to 2.1mm. These modifications effectively reduce losses. Further details are presented in Table 5.1.

Table 5.1 Design parameters

Parameter	**Value**
Number of turns	10
Inner length	49 mm
Outer length)	214 mm
Thickness of trace	0.072 mm
Outer coil width	8 mm
Scaling factor	0.9
Inter-turn gap	3.7 mm to 2.1 mm
Thickness of dielectric	0.2 mm

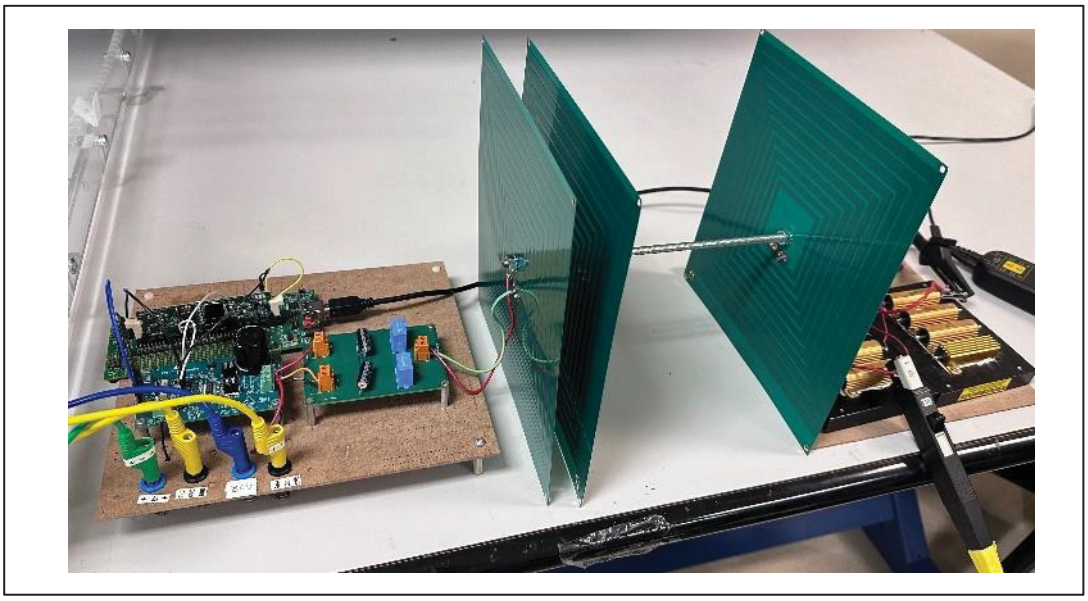

Figure 5.4 Experimental setup of the proposed SR WPT

4.1 Simulation and Experimental Results

To validate the proposed 3-coil WPT system and measure its power transfer efficiency, three self-resonant planar coils, detailed in table 5.1, were fabricated and shown in Figure 5.4. The experimental arrangement included a Tektronix AFG3101 function generator, a Tektronix DPO4054 digital oscilloscope, and a network analyzer E5061B. The electrical parameters of the self-resonant planar coils were measured, yielding an intra-capacitance of 7.2 nF, resistance of 1023.4 mΩ, inductance of 24.97 μH, resonant frequency of 375.357 kHz, and a quality factor of 57.54. The resistance R_1 was determined at the self-resonant frequency (f_r), identified by a zero-phase angle and the point of minimum impedance. Intra-capacitance was measured at 10 kHz, while the quality factor (Q) was evaluated as the ratio of f_r to the frequency range where the phase angle deviates by ±45 degrees. The inductance of the open coil was then computed using Q, R_1, and f_r based on a defined formula.

$$L = \frac{R_1 Q}{2\pi f_r} \tag{5.12}$$

For comparative analysis, two self-resonant coils were designed and fabricated with identical specifications to those used in the three-coil WPT system, including geometry, material properties, and number of turns. Experimental measurements and simulations were conducted to evaluate the performance of the coils. In the experiment, a sinusoidal voltage of 10 V at 375 kHz was applied to the transmitter coil, including a 50 Ω generator impedance and a 5 Ω shunt resistor to measure the current (i_T) using an oscilloscope. The source power was calculated as $P_T=V.i_T$. The relay circuit consisted of a self-resonant coil with terminals shorted, while the receiver circuit included a 10 Ω resistor (R_l) for load current measurement i_L and total load resistance defined as $R_L=R_l+R_3$. The load power $P_L=R_L i_L^2$ and efficiency $\eta=P_L/P_T$ were computed. Coils were coaxially aligned, and the load-relay coil distance was varied in 5 mm steps from 20 mm to 200 mm. Measurements were performed for transmitter-relay coil separations of 20, 40, and 60 mm. To analyze the efficiency η according to equation (5.3), it is necessary to account for the planar coil resistance (R_1) alongside the external resistances (R_{shant} and R_L) and the generator impedance (R_g). The resistance values are determined as follows: R_{TX}, representing the total transmitter resistance, is given by $R_g+R_1+R_{shant}=56.023\ \Omega$, R_2 the relay resistance, is $R_2=1.023\ \Omega$, and R_L, the load resistance, is $R_3+R_L=11.023\ \Omega$. These calculations comprehensively capture the resistances in each section of the circuit.

Figure 5.5 presents the coupling coefficient k_{12} and k_{23} simulations for two-coil and three-coil setups. In the three-coil system, Tx-to-relay coil distances of 20 mm, 40 mm, and 60 mm were analyzed, with relay-to-Rx coil distances varying from 25 mm to 200 mm in 5 mm steps. With greater distance, k_{12} rises, while k_{23} decreases. This behavior arises because, as RX moves farther from the relay, its loading effect on the relay weakens. This allows TX to couple more effectively with the relay, increasing k_{12}, while the reduced proximity between the relay and RX decreases k_{23}.

The efficiency of the three-coil WPT system, including experimental, simulation, and theoretical results, is presented in Figure 5.6(a)–(c). For comparison, Figure 5.7 illustrates the efficiency of a two-coil system with identical parameters for the transmitter and load circuits.

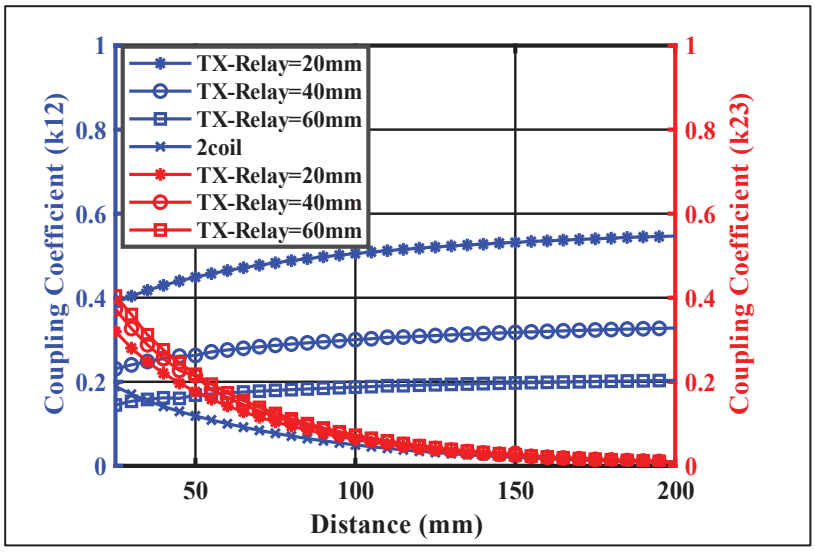

Figure 5.5 Coupling coefficient (k_{12}) and (k_{23}) in different distances between Relay-RX

As shown, the two-coil system delivers higher efficiency at shorter distances, while the self-resonant three-coil configuration excels at longer distances. For example, at a 150 mm separation, the two-coil system achieves 28% efficiency, whereas the three-coil setup reaches 42% efficiency with a 20 mm TX-to-relay distance. Additionally, as the transmitter-relay gap increases (40 mm and 60 mm), the peak efficiency decreases, but the point of maximum efficiency shifts to greater distances, aligning with expected trends. The minor discrepancy between the measured and calculated values is expected, as the mutual inductance between the transmitter and load circuit was not included in (5.3).

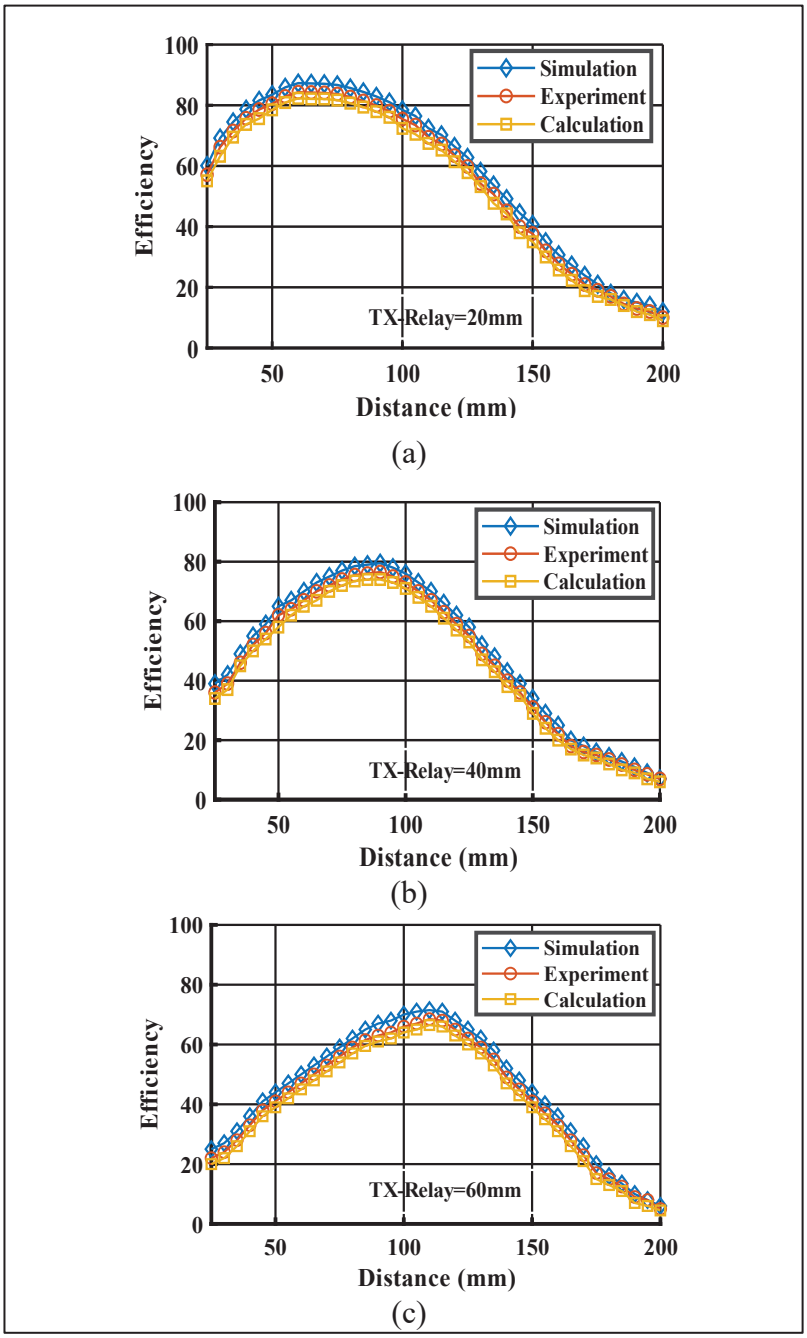

Figure 5.6 Measured, simulated, and calculated the efficiency of three coils WPT in different distances between the relay and the receiver (RX). (a) TX-Relay at 20 mm, (b) TX-Relay at 40 mm, and (c) TX-Relay at 60 mm

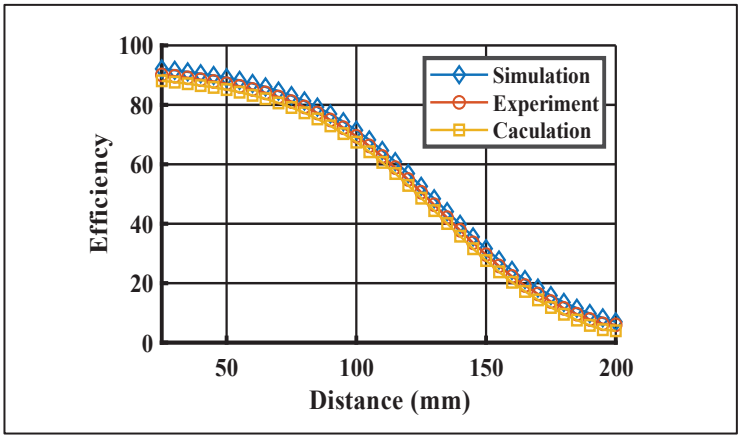

Figure 5.7 Measured, simulated, and calculated efficiency of two-coil WPT as a function of the distance between the relay and the receiver

5.1 Conclusion

This paper presents a high-efficiency three-coil wireless power transfer (WPT) system featuring key innovations that enhance performance and scalability. Tuning the circuits to the coils' self-resonant frequencies (SRF) eliminates the need for discrete capacitors, simplifying the design while maintaining high functionality. The system employs planar coils, enabling a compact design and efficient energy transfer, with series compensation achieved through precise circuit tuning. The proposed three-coil configuration addresses the limitations of traditional two-coil systems, where efficiency significantly decreases over longer distances. To further optimize performance, track width ratio (TWR) and track gap ratio (TGR) structures are implemented, effectively reducing losses and enhancing the quality factor. Experimental results validate the system's effectiveness, achieving a peak efficiency of 42% at a 150 mm distance between the relay and load coils, and a maximum efficiency of 87.2% at a 70 mm distance. These advancements make the proposed system highly suitable for high-power applications, including electric vehicle charging and miniaturized biomedical devices.

CONCLUSION

Wireless Power Transfer (WPT) technology is evolving toward more compact, reliable, and efficient architectures that minimize component count while maximizing performance. Conventional resonant WPT systems rely on external compensation networks to establish resonance, which inevitably introduce additional components, dielectric losses, voltage stress, and reduced structural robustness. In contrast, self-resonant wireless power transfer (SRWPT) systems embed resonance within the intrinsic electromagnetic properties of the coil itself. However, achieving practical, efficient, and scalable SRWPT operation requires more than eliminating external capacitors; it demands a comprehensive understanding of electromagnetic interactions, structural configuration, geometrical influence, and multi-coil impedance behavior.

This thesis demonstrates that performance enhancement in SRWPT systems can be systematically achieved through structural electromagnetic engineering at three fundamental levels: multilayer coil construction, geometry-driven optimization, and architectural impedance manipulation using multi-coil configurations. Rather than relying on circuit-level compensation techniques, the work establishes a design methodology in which resonance control, efficiency improvement, and power scalability are inherently realized within the coil structure and system architecture.

Chapter 1 established the theoretical and analytical foundation of the thesis through a comprehensive review of self-resonant coil structures. Various wire-based and PCB-based configurations were categorized and analyzed, and detailed modeling of inductance, distributed capacitance, resistance, resonant frequency, quality factor, copper losses, dielectric losses, power capability, and EMI considerations was presented. The chapter clarified that SRWPT performance depends on the coupled interaction between electromagnetic parameters, structural layout, and loss mechanisms. This integrated understanding formed the scientific basis for the structural, geometrical, and architectural optimizations developed in the subsequent chapters.

Chapter 2 addressed structural optimization of self-resonant coils through multilayer PCB implementation. By connecting multiple double-layer coils in parallel, the effective electromagnetic behavior of the structure was engineered to simultaneously increase distributed capacitance and reduce equivalent AC resistance through current sharing. The integration of Track Width Ratio (TWR) and Track Gap Ratio (TGR) further minimized conduction losses and improved quality factor. This chapter demonstrated that low-frequency and high-efficiency self-resonant operation can be achieved through deliberate multilayer structural design, establishing the importance of layout-level electromagnetic control in capacitor-free WPT systems.

Chapter 3 investigated the impact of planar coil geometry on SRWPT system performance. Under identical electrical conditions, circular, square, hexagonal, and octagonal geometries were comparatively analyzed. The study revealed that geometry significantly influences inductance distribution, inter-turn capacitance, coupling behavior, misalignment tolerance, and power transfer capability. Each geometry exhibited distinct electromagnetic characteristics, highlighting that geometry selection is not merely mechanical but fundamentally electromagnetic. This chapter provided practical design insight into tailoring coil shape based on efficiency, power density, and robustness requirements.

Chapter 4 introduced an enhanced self-resonant three-coil architecture aimed at improving impedance transfer and efficiency in size-constrained receiver applications. Instead of increasing receiver dimensions to raise inductance, a third coil was strategically employed to amplify reflected impedance and strengthen power delivery to a compact receiver. By engineering mutual inductive and capacitive interactions between coils, the architecture improved load-side efficiency without compromising footprint. This chapter demonstrated that architectural impedance manipulation through multi-coil interaction is an effective strategy for overcoming physical size limitations in SRWPT systems.

Chapter 5 extended the architectural concept to improve efficiency at increased transfer distances. A self-resonant three-coil configuration incorporating a relay coil was developed to enhance magnetic coupling and stabilize power transfer under larger separation gaps. The integration of structural optimization and multi-coil interaction enabled higher efficiency

retention compared to conventional two-coil systems. This chapter confirmed that distance scalability in capacitor-free SRWPT systems can be achieved through architectural enhancement rather than additional compensation circuitry.

Future Work

This thesis established a coherent design framework for high-performance self-resonant wireless power transfer (SRWPT) systems, with a primary focus on low-frequency and medium-power applications. Through multilayer structural engineering, geometry-driven electromagnetic optimization, and impedance-enhanced multi-coil architectures, efficient and capacitor-free operation was demonstrated under practical spatial constraints. However, the proposed methodologies do not represent the final stage of optimization for self-resonant systems. The presented framework can be further extended and scaled toward higher power levels, enhanced robustness, and industry-grade implementations. Several research directions can therefore be pursued as future work.

High-Power Wireless EV Charging Based on Self-Resonant Multilayer Coils

A major future research direction is extending the proposed self-resonant multilayer coil architecture to high-power electric vehicle (EV) wireless charging systems operating at 85 kHz. While this thesis demonstrates efficient capacitor-free operation in low and medium-power applications, scaling to EV-level power requires careful optimization of high-current PCB traces, multilayer stacking, thermal management, and mechanical robustness. Future work will aim to design compact, high-efficiency charging pads capable of maintaining high coil-to-coil efficiency under practical air gaps and realistic misalignment conditions, while complying with EV charging standards and safety regulations.

Adaptive Impedance-Tracking and Intelligent Control Integration

Another promising direction is integrating adaptive impedance-tracking strategies with self-resonant architectures to enhance robustness under dynamic operating conditions. In practical EV applications, coupling coefficients vary due to vehicle positioning, temperature drift, and load fluctuations. Future research can focus on real-time monitoring of reflected impedance and intelligent control algorithms that maintain operation near the zero-phase-angle condition. This structural–control co-design approach would improve efficiency stability without reintroducing bulky external compensation networks.

Thermal–Electromagnetic Co-Optimization for High-Current Operation

As power levels increase, thermal limitations become critical in multilayer PCB self-resonant coils. Future studies can investigate coupled thermal electromagnetic modeling to optimize copper thickness, trace geometry, inter-layer spacing, and dielectric materials. Understanding the interaction between AC copper losses, proximity effects, and temperature-dependent material behavior will enable the development of scalable design guidelines for high-power, fast-charging EV platforms while preserving efficiency and reliability.

EMI/EMF-Compliant Field Shaping for Large-Scale Deployment

For practical EV infrastructure deployment, compliance with electromagnetic exposure (EMF) and EMC standards is essential. Future work can focus on advanced magnetic field shaping using optimized meta-surface patterns and current distribution engineering to enhance coupling while minimizing stray magnetic fields. Establishing standardized design methodologies that satisfy international regulations without increasing system volume or complexity will be crucial for commercial implementation

LIST OF BIBLIOGRAPHICAL REFERENCES

Abatti, P. J., de Miranda, C. M., da Silva, M. A., & Pichorim, S. F. (2018). Analysis and optimisation of three-coil wireless power transfer systems. IET Power Electronics, 11(1), 68-72.

Aditya, K., & Williamson, S. S. (2014, June). Design considerations for loosely coupled inductive power transfer (IPT) system for electric vehicle battery charging-A comprehensive review. In 2014 IEEE Transportation Electrification Conference and Expo (ITEC) (pp. 1-6). IEEE.

Akyel, C., Babic, S., & Kincic, S. (2002). New and fast procedures for calculating the mutual inductance of coaxial circular coils (circular coil-disk coil). IEEE Transactions on Magnetics, 38(5), 2367-2369.

Awuah, C. M., Danuor, P., Moon, J. I., & Jung, Y. B. (2023). Novel coil design and analysis for high-power wireless power transfer with enhanced Q-factor. Scientific Reports, 13(1), 4187.

Aydin, E., Kosesoy, Y., Yildiriz, E., & Aydemir, M. T. (2018, November). Comparison of hexagonal and square coils for use in wireless charging of electric vehicle battery. In 2018 International Symposium on Electronics and Telecommunications (ISETC) (pp. 1-4). IEEE.

Bosshard, R., & Kolar, J. W. (2016). Multi-objective optimization of 50 kW/85 kHz IPT system for public transport. IEEE Journal of Emerging and Selected Topics in Power Electronics, 4(4), 1370-1382.

Breitkreutz, B., & Henke, H. (2013). Calculation of self-resonant spiral coils for wireless power transfer systems with a transmission line approach. IEEE Transactions on Magnetics, 49(9), 5035-5042.

Campi, T., Cruciani, S., Maradei, F., Montalto, A., Musumeci, F., & Feliziani, M. (2021). Centralized high power supply system for implanted medical devices using wireless power transfer technology. IEEE Transactions on Medical Robotics and Bionics, 3(4), 992-1001.

Cen, G., Wang, C., Yang, P., Zalhaf, A. S., & Han, Y. (2024). Automatic resonance tuning in wireless power transmission system utilizing flexible coil. IEEE Transactions on Power Electronics, 39(12), 16916-16932.

Chakibanda, V., & Komanapalli, V. L. N. (2024). Core structure optimization in double-D coil with enhanced performance for inductive wireless power transfer system. IEEE Access, 12, 135489-135505.

Chen, K., & Zhao, Z. (2013). Analysis of the double-layer printed spiral coil for wireless power transfer. IEEE Journal of Emerging and Selected Topics in Power Electronics, 1(2), 114-121.

Chen, Y., Seyedi, S. M., & Toliyat, H. A. (2024, June). Coil design of integrated LCC-S compensation topology for wireless charging. In 2024 IEEE Transportation Electrification Conference and Expo (ITEC) (pp. 1-6). IEEE.

Côte, N., Sterna, L., Garraud, N., Perichon, P., Frassati, F., & Boisseau, S. (2022, July). Design and optimization of a self-resonant impedance matched coil for Wireless Power Transfer. In 2022 Wireless Power Week (WPW) (pp. 48-53). IEEE.

Dai, Z., Sun, Y., Gan, Q., Zhai, Y., Wang, H., Wei, X., ... & Zhang, X. (2025). Hybrid Wireless Power Transfer with Self-Resonance Coupler Based on Integrated Coil. IEEE Transactions on Power Electronics.

de Miranda, C. M., & Pichorim, S. F. (2016). A self-resonant two-coil wireless power transfer system using open bifilar coils. IEEE Transactions on Circuits and Systems II: Express Briefs, 64(6), 615-619.

de Miranda, C. M., & Pichorim, S. F. (2019). On the self-resonant frequency reduction of closed-and open-bifilar coils. International Journal of Circuit Theory and Applications, 47(5), 641-653.

de Miranda, C. M., & Pichorim, S. F. (2019, June). Alternative configuration of open-bifilar coil for self-resonant wireless power transfer system. In 2019 IEEE Wireless Power Transfer Conference (WPTC) (pp. 116-119). IEEE.

de Miranda, C. M., & Pichorim, S. F. (2022). A three-coil wireless power transfer system using self-resonant open-bifilar coils. AEU-International Journal of Electronics and Communications, 154, 154300.

Dionigi, M., & Mongiardo, M. (2012). A novel coaxial loop resonator for wireless power transfer. International Journal of RF and Microwave Computer-Aided Engineering, 22(3), 345-352.

Du, X., Li, C., & Dujić, D. (2021). Design and characterization of PCB spiral coils for inductive power transfer in medium-voltage applications. IEEE Transactions on Power Electronics, 37(5), 6168-6180.

Eo, Y., & Eisenstadt, W. R. (2002). High-speed VLSI interconnect modeling based on S-parameter measurements. IEEE Transactions on Components, Hybrids, and Manufacturing Technology, 16(5), 555-562.

Essa, A., Almajali, E., Barneih, F., Yousaf, J., Amaya, R. E., & Mahmoud, S. (2025). A Compact Tissue-Insensitive Ultra-Wideband Implantable Antenna for Wireless Power Transfer in Implantable Medical Devices. IEEE Open Journal of Antennas and Propagation.

Faisal, F., Basir, A., Zada, M., Björninen, T., Chaker, M., & Djerafi, T. (2024). Simultaneous wireless powering and biotelemetry for biomedical implants using 3-D printable water-based self-diplexing antennas. IEEE Transactions on Antennas and Propagation, 73(4), 2288-2298.

Fang, X., Wu, R., & Sin, J. K. (2015). Analytical modeling of AC resistance in thick coil integrated spiral inductors. IEEE Transactions on Electron Devices, 63(2), 760-766.

Fang, Z., Zhong, W., & Lu, Y. (2024, May). Analysis and Design of Three-Coil Wireless Power Transfer System with Split Transmitting Coils. In 2024 IEEE 7th International Electrical and Energy Conference (CIEEC) (pp. 3038-3043). IEEE.

Farajizadeh, F., Vilathgamuwa, D. M., Jovanovic, D., Jayathurathnage, P., Ledwich, G., & Madawala, U. (2019). Expandable N-legged converter to drive closely spaced multitransmitter wireless power transfer systems for dynamic charging. IEEE Transactions on Power Electronics, 35(4), 3794-3806.

Gao, X., Dong, S., Yin, Y., Zhang, Y., & Cui, S. (2022). An economical DWPT system with mutual compensation of segmented power supply rails based on LCL topology. IEEE Transactions on Transportation Electrification, 9(2), 2865-2877.

García-Moreno, S., & Bandala-Sánchez, M. (2013). Fringing capacitance in sections of circular parallel plates with variable overlapping area. Electronics letters, 49(11), 712-714.

Greiner, W. (1991). Theoretische Physik, vol. 3. Frankfurt am Main: H. Deutsch.

Gu, L., Zulauf, G., Stein, A., Kyaw, P. A., Chen, T., & Davila, J. M. R. (2020). 6.78-MHz wireless power transfer with self-resonant coils at 95% DC–DC efficiency. IEEE Transactions on Power Electronics, 36(3), 2456-2460.

Guan, Y., Qiao, Y., Mai, J., Wang, Y., & Xu, D. (2025). Topology Reconstruction of Multicoil Transmitter in UAV System for Low Stray Magnetic Field. IEEE Transactions on Power Electronics.

Ha-Van, N., Tretyakov, S. A., & Simovski, C. R. (2025). Optimal frequencies for wireless power transfer through biological tissues. IEEE Open Journal of Antennas and Propagation, 6(2), 433-444.

Hanawa, K., & Imura, T. (2021, October). Proposal of ferrite-less and capacitor-less 85 kHz four-layer coil for stationary wireless power transfer. In IECON 2021–47th Annual Conference of the IEEE Industrial Electronics Society (pp. 1-5). IEEE.

Hanawa, K., Imura, T., Hori, Y., & Abe, N. (2022, October). Comparison of Circular Coil, Double-D Coil, and 85 kHz Self-Resonant Coil in Road Embedment for Dynamic Wireless Power Transfer. In IECON 2022–48th Annual Conference of the IEEE Industrial Electronics Society (pp. 1-6). IEEE.

Ho, G. K. Y., & Pong, B. M. (2019). Multilayer flexible printed circuitry planar transformer with integrated series capacitance for an LLC converter. IEEE Transactions on Power Electronics, 34(11), 11139-11152.

Hou, X., Hu, H., Su, Y., Liu, Z., Deng, Z., & Deng, R. (2022). A multirelay wireless power transfer system with double-sided LCC compensation network for online monitoring equipment. IEEE Journal of Emerging and Selected Topics in Power Electronics, 11(1), 1262-1271.

Huang, Z., Fang, Z., Lam, C. S., Mak, P. I., & Martins, R. P. (2019). Cost-effective compensation design for output customization and efficiency optimization in series/series-parallel inductive power transfer converter. IEEE Transactions on Industrial Electronics, 67(12), 10356-10365.

Hurley, W. G., & Duffy, M. C. (1997). Calculation of self-and mutual impedances in planar sandwich inductors. IEEE Transactions on Magnetics, 33(3), 2282-2290.

Jeong, S., Kim, D. H., Song, J., Kim, H., Lee, S., Song, C., ... & Kim, J. (2018). Smartwatch strap wireless power transfer system with flexible PCB coil and shielding material. IEEE Transactions on Industrial Electronics, 66(5), 4054-4064.

Jeong, S., Kim, T. W., Lee, S., Sim, B., Park, H., Son, K., ... & Kim, B. J. (2022). Analysis of repetitive bending on flexible wireless power transfer (WPT) PCB coils for flexible wearable devices. IEEE Transactions on Components, Packaging and Manufacturing Technology, 12(11), 1748-1756.

Jiang, C., Gaona, D. E., Shen, Y., Zhao, H., Chau, K. T., & Long, T. (2020). Low-frequency medium power capacitor-free self-resonant wireless power transfer. IEEE Transactions on Industrial Electronics, 68(11), 10521-10533.

Jow, U. M., & Ghovanloo, M. (2008). Design and optimization of printed spiral coils for efficient transcutaneous inductive power transmission. IEEE Transactions on biomedical circuits and systems, 1(3), 193-202.

Kiani, M., & Ghovanloo, M. (2012). The circuit theory behind coupled-mode magnetic resonance-based wireless power transmission. IEEE Transactions on Circuits and Systems I: Regular Papers, 59(9), 2065-2074.

Kiani, M., Jow, U. M., & Ghovanloo, M. (2011). Design and optimization of a 3-coil inductive link for efficient wireless power transmission. IEEE Transactions on biomedical circuits and systems, 5(6), 579-591.

Kim, K. B., Levi, E., Zabar, Z., & Birenbaum, L. (1997). Mutual inductance of noncoaxial circular coils with constant current density. IEEE Transactions on Magnetics, 33(5), 4303-4309.

Kim, M., & Choi, J. (2022, July). Design of self-resonant spiral coils for mid-range, high-frequency wireless power transfer systems. In 2022 Wireless Power Week (WPW) (pp. 33-38). IEEE.

Knaisch, K., Springmann, M., & Gratzfeld, P. (2016, April). Comparison of coil topologies for inductive power transfer under the influence of ferrite and aluminum. In 2016 Eleventh International Conference on Ecological Vehicles and Renewable Energies (EVER) (pp. 1-9). IEEE.

Kyaw, P. A., Stein, A. L., & Sullivan, C. R. (2017, March). High-Q resonator with integrated capacitance for resonant power conversion. In 2017 IEEE Applied Power Electronics Conference and Exposition (APEC) (pp. 2519-2526). IEEE.

Langton, N. H. (1981). The parallel-plate capacitor with symmetrically placed unequal plates. Journal of Electrostatics, 9(4), 289-305.

Lee, J., Kim, Y., Kang, D., Song, I., & Lee, B. (2024). A reconfigurable bidirectional wireless power and full-duplex data transceiver IC for wearable biomedical applications. IEEE Transactions on Biomedical Circuits and Systems, 19(4), 767-776.

Lee, Y. D., Kim, K. W., & Moon, G. W. (2021). A self-compensated planar coil with integrated single-switch regulator for wireless power transfer (WPT) systems. IEEE Transactions on Power Electronics, 36(10), 10954-10958.

Li, J., & Costinett, D. (2018, March). Analysis and design of a series self-resonant coil for wireless power transfer. In 2018 IEEE Applied Power Electronics Conference and Exposition (APEC) (pp. 1052-1059). IEEE.

Li, J., Yu, S., Kou, N., Ding, Z., & Zhang, Z. (2022). Cylindrical magnetically coupled resonant wireless power transfer system based on flexible PCB coils. IEEE Microwave and Wireless Components Letters, 32(12), 1479-1482.

Li, K., Wu, J., Wang, M., Yucel, A. C., & Hui, S. Y. R. (2023, March). A sandwich structure for cost-effective printed-circuit-board wireless power resonator. In 2023 IEEE Applied Power Electronics Conference and Exposition (APEC) (pp. 818-821). IEEE.

Li, K., Wu, J., Yucel, A. C., & Hui, S. Y. R. (2023). New printed-circuit-board resonators with high quality factor and transmission efficiency for mega-hertz wireless power transfer applications. IEEE Transactions on Power Electronics, 38(10), 13207-13218.

Li, W., Zhang, Q., Cui, C., & Wei, G. (2021). A self-tuning S/S compensation WPT system without parameter recognition. IEEE Transactions on Industrial Electronics, 69(7), 6741-6750.

Li, X., Wang, C., Wang, H., Dai, X., Sun, Y., & Hu, A. P. (2023). A robust wireless power transfer system with self-alignment capability and controllable output current for automatic-guided vehicles. IEEE Transactions on Power Electronics, 38(10), 11898-11906.

Li, Y., Chen, J., Yang, S., Wang, H., Wei, L., Xiao, J., & He, Z. (2026). Self-Resonant Multi-Relay WPT Systems with Four-layer Antisymmetric PCB Resonator Structure for Modern Power Inspection Applications: Analysis, Optimization and Experimental Validation. IEEE Transactions on Transportation Electrification.

Liu, Y., Yang, F., Han, Y., Gao, J., Sun, H., Wang, C., ... & Sun, R. (2023, November). Optimization Design Method for Printed Circuit Board Self-Resonant Coil. In 2023 IEEE 2nd International Power Electronics and Application Symposium (PEAS) (pp. 1316-1321). IEEE.

Lope, I., Carretero, C., Acero, J., Alonso, R., & Burdio, J. M. (2013). AC power losses model for planar windings with rectangular cross-sectional conductors. IEEE Transactions on Power Electronics, 29(1), 23-28.

Lu, J., Zhu, G., Lin, D., Zhang, Y., Wang, H., & Mi, C. C. (2020). Realizing constant current and constant voltage outputs and input zero phase angle of wireless power transfer systems with minimum component counts. IEEE Transactions on Intelligent Transportation Systems, 22(1), 600-610.

Lu, M., & Ngo, K. D. (2019). Analytical calculation of proximity-effect resistance for planar coil with litz wire and ferrite plate in inductive power transfer. IEEE Transactions on Industry Applications, 55(3), 2984-2991.

Machnoor, M., Rodríguez, E. S. G., Kosta, P., Stang, J., & Lazzi, G. (2018). Analysis and design of a 3-coil wireless power transmission system for biomedical applications. IEEE Transactions on Antennas and Propagation, 67(8), 5012-5024.

Makhetha, M. J., Markus, E. D., & Abu-Mahfouz, A. M. (2022). Efficient wireless power transfer via self-resonant Conformal Strongly Coupled Magnetic Resonance for wireless sensor networks. Energy Reports, 8, 1358-1367.

Mao, X., Lin, J., Su, T., & Zhang, Y. (2023). Automatic guided vehicle wireless charging with dual receiving coils for misalignment tolerance. IEEE Transactions on Circuits and Systems II: Express Briefs, 71(1), 336-339.

Matsumoto, H., Shibako, Y., & Neba, Y. (2017). Contactless power transfer system for AGVs. IEEE Transactions on Industrial Electronics, 65(1), 251-260.

McDonough, M., & Fahimi, B. (2014, March). Comparison between circular and square coils for use in Wireless Power Transmission. In 9th IET International Conference on Computation in Electromagnetics (CEM 2014) (pp. 5-14). Stevenage UK: IET.

Meng, M., & Kiani, M. (2016). Design and optimization of ultrasonic wireless power transmission links for millimeter-sized biomedical implants. IEEE Transactions on Biomedical Circuits and Systems, 11(1), 98-107.

Mohammad, M., Rallabandi, V., Onar, O. C., & Su, G. J. (2025, March). Capacitor Design for Self-Resonant Coils for Long-Distance Wireless Power Transfer System. In 2025 IEEE Applied Power Electronics Conference and Exposition (APEC) (pp. 1635-1639). IEEE.

Mohammad, M., Rallabandi, V., Xue, L., Su, G. J., Galigekere, V. P., Chowdhury, S., & Wilkins, J. (2023, June). Self-resonant coil design for high-frequency high-power inductive wireless power transfer. In 2023 IEEE Wireless Power Technology Conference and Expo (WPTCE) (pp. 1-5). IEEE.

Mohan, S. S., del Mar Hershenson, M., Boyd, S. P., & Lee, T. H. (2002). Simple accurate expressions for planar spiral inductances. IEEE Journal of Solid-State Circuits, 34(10), 1419-1424.

Moisello, E., Liotta, A., Malcovati, P., & Bonizzoni, E. (2023). Recent trends and challenges in near-field wireless power transfer systems. IEEE Open Journal of the Solid-State Circuits Society, 3, 197-213.

Moon, S., Kim, B. C., Cho, S. Y., Ahn, C. H., & Moon, G. W. (2014). Analysis and design of a wireless power transfer system with an intermediate coil for high efficiency. IEEE Transactions on Industrial Electronics, 61(11), 5861-5870.

Mühlethaler, J. (2012). Modeling and multi-objective optimization of inductive power components (Doctoral dissertation, ETH Zurich).

Munsi, A., Pradhan, S., & Aditya, K. (2025). Advancements in inductive wireless power transfer: A comprehensive review. Chinese Journal of Electrical Engineering.

Narayanamoorthi, R., & Juliet, A. V. (2018). Capacitor-less high-strength resonant wireless power transfer using open bifilar spiral coil. IEEE Transactions on Applied Superconductivity, 29(1), 1-8.

Nguyen, H. T., Alsawalhi, J. Y., Al Hosani, K., Al-Sumaiti, A. S., Al Jaafari, K. A., Byon, Y. J., & El Moursi, M. S. (2021). Review map of comparative designs for wireless high-power transfer systems in EV applications: Maximum efficiency, ZPA, and CC/CV modes at fixed resonance frequency independent from coupling coefficient. IEEE Transactions on Power Electronics, 37(4), 4857-4876.

Nishihata, H., Sasa, N., Imura, T., Hori, Y., Inoue, S., & Kano, Y. (2025, June). Novel Self-Resonant Multilayer Onboard Coil for 85 kHz Wireless Power Transfer. In 2025 IEEE Wireless Power Technology Conference and Expo (WPTCE) (pp. 1-6). IEEE.

Odendaal, W. G., & Li, Y. (2005). U.S. Patent No. 6,960,968. Washington, DC: U.S. Patent and Trademark Office.

Ongayo, D., & Hanif, M. (2015, November). Comparison of circular and rectangular coil transformer parameters for wireless Power Transfer based on Finite Element Analysis. In 2015 IEEE 13th Brazilian Power Electronics Conference and 1st Southern Power Electronics Conference (COBEP/SPEC) (pp. 1-6). IEEE.

Park, Y., Hung, P. D., Youn, D., Kwon, D., Kim, C., & Je, M. (2025). A wireless power and data transfer system for medical implants using a miniaturized inductive link with frequency-splitting enhancement. IEEE Journal of Solid-State Circuits, 60(11), 3966-3984.

Pei, R., Leach, M. P., Lim, E. G., Wang, Z., Song, C., Wang, J., ... & Huang, Y. (2020). Wearable EBG-backed belt antenna for smart on-body applications. IEEE Transactions on Industrial Informatics, 16(11), 7177-7189.

Pozar, D. M. (2011). Microwave engineering. John Wiley & Sons.

Qin, R. (2022). A High Frequency Wireless Power Transfer System for Electric Vehicle Charging Using Multi-layer Non-uniform Self-resonant Coil.

Qin, R., & Costinett, D. (2019, September). Multi-layer non-uniform series self-resonant coil for wireless power transfer. In 2019 IEEE Energy Conversion Congress and Exposition (ECCE) (pp. 3333-3339). IEEE.

Qin, R., Li, J., & Costinett, D. (2020, October). A high frequency wireless power transfer system for electric vehicle charging using multi-layer nonuniform self-resonant coil at MHz. In 2020 IEEE Energy Conversion Congress and Exposition (ECCE) (pp. 5487-5494). IEEE.

Qin, R., Li, J., & Costinett, D. (2021). A 6.6-kW high-frequency wireless power transfer system for electric vehicle charging using multilayer nonuniform self-resonant coil at MHz. IEEE Transactions on Power Electronics, 37(4), 4842-4856.

Qin, R., Li, J., Sun, J., & Costinett, D. (2023). Shielding design for high-frequency wireless power transfer system for EV charging with self-resonant coils. IEEE Transactions on Power Electronics, 38(6), 7900-7909.

Qin, R., Li, J., Sun, J., & Costinett, D. (2023, March). Fully compensated self-resonant coil with low e-field and low profile for consumer electronics wireless charging. In 2023 IEEE Applied Power Electronics Conference and Exposition (APEC) (pp. 795-802). IEEE.

Qu, J., Kiratipongvoot, S., Lee, C. K., & Tang, N. (2018, September). An integrated printed-circuit-board resonator design for inductive power transfer system. In 2018 IEEE Energy Conversion Congress and Exposition (ECCE) (pp. 2021-2025). IEEE.

RamRakhyani, A. K., Mirabbasi, S., & Chiao, M. (2010). Design and optimization of resonance-based efficient wireless power delivery systems for biomedical implants. IEEE Transactions on Biomedical Circuits and Systems, 5(1), 48-63.

Rezazade, S., Shahirinia, A., Naghash, R., Rasekh, N., & Afjei, S. E. (2022). A novel efficient hybrid compensation topology for wireless power transfer. IEEE Transactions on Industrial Electronics, 70(3), 2277-2285.

Saadabad, N. Z., Nasiri, A., & Nekoui, J. (2025). A new three-port DC/DC converter with soft switching, for PV applications. International Journal of Circuit Theory and Applications, 53(2), 993-1009.

Saadabad, N. Z., Nekoui, J., Dehbozorgi, M. R., Wang, Q., & Chandra, A. (2025, October). A three-coil self-resonant WPT system for biomedical applications. In IECON 2025–51st Annual Conference of the IEEE Industrial Electronics Society (pp. 1-6). IEEE.

Saadabad, N. Z., Wang, Q., & Chandra, A. (2025). A multilayer PCB coil for self-resonant wireless power transfer systems. IEEE Transactions on Industrial Electronics.

Saadabad, N. Z., Wang, Q., & Chandra, A. (2025). Performance comparison of coil geometries in self-resonant wireless power transfer system. IEEE Transactions on Industry Applications.

Saket, M. A., Shafiei, N., & Ordonez, M. (2016). LLC converters with planar transformers: Issues and mitigation. IEEE Transactions on Power Electronics, 32(6), 4524-4542.

Sasahara, I., & Akatsu, K. (2022, June). A Coupler design for high power 2.3 kW WPT using 13.56 MHz. In 2022 IEEE 31st International Symposium on Industrial Electronics (ISIE) (pp. 762-767). IEEE.

Schelles, M., Lievens, W., Goyvaerts, L., Ceyssens, F., Muller, R., & Kraft, M. (2025). Comparison and System Development of a 2-coil and 3-coil Inductive Link for Transcutaneous Power Transfer. IEEE Access.

Sezer, C., Odabas, G., Sinirlioglu, S., Kaya, B., & Altintas, N. (2021, April). Modeling of WPT system for small home appliances. In 2021 8th International Conference on Electrical and Electronics Engineering (ICEEE) (pp. 243-247). IEEE.

Shah, I. A., Zada, M., Shah, S. A. A., Basir, A., & Yoo, H. (2023). Flexible metasurface-coupled efficient wireless power transfer system for implantable devices. IEEE Transactions on Microwave Theory and Techniques, 72(4), 2534-2547.

Shahsevani, J., & Beiranvand, R. (2024). Application-oriented review of the LLC-based resonant converters. IEEE Access, 12, 52687-52726.

Shevchenko, V., Husev, O., Pakhaliuk, B., Karlov, O., & Kondratenko, I. (2019, July). Coil design for wireless power transfer with series-parallel compensation. In 2019 IEEE 2nd Ukraine Conference on Electrical and Computer Engineering (UKRCON) (pp. 401-407). IEEE.

Shevchenko, V., Husev, O., Strzelecki, R., Pakhaliuk, B., Poliakov, N., & Strzelecka, N. (2019). Compensation topologies in IPT systems: Standards, requirements, classification, analysis, comparison and application. IEEE Access, 7, 120559-120580.

Shin, J., Shin, S., Kim, Y., Ahn, S., Lee, S., Jung, G., ... & Cho, D. H. (2013). Design and implementation of shaped magnetic-resonance-based wireless power transfer system

for roadway-powered moving electric vehicles. IEEE Transactions on Industrial Electronics, 61(3), 1179-1192.

Smith, G. S. (1972). Proximity effect in systems of parallel conductors. Journal of Applied Physics, 43(5), 2196-2203.

Song, K., Li, Z., Jiang, J., & Zhu, C. (2017). Constant current/voltage charging operation for series–series and series–parallel compensated wireless power transfer systems employing primary-side controller. IEEE Transactions on Power Electronics, 33(9), 8065-8080.

Son, H. C., Kim, J., Kim, D. H., Kim, K. H., & Park, Y. J. (2011, December). Self-resonant coil with coaxial-like capacitor for wireless power transfer. In Asia-Pacific Microwave Conference 2011 (pp. 90-93). IEEE.

Son, H. C., Kim, J., Kim, D. H., Kim, K. H., & Park, Y. J. (2013). Analysis and Application of Compact Planar Multi-Loop Self-Resonant Coil of High Quality Factor with Coaxial Cross Section. The Journal of Korean Institute of Electromagnetic Engineering and Science, 24(4), 466-473.

Son, J., Shrestha, N., & Williamson, S. (2024, February). Comprehensive comparative analysis of circular, rectangular, and hexagonal coils for wireless charging of E-mobility. In 2024 IEEE Applied Power Electronics Conference and Exposition (APEC) (pp. 2915-2921). IEEE.

Stein, A. L., Kyaw, P. A., & Sullivan, C. R. (2017, March). High-Q self-resonant structure for wireless power transfer. In 2017 IEEE Applied Power Electronics Conference and Exposition (APEC) (pp. 3723-3729). IEEE.

Stein, A. L., Kyaw, P. A., & Sullivan, C. R. (2018). Wireless power transfer utilizing a high-Q self-resonant structure. IEEE Transactions on Power Electronics, 34(7), 6722-6735.

Stein, A. L., Kyaw, P. A., Feldman-Stein, J., & Sullivan, C. R. (2018, March). Thin self-resonant structures with a high-Q for wireless power transfer. In 2018 IEEE Applied Power Electronics Conference and Exposition (APEC) (pp. 1044-1051). IEEE.

Su, Y. P., Liu, X., & Hui, S. R. (2009). Mutual inductance calculation of movable planar coils on parallel surfaces. IEEE Transactions on Power Electronics, 24(4), 1115-1123.

Sullivan, C. R., & Beghou, L. (2013, June). Design methodology for a high-Q self-resonant coil for medical and wireless-power applications. In 2013 IEEE 14th Workshop on Control and Modeling for Power Electronics (COMPEL) (pp. 1-8). IEEE.

Sun, S., Zhang, B., Rong, C., Shu, X., & Wei, Z. (2021). A multireceiver wireless power transfer system using self-oscillating source composed of zero-voltage switching full-bridge inverter. IEEE Transactions on Industrial Electronics, 69(3), 2885-2895.

Takahashi, Y., Hata, K., Imura, T., & Hori, Y. (2018, October). Comparison of capacitor-and ferrite-less 85kHz self-resonant coils considering dielectric loss for in-motion wireless power transfer. In IECON 2018-44th Annual Conference of the IEEE Industrial Electronics Society (pp. 5159-5163). IEEE.

Vendik, O. G., Zubko, S. P., & Nikol'Skii, M. A. (1999). Modeling and calculation of the capacitance of a planar capacitor containing a ferroelectric thin film. Technical Physics, 44(4), 349-355.

Vishnuram, P., & Ramachandiran, G. (2020). Capacitor-less induction heating system with self-resonant bifilar coil. International Journal of Circuit Theory and Applications, 48(9), 1411-1425.

Wang, J., Leach, M. P., Lim, E. G., Wang, Z., Jiang, Z., Pei, R., & Huang, Y. (2019). A conformal split-ring loop as a self-resonator for wireless power transfer. IEEE Access, 8, 911-919.

Wang, J., Wang, C., Lu, Z., Guo, Z., & Wang, S. (2022). Single-switch wireless-power-transfer circuit with P-CLC compensation network used for battery charging. IEEE Transactions on Transportation Electrification, 8(3), 4014-4026.

Wang, Q., Saket, M. A., Troy, A., & Ordonez, M. (2020). A self-compensated planar coil for resonant wireless power transfer systems. IEEE Transactions on Power Electronics, 36(1), 674-682.

Wang, Y., Sun, Z., Zhang, X., Yang, Y., & Hui, S. Y. R. (2025, March). Integrated hybrid inductive and capacitive power transfer system with asymmetrical PCB self-resonator. In 2025 IEEE Applied Power Electronics Conference and Exposition (APEC) (pp. 3275-3280). IEEE.

Wang, Y., Wang, K., Li, K., Yang, Y., & Hui, S. Y. R. (2024). Multi-MHz inductive and capacitive power transfer systems with PCB-based self-resonators. IEEE Transactions on Power Electronics, 39(10), 14077-14090.

Weng, W., Wu, J., Qin, L., Chen, H., Deng, Y., & He, X. (2025). Analysis and optimization of wireless power and information dual transfer in multi-coil system. IEEE Transactions on Power Electronics.

Wheeler, H. A. (2006). Simple inductance formulas for radio coils. Proceedings of the Institute of Radio Engineers, 16(10), 1398-1400.

Wu, S., Jiao, Y., Cai, C., Yu, J., & Ren, X. (2025). Self-Resonant Planar Coil on Sheet Metal for Inductive Power Transfer in Neural Stimulation Implants. IEEE Journal of Emerging and Selected Topics in Power Electronics.

Wu, Y., Liu, C., Zhou, M., Mao, X., & Zhang, Y. (2023). An antioffset electric vehicle wireless charging system based on dual coupled antiparallel coils. IEEE Transactions on Power Electronics, 38(5), 5634-5637.

Xiang, J., Jiang, C. Q., Ma, T., Wang, Y., & Fan, Y. (2024). An ultra-thin self-resonant coupler with nanocrystalline flake ribbons for wireless power transfer system. IEEE Transactions on Magnetics, 60(9), 1-5.

Xiang, J., Jiang, C. Q., Ma, T., Wang, X., Fan, Y., & Zhou, J. (2024). High power density self-resonant coupler for flexible surface wireless power transfer system with nanocrystalline ribbon. IEEE Transactions on Power Electronics, 39(10), 13975-13987.

Xue, L., Su, G. J., Mohammad, M., Rallabandi, V., Wilkins, J., Chowdhury, S., ... & Ozpineci, B. (2023, October). Pushing to the distance boundary of inductive wireless power transfer. In 2023 IEEE Energy Conversion Congress and Exposition (ECCE) (pp. 1625-1631). IEEE.

Xu, X., Wei, R., Liao, W., Yao, Y., Huang, X., Tang, X., ... & Lan, J. (2024). An adaptive impedance matching system with fast optimization control algorithm for wireless power transfer via magnetic coupling resonance. IEEE Transactions on Circuits and Systems I: Regular Papers, 71(10), 4802-4811.

Yang, S., Cooper, E. B., Elkhouly, E., Narayan, J. K., & Ren, S. (2015). Low emission coil topology for wireless charging. patentus US, 14(672,082).

Yi, Z., Li, M., Muneer, B., He, G., & Yang, X. X. (2020). Self-resonant antisymmetric planar coil for compact inductive power transfer system avoiding compensation circuits. IEEE Transactions on Power Electronics, 36(5), 5121-5134.

Yi, Z., Yang, K., Yang, X. X., Li, M., & Zeng, D. (2024). A gradual-width high-Q self-resonant coil based on coplanar waveguide. IEEE Microwave and Wireless Technology Letters, 35(2), 165-168.

Yin, Y., Li, H., Gao, S., Li, Y., Zhang, X., & Fu, M. (2023). A simple integrated and low-radiation receiver for inductive power transfer. IEEE Transactions on Power Electronics, 38(10), 11776-11785.

Yue, C. P., & Wong, S. S. (2002). Physical modeling of spiral inductors on silicon. IEEE Transactions on Electron Devices, 47(3), 560-568.

Yue, K., Liu, Y., Zhang, X., Fu, M., Liang, J., & Wang, H. (2023). Transmitter-side voltage-based mutual inductances and load tracking for two-transmitter LCC-S compensated wireless power transfer systems. IEEE Journal of Emerging and Selected Topics in Power Electronics, 12(2), 2317-2332.

Zahedi, N., Wang, Q., & Chandra, A. (2023, August). A review of self-compensated wireless power transfer system. In 2023 IEEE 14th International Conference on Power Electronics and Drive Systems (PEDS) (pp. 1-6). IEEE.

Zahedi, N., Wang, Q., & Chandra, A. (2023, August). Comparative study of self-compensated coil geometries for wireless power transfer system. In 2023 IEEE 14th International Conference on Power Electronics and Drive Systems (PEDS) (pp. 1-5). IEEE.

Zahedi Saadabad, N., Hossein Hosseini, S., Nasiri, A., & Sabahi, M. (2020). New soft-switched high gain three-port DC–DC converter with coupled inductors. IET Power Electronics, 13(19), 4562-4571.

Zhang, R., Lin, X. Q., Li, C., Cheng, F., & Fan, Y. (2013, July). A high-efficiency wireless power transmission circuit using coaxial resonators welded on a substrate. In 2013 Cross Strait Quad-Regional Radio Science and Wireless Technology Conference (pp. 113-115). IEEE.

Zhang, X., Lu, J., Chen, J., Tong, L., Shi, Y., & Qiu, H. (2024). Impedance matching through a reconfigurable relay coil achieving maximum wireless power transfer under variations of coupling coefficient and load resistance. IEEE Transactions on Circuits and Systems I: Regular Papers, 71(10), 4851-4860.

Zhang, Y., Shen, Z., Pan, W., Wang, H., Wu, Y., & Mao, X. (2022). Constant current and constant voltage charging of wireless power transfer system based on three-coil structure. IEEE Transactions on Industrial Electronics, 70(1), 1066-1070.

Zhang, Y., Wu, Y., Zhou, M., Zhou, H., Mao, X., Jin, T., & Chen, X. (2023). An integrated electric vehicle charging system of wireless power transfer and auxiliary power module with shared converter and magnetic coupler. IEEE Transactions on Industrial Electronics, 71(9), 10414-10421.

Zhang, Y., Zhou, H., Xie, R., Mao, X., Chen, X., & Li, Z. (2024). A smooth-output dynamic wireless charging system for automated guided vehicles with dual-receiver magnetic coupler. IEEE Transactions on Power Electronics, 40(4), 4711-4715.

Zhang, Z., Georgiadis, A., & Cecati, C. (2019). Wireless power transfer for smart industrial and home applications. IEEE Transactions on Industrial Electronics, 66(5), 3959-3962.

Zhong, W. X., Zhang, C., Liu, X., & Hui, S. R. (2014). A methodology for making a three-coil wireless power transfer system more energy efficient than a two-coil counterpart for extended transfer distance. IEEE Transactions on Power Electronics, 30(2), 933-942.

Zhu, L., Wang, L., Wu, M., Zhao, C., & Yu, L. (2023). Precise modeling and design of self-resonant for high-efficiency mid-range wireless power transfer system. IEEE Transactions on Power Electronics, 38(6), 7848-7862.

Zhu, L., Wang, L., Zhao, C., Shen, J., Wu, M., & Pei, L. (2024). Design and optimization of unequal-pitch self-resonant helical coils for high-efficiency mid-range wireless power transfer. IEEE Transactions on Power Electronics, 39(11), 15281-15294.

Zhu, L., Wang, L., Zhao, C., Shen, J., Wu, M., & Pei, L. (2024, May). An Improved Calculation for Ohmic Resistance of Round-wire Self-Resonant Coils in High-Frequency Wireless Power Transfer System. In 2024 IEEE 10th International Power Electronics and Motion Control Conference (IPEMC2024-ECCE Asia) (pp. 4707-4712). IEEE.

Zierhofer, C. M., & Hochmair, E. S. (2002). Geometric approach for coupling enhancement of magnetically coupled coils. IEEE Transactions on Biomedical Engineering, 43(7), 708-714